Aerothermodynamic Properties of an Upper Stage Rocket Equipped with Control Surfaces

Marília de Almeida Carvalho Matos

Thesis to obtain the Master of Science Degree in

Aerospace Engineering

Supervisor(s): Prof. Mário António Prazeres Lino da Silva
Eng. Nuno Tiago Salavessa Cardoso Hormigo Vicente

Examination Committee

Chairperson: Prof. José Fernando Alves da Silva
Supervisor: Prof. Mário António Prazeres Lino da Silva
Member of the Committee: Prof. João Manuel Gonçalves de Sousa Oliveira

November 2019

”If one can figure out how to effectively reuse rockets just like airplanes, the cost of access to space will be reduced by as much as a factor of a hundred. A fully reusable vehicle has never been done before. That really is the fundamental breakthrough needed to revolutionise access to space.”

- Elon Musk

”That we have written an equation does not remove from
the flow of fluids its charm or mystery or its surprise.”

- Richard Feynman

Acknowledgments

First and foremost, I would like to express my sincere gratitude to Prof. Mário Lino da Silva for accepting to be my supervisor, for his guidance on this work and for the wise words which kept me going when nothing seemed to make sense. Without his continuous support and immense knowledge the completion of this thesis would not be possible. I would also like to thank Eng. Tiago Hormigo from SpinWorks who readily answered all my questions and for his insightful comments and Prof. José Maria André and Prof. Melão Barros for the afternoon spent clarifying all my doubts regarding aerodynamic forces and Newtonian fluid. My sincere thanks also goes to Duarte Gonçalves, for his willingness to teach me how to use SPARK, for the hours he spent answering my requests and for his endless patience and to João Vargas, for his helpful answers to all my questions. I am also grateful to the teachers and professors who I happened to come across over the last 17 years for their true mentoring.

In order to get through my dissertation, more than academic support was desired. I have many, many people to thank for listening to me and, at times, having to tolerate me over the past years. So, last, but not least, I must thank: my friends, who believe in me and are always by my side, in particular Jack, Murrough, Ramalho and Rohan, for finding the time to make sure that this manuscript was well-written; my family, for supporting me in every academic adventure, specially my little brother, my grandparents, for their non-exhaustive guidance and warm meals, and my mum, for being the strongest person I know; Carlos and Fátima Pereira, also for their warm meals and Eduardo, for his unfailing support and for keeping me sane. I dedicate my thesis to all of you.

Resumo

Os mais recentes desenvolvimentos na indústria aeroespacial apontam para uma emergente necessidade na reutilização de foguetões na sua totalidade. Apesar de empresas como a SpaceX, Blue Origin e Rocket Lab já terem demonstrado as suas intenções no reaproveitamento de primeiros andares, a maior dificuldade assenta na recuperação controlada de andares superiores a velocidades orbitais. Este trabalho tem como objetivo estudar a reentrada de um andar superior de um foguetão equipado com superfícies de controlo através de simulações em CFD, com recurso ao código SPARK, desenvolvido e mantido no Instituto de Plasmas e Fusão Nuclear. A velocidade considerada para a simulação numérica foi 7.6 km/s, a uma altitude de 60 km. Os coeficientes aerodinâmicos e fluxos de calor foram calculados para esse ponto da trajetória e para duas geometrias do nariz do veículo diferentes (uma esférica e outra elítica), com o objetivo de determinar a eficiência das superfícies de controlo a diferentes ângulos (10°, 20° e 30°) e o sistema de proteção térmica adequado, respetivamente. Os dois modelos de transporte utilizados (Wilke e Gupta-Yos/CCS) mostraram concordância na camada de choque. Uma análise mais complexa foi efetuada tendo em conta o modelo de duas temperaturas proposto por Park no caso de desequilíbrio térmico. Este desequilíbrio mostrou-se claramente visível na zona da onda de choque, alcançando o equilíbrio térmico na zona de interesse (camada limite). As duas geometrias apresentaram uma boa semelhança aerodinâmica. As configurações e ângulos de deflexão em estudo resultaram numa máxima eficiência aerodinâmica para a geometria esférica de 0.19. A concordância entre os resultados para os casos de equilíbrio e não equilíbrio reforçam a suposição inicial de equilíbrio térmico na zona da camada limite.

Palavras-Chave: Reentrada, CFD Hipersónico, SPARK, Aerotermodinâmica, Superfícies de Controlo, Fluxos de Calor Convectivos

Abstract

The most recent developments in the aerospace industry have made it clear that there is an emergent need to reuse every part of a launch vehicle. Although companies such as SpaceX, Blue Origin and Rocket Lab have already demonstrated their intentions to retrieve first stages, the controlled recovery of upper stages travelling at orbital speed is still a much more difficult task. This work aimed to study the reentry of an upper stage rocket equipped with control surfaces by using the CFD SPARK code, developed and maintained at Institute for Plasmas and Nuclear Fusion. The reentry velocity considered for the simulation was 7.6 km/s at an altitude of 60 km and two different geometries for the nose region thermal protection system were examined (one spherical and one highly elliptical). Aimed at determining the efficiency of the control surfaces and the most suitable thermal protection system, the aerodynamic coefficients and convective heat fluxes were computed, respectively, at that point of the trajectory for the two nose geometries, three flap deflection angles (10°, 20° and 30°) and four flap configurations. The two transport models considered (Wilke and Gupta-Yos/CCS) showed a good agreement within the shock-layer. Park's two-temperature model for thermal non-equilibrium was also analysed. The non-equilibrium state was particularly visible in the shock-wave region, whereas in the boundary layer, an almost perfect agreement exists between the two temperatures. The two geometries presented good aerodynamic similarity. The highest aerodynamic efficiency was found for the spherical nose geometry with a value of 0.19. The agreement between the results for the equilibrium and non-equilibrium cases supports the initial assumption of thermal equilibrium in the boundary layer region.

Keywords: Reentry, Hypersonic CFD, SPARK, Aerothermodynamics, Control Surfaces, Convective Heat Fluxes

Contents

List of Tables

List of Figures

Nomenclature

Greek symbols

α	Angle of attack.
β	Side-slip angle.
γ	Ratio of specific heats.
Δ	Collision term.
δ	Boundary layer thickness.
ε	Energy of a particle.
ζ	Coefficient in Gupta-Yos formulation.
η	Flap deflection angle.
θ	Characteristic temperature.
κ	Thermal conductivity coefficient.
μ	Dynamic viscosity coefficient.
ν	Stoichiometric coefficient.
ν'	Stoichiometric coefficient on the reactant side of the chemical reaction.
ν''	Stoichiometric coefficient on the product side of the chemical reaction.
ρ	Density.
σ	Collision effective cross-section.
$\boldsymbol{\tau}$	Shear stress vector.
τ	Relaxation time.
$[\boldsymbol{\tau}]$	Viscous stress tensor.
ϕ	Scale factor.
$\dot{\Omega}$	Thermal energy source term.

$\overline{\Omega}^{(1,1)}$	Collision integral (1,1).
$\overline{\Omega}^{(2,2)}$	Collision integral (2,2).
$\dot{\omega}$	Species source term.

Roman symbols

A	Area.
A_i	Curve fitted coefficient in Wilke formulation.
a	Speed of sound.
B_i	Curve fitted coefficient in Wilke formulation.
C_D	Drag coefficient.
$\boldsymbol{C}_F$	Force coefficient vector.
C_i	Curve fitted coefficient in Wilke formulation.
C_L	Lift coefficient.
$\boldsymbol{C}_M$	Moment coefficient vector.
C_M	Moment coefficient.
C_p	Pressure coefficient.
c	Mass fraction.
c_p	Specific heat at constant pressure.
c_{ref}	Reference chord.
c_v	Specific heat at constant volume.
$\mathscr{D}$	Mass diffusion coefficient.
D	Drag force.
d	Dimensionless distance.
E	Total energy per unit mass.
e	Specific internal energy.
$\boldsymbol{F}$	Force vector.
g	Energy level degeneracy.
h	Enthalpy per unit mass.

h	Altitude.
$(\Delta h_s)^\circ$	Formation enthalpy.
$\boldsymbol{J}$	Mass diffusion flux vector.
K	Heat transfer coefficient.
K_n	Knudsen number.
k_B	Boltzmann constant.
k_b	Rate constant for the backward process of the chemical reaction.
k_f	Rate constant for the forward process of the chemical reaction.
L	Lift force.
Le	Lewis number.
l	Characteristic dimension of the body.
$\boldsymbol{M}$	Moment vector.
M	Molar mass.
M	Mach number.
m	Mass.
N	Number of particles.
N_A	Avogadro constant.
Ni	Number of mesh cells in the direction normal to the wall.
n	Number of moles.
$\hat{\boldsymbol{n}}$	Unit normal vector.
p	Static pressure.
$\boldsymbol{Q}$	Transformation matrix.
$\dot{Q}$	Total energy source term.
$\boldsymbol{q}$	Heat flux vector.
$\boldsymbol{q}_C$	Conduction heat flux vector.
$\boldsymbol{q}_E$	Total energy flux vector.
$\boldsymbol{q}_R$	Radiative heat flux vector.
R	Specific gas constant.

R_n	Hemispherical nose radius.
R_u	Universal gas constant.
$\boldsymbol{r}$	Position vector.
T	Temperature.
t	Time.
T_c	Controlling temperature.
$\boldsymbol{U}$	Velocity vector.
U	Magnitude of the velocity vector.
V	Volume.
x	Mole fraction.
X, Y, Z	Cartesian components.
$[X_i]$	Molar concentration.

Subscripts

∞	Free-stream condition.
A	Air-path reference frame.
B	Body-fixed reference frame.
C	Conduction.
D	Diffusive term.
e	Free electrons.
exc	Electronic excitation energy mode.
f	Frozen condition.
i	i^{th} species.
ion	Ionic species.
j	j^{th} species.
k	k^{th} energy mode.
l	l^{th} energy level.
m	Mixture.
mol.	Molecular species.

R	Radiative term.
r	r^{th} chemical reaction.
ref	Reference condition.
rot	Rotational energy mode.
tra	Translational energy mode.
vib	Vibrational energy mode.
w	Wall.

Superscripts

a	Ambipolar diffusion.
N	Normal.
S	Shear stress.
T	Transpose.

Acronyms and Glossary

CFD	Computational Fluid Dynamics is a branch of fluid mechanics that uses numerical methods and algorithms to solve problems that involve fluid flows.
CFL	Courant-Friedrichs-Lewy condition is a necessary condition for convergence while solving certain partial differential equations numerically.
CIRA	The Italian Aerospace Research Centre is a consortium established in 1984 to promote the growth and success of the aerospace industry in Italy.
CubeSat	Type of miniaturised satellite for space research that is made up of multiples of 10 cm × 10 cm × 11.35 cm cubic units.
ESA	European Space Agency is an intergovernmental organisation dedicated to the exploration of space.
EXPERT	European EXPerimental Re-entry Testbed is a flight testbed aiming to obtain aerothermodynamic flight data to validate design tools, ground test facilities and verification techniques.
H3NS	CIRA structured multi-block finite volume solver that allows for the treatment of a wide range of compressible fluid dynamic problems.

IPFN	Instituto de Plasmas e Fusão Nuclear, in english, Institute for Plasmas and Nuclear Fusion is a research unit of Instituto Superior Técnico, Lisbon.
ISS	International Space Station is a space station, or a habitable artificial satellite, in low Earth orbit.
iXV	The Intermediate eXperimental Vehicle is a ESA experimental suborbital reentry vehicle.
LEO	Low Earth Orbit is an Earth-centred orbit with an altitude of 2000 km or less.
MSPL	The NASA Mars Surveyor 2001 Lander was a planned Mars probe which was canceled in May 2000 in the wake of the failures of the Mars Climate Orbiter and Mars Polar Lander missions in late 1999.
SPARK	Software Package for Aerothermodynamics, Radiation and Kinetics is a CFD Navier-Stokes code for the modelling of entry plasmas, developed and maintained at IPFN.
SWBLI	Shock-wave boundary layer interactions are complex phenomena caused by the encounter of a shock wave with a boundary layer and possibly with other shock-waves.
TPS	Thermal Protection System is the shield which protects the vehicle from the high thermal loads during reentry.
Vega	*Vettore Europeo di Generazione Avanzata*, in english, Advanced generation European carrier rocket, is an expendable launch system in use by Arianespace jointly developed by the Italian Space Agency and the European Space Agency.

Chapter 1

Introduction

This chapter introduces this thesis by putting it into context. A preliminary introduction to the future of space exploration is presented and the major challenges reentry bodies face at hypersonic speeds is clarified. The objectives and a detailed description of the state-of-the-art of non-winged guided reentry vehicles are also discussed, followed by the outline of this work.

1.1 Motivation

From the practical beginning of astronautics and aeronautics with the Wright brothers' first airplane in 1903, there has been one primary goal: to fly faster, higher and cheaper. An exponential increase in both aircraft speed and altitude over the past century was observed, with the era of the hypersonic flight approaching day by day. In the 20^{th}, the technology needed to explore the space frontier was continuously being developed, which allowed the American and Soviet space programs to advance, the former being represented by Mercury, Gemini and Apollo. In the scope of planetary exploration, space probes have been sent to Venus, Mars, Jupiter and Titan's atmospheres [1]. Moreover, space agencies made it possible to intercept and even land on asteroids and comets. The Stardust mission collected dust samples from the tail of the comet Wild 2 [2], and returned them to Earth via a reentry capsule. The Hayabusa mission landed on the near-earth asteroid 25143 Itokawa and collected samples [3]. Finally, the Rosetta mission successfully landed on the comet 67P/Churyumov-Gerasimenko [4]. The capacity to perform simulations of entry vehicles is of paramount importance to the understanding of our Solar System and, to some extent, the Universe.

The future of space exploration is bright, with private industry bringing efficiency and automation, while space agencies continue to push for more ambitious agendas. Humanity's journey into space has been a difficult voyage with one of the most challenging tasks of space travel and exploration consisting of the safe, guided and controlled return of astronauts or samples from other celestial bodies to planet Earth [5].

At lower speeds, the control of a vehicle is achieved by making local alterations to the pressure field imparted on the vehicle by the flow. This can be accomplished with configurational changes, such as the deflection of a control surface. At hypersonic speeds, the control and support of the distributed loads on the vehicle become much more difficult since, in addition to the pressure load, a distributed thermal load is being applied and mass flow (ablation) acts on the vehicle [6]. Nevertheless, it is still necessary to guide the reentry vehicle so that it can navigate through the atmosphere with the right angles to withstand the friction and pressure occurring during atmospheric entry. Obtaining and mastering a complete knowledge of the physics of hypersonic flow is key for future space transportation missions, which include the return of soil samples originating in other celestial bodies (Mars, Moon, asteroids, comets) and the safe transportation of ISS experiments back to Earth.

One way to achieve the aforementioned objectives is by using body flaps. These aerodynamic control surfaces can allow an entry vehicle to meet aerodynamic performance requirements while reducing or eliminating the use of ballast mass [7]. Furthermore, it provides the capability to modulate the lift-to-drag ratio during entry, to land the vehicle on a dedicated landing area as well as to satisfy other mission constraints, such as peak heat rate limits. From a stability point of view, a hypersonic vehicle without active control is likely to be lightly damped or even unstable [8]. The body flap guidance technology can also help the future development of reusable launcher stages, revealing its high importance in cost efficiency, since the recovery effort is almost eliminated. Moreover, it is also essential for developing a wide range of other space transportation applications, including space planes, planetary probes and sample return, cargo and crew transport vehicles. Improvement in reentry technology can also be proven useful in innovative future missions for Earth observation, micro-gravity experimentation, high-altitude atmospheric research and servicing and disposing of future generation satellites [9]. Although challenging, this is a journey worth pursuing, given its immediate scientific benefits.

1.2 Atmospheric Reentry Overview

Hypersonic flow, commonly defined as having free stream speeds that exceeds a Mach number of 5, is described as the regime where the flow internal energy is much smaller, when compared to its kinetic energy [10]. Furthermore, its gas dynamics is fundamentally distinct from subsonic and supersonic ones, with the presence of strong high-temperature shocks, thermodynamic and chemical non-equilibrium where molecular vibrations, O_2 and N_2 dissociation, electronic excitation and ionisation take place. Figure 1.1 shows a schematic representation of a biconic shaped vehicle during Earth reentry and the chemical events associated to it. This sphere-cone shape with an additional frustum attached presents a significantly improved L/D ratio in comparison to the Apollo-like capsules, making it a better option to transport people, given its lower deceleration peak [6].

The bow shock created around the body is nearly normal in the nose region, which, at hypersonic speeds, significantly increases the temperature behind the strong shock through the transfer of kinetic to thermal/internal energy. The high-temperature environment of several thousand degrees experienced behind the bow shock wave is capable of exciting the generally dormant internal energy modes of the gas particles. For air at temperatures above 800 K, the vibrational and electronic excitation internal modes of the molecules become, particularly, accessible reservoirs capable of storing thermal energy, while

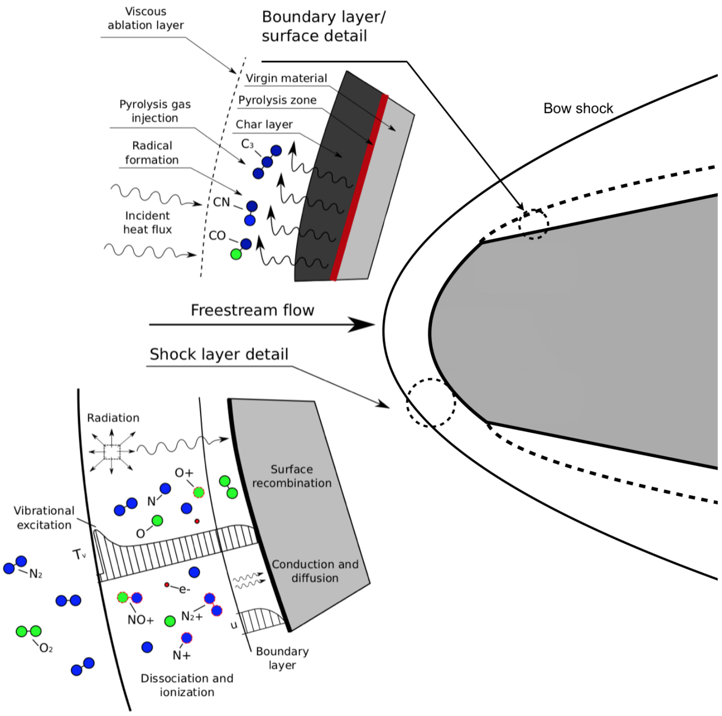

Figure 1.1: Aerothermodynamic processes occurring in the shock layer and on the surface of a reentry vehicle at peak heating conditions. Adapted from [11].

relaxing the translational energy mode. Additionally, as the temperature is further increased, chemical reactions begin to take place and, as mentioned before, O_2 and N_2 dissociation followed by ionisation occur, forming a partially ionised plasma. The flow consists of species which are chemically reacting, trying to achieve an equilibrium configuration through molecular collisions. Typically, at high altitudes, the time vibrational relaxation and chemical reactions need to take place are greater than the characteristic flow time, which places the flow between the limits of frozen (reaction rate constants $k_f = k_b = 0$ and relaxation time $\tau \to \infty$) and equilibrium states (reaction rate constants $k_f = k_b \to \infty$ and relaxation time $\tau = 0$), i.e., in a non-equilibrium state [10]. Furthermore, the excitation of the species internal degrees of freedom leads to the emission and/or absorption of radiation and the resulting free electrons of ionisation tend absorb the radio-frequency radiation, commonly causing the *communications blackout* [12]. Therefore, the proper consideration of chemically reacting gas is of paramount importance to accurately predict the thin shock layer temperature and its consequences.

The detached shock is of high importance in reentry flows, and it is the reason why the reentry vehicles are designed with a blunted nose. The former allows the endothermic reactions occurring inside the shock layer, among other processes, to help the gas lower its temperature before it hits the body surface, preventing this way, the complete depletion of the thermal protection system (TPS). Nevertheless, this also means the reentry body will experience a high-temperature environment due to the extreme heating originated from direct interaction between the vehicle's surface and the gas particles (convective heating) and from absorption of electromagnetic radiation emitted in the high-temperature shock layer (radiative heating) [13].

The strong favourable pressure conditions around the body and a small Reynolds number in the stagnation region delay the transition to turbulent flow and favour the assumption of laminar flow. Moreover, the thickness of the boundary layer increases in hypersonic flow and the classical concept of boundary layer fails, giving rise to a fully viscous approach. At the wall, surface chemistry may arise due to, for example, ablation, which helps the boundary layer to become more chemically reactive. These events are represented in Figure 1.2.

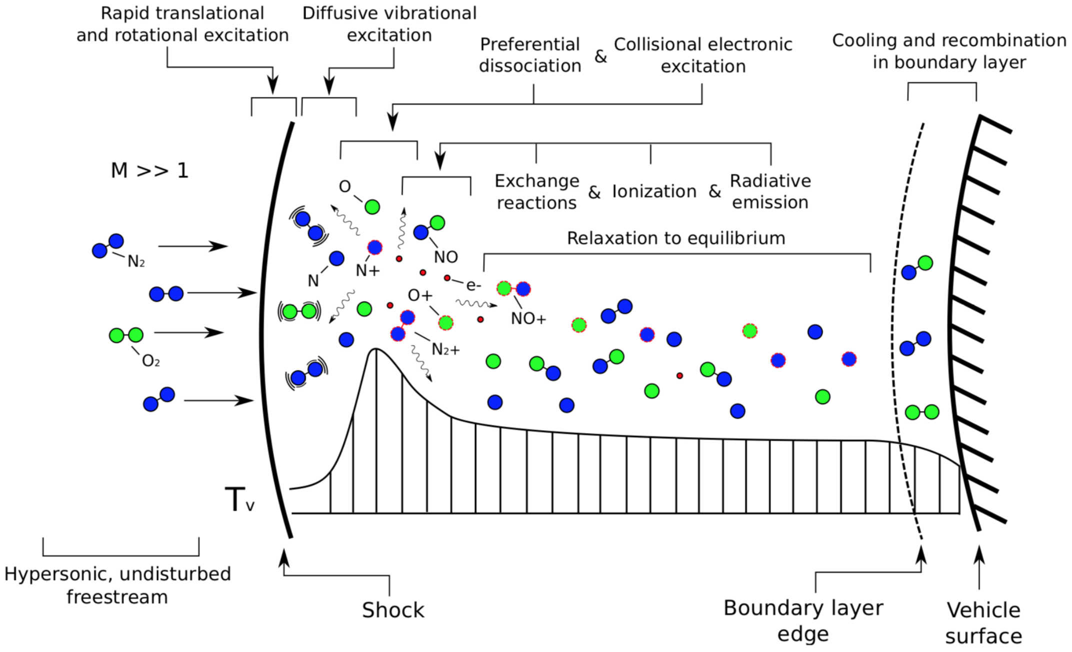

Figure 1.2: Chemical kinetic processes along the stagnation streamline for an Earth reentry [11].

High-temperature chemically reacting gas will make a difference in the lift, drag and moments of the hypersonic reentry vehicle, which, in turn, will influence the amount of flap deflection necessary to trim the body.

Downstream of the body, if the vehicle is being actively controlled by a deflected body flap, an additional shock wave is created at the wedge of the flap, which can interact with the boundary layer and with the primary bow shock (SWBLI). The subsonic portion of the boundary layer on the vehicle's surface approaching a compression ramp provides a path for the disturbances such as the increased pressure produced by the shock wave to influence the upstream flow. This upstream influence may be relatively small, e.g., a slight thickening of the upstream boundary layer, or may create a large separation bubble at the corner with a complex, lambda-shaped shock wave, as shown in Figure 1.3.

The parameters of the approaching flow that have the strongest influence on the SWBLI are: whether the flow is laminar or turbulent; Mach and Reynolds number; wall temperature; flap deflection angle and the chemical state of the gas. Hence, depending on the nature of the onset flow, different thermal and pressure loads are expected in this region [10].

SWBLI have a large impact on the design of high-speed vehicles due to the existence of extended recirculation regions and intense local heating. The presence of such interactions can lead to the loss of aerodynamic efficiency of the control surfaces. Thus, understanding the controlling effects and their

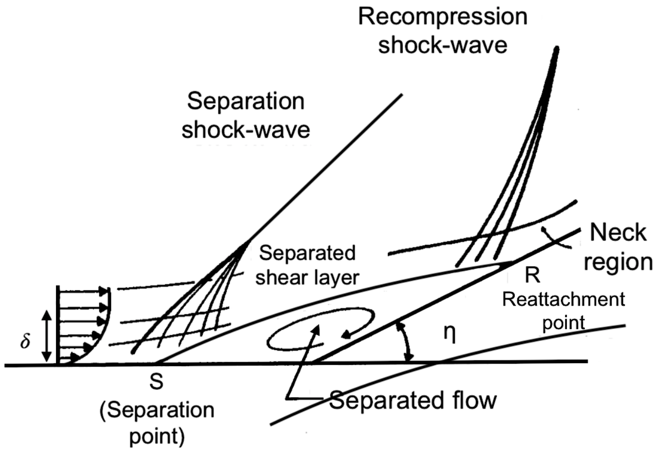

Figure 1.3: Separated-flow pattern for a SWBLI in a ramp. Adapted from [10].

quantitive characterisation is required to properly design hypersonic vehicles and their thermal protection systems [14].

1.3 Case Study

1.3.1 Reusable Launch Vehicles

In the near future, fully reusable rockets will be commonplace, suggesting a renewed emphasis on equipping upper stages[1] to correctly perform the task of guided atmospheric reentry. The difficulty lies in the fact that upper stages come back to Earth at a much higher speed than the first stage since they enter orbit on each mission in order to deploy satellites, as represented in Figure 1.4.

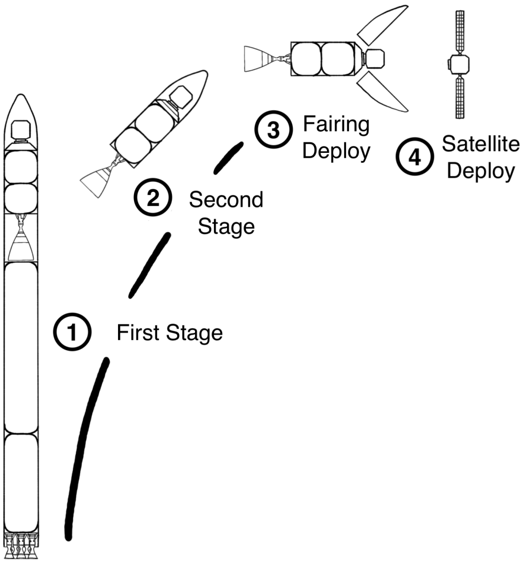

Figure 1.4: Different launch phases. Adapted from [15].

---

[1] Upper stages operate after the first stage has accelerated the vehicle to a high speed through the thickest parts of the atmosphere and has detached itself from the remaining parts of the vehicle.

This makes their return more challenging than recovering the first stage (a task currently being planned or performed by companies such as SpaceX, Blue Origin and Rocket Lab [16–18]).

New focus has also been given to small launch vehicles mainly due to the growth of CubeSat technology. These small satellites usually ride piggyback on larger missions and their launch date and orbit are always set by the primary payload, which makes the search for a suitable match difficult. Small launch vehicles aim at ending these constraints by placing small satellites into low Earth orbit (LEO) at a much higher rate, starting from the ground or from an aerial platform while drastically reducing the launch prices. Their mission objectives are generally Earth observation, education, technology demonstration and telecoms. This market generated €304 million in 2017 and it is expected to reach €6.2 billion by 2028 [19].

Hence, the geometry chosen to be aerodynamically characterised is the third stage of the European Vega launcher. This choice was based on the fact that its dimensions are within the dimensions of the upper stages of micro-launchers, the new trend in the aerospace field, and because it is the smallest among European launchers. Moreover, it is the smallest launcher with data-sheets fully available.

1.3.2 Launch Vehicle General Data

The Vega launch vehicle consists primarily of three solid propellant stages, a re-ignitable AVUM (Attitude and Vernier Upper Module) upper stage, a payload fairing and payload adapters/dispensers with different separation systems, depending on the type of mission being carried out [20].

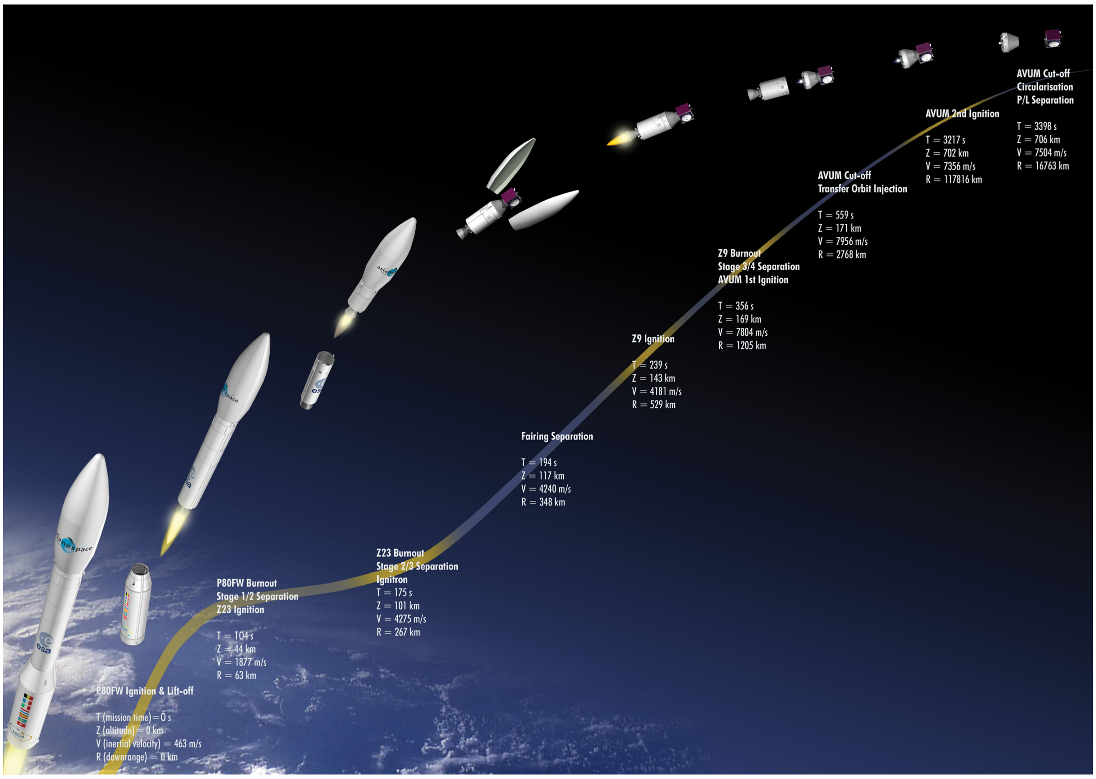

Figure 1.5: A typical Vega launch profile [21].

Figure 1.5 shows a typical mission profile for the Vega launcher and related sequence of events.

Stage 3/4 separation commonly takes place at a velocity between 7500 and 7800 $\mathrm{m\,s^{-1}}$ and at an altitude that does not exceed 215 km.

The third stage consists of a Zefiro 9 engine, with its overall characteristics and performances presented in Figure 1.6. This engine is designed to work in vacuum and thus, it cannot provide active control when entering the Earth's atmosphere.

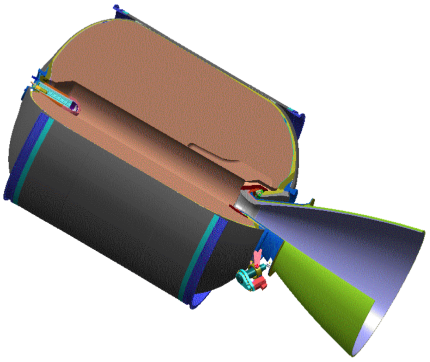

Zefiro 9	
Overall Length [m]	3.86
Diameter [m]	1.91
Propellant Mass [kg]	10115
Inert Mass [kg]	835
Nozzle Expansion Ratio	56
Nozzle Deflection Angle [°]	+/- 6

Figure 1.6: Zefiro 9 overall characteristics and performance [22].

1.3.3 Conceptual Design

Outfitting the upper stage for a guided reentry and landing would result in a weight performance penalty since the extra mass would follow the mission payload all the way to orbit. This way, flexible TPS materials are a mission enabler for large mechanically inflatable or deployable reentry system aeroshells. An inflatable aeroshell provides one alternative for protecting the nose and nozzle sides of the vehicle with a low-mass design [23–26]. This concept applied to this case would result in the geometries represented in Figure 1.7.

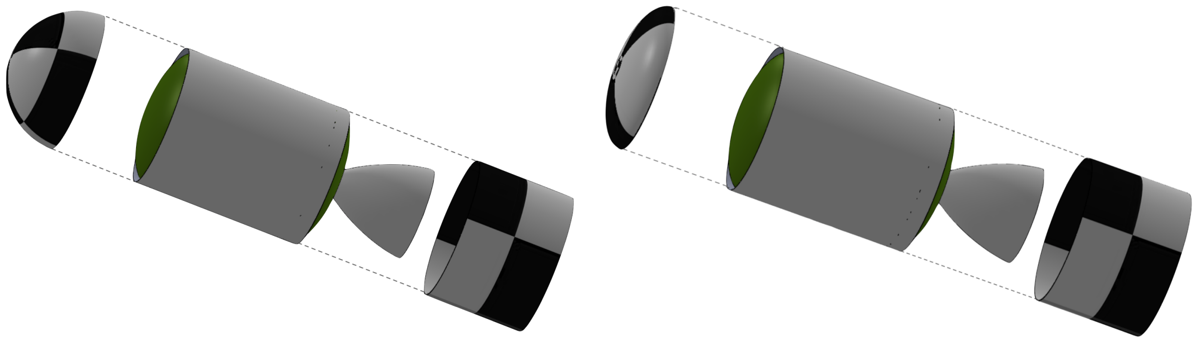

(a) Spherical nose

(b) Highly elliptical nose

Figure 1.7: Stage equipped with parashield protection with two different nose geometries.

Two different nose geometries were considered in order to assess their influence on heat flux and flap efficiency: one spherical and one highly elliptical with an eccentricity of 0.9.

Figure 1.8 presents a possible flap configuration for the upper stage, using the same deployable mechanism. Although not represented in Figure 1.8, all the simulations with the flap considered the nozzle protection system shown in Figure 1.7 with the vehicle at zero angle of attack.

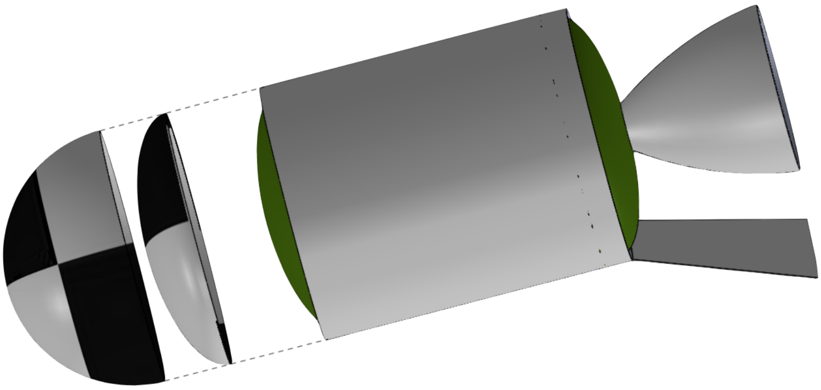

Figure 1.8: Stage equipped with control surface with two possible different nose geometries.

1.4 Objectives

As discussed in section 1.1, understanding additional options for controlling reentry and landing, such as flaps, is key to the entry, descent and landing of any mission. While experimental missions are an essential part of achieving this understanding, computational simulations are still necessary, and the most affordable way to predict the aerodynamic behaviour of reentry vehicles.

The overall aim of this thesis is to determine the aerothermodynamic characteristics of a reusable upper stage of a rocket equipped with control surfaces from numerical results obtained with SPARK (Software Package for Aerothermodynamics, Radiation and Kinetics). In order to do so, the intermediate objectives are to:

1. Identify a key trajectory point for the proper control set-up of the reentry body.
2. Compute the convective heating experienced by the reentry vehicle at the selected key trajectory point.
3. Assess the aerodynamic efficiency of the control surfaces at orbital velocity reentry conditions.
4. Generate quantitative aerodynamic and surface pressure data for future flight-test validation and aerodynamic database development.

In order to accomplish these objectives, numerical simulations were performed using the SPARK code. To compute the transport properties, two different models (Wilke and Gupta/CCS) were considered. Additionally, to account for thermal equilibrium and non-equilibrium conditions, both one and two-temperature models were used, respectively.

1.5 State-of-the-Art

The aerothermodynamic expertise needed to design and safely fly future hypersonic space vehicles is normally acquired by ground-based experimental simulation, computational predictions and ground-to-flight extrapolation methodologies. Nonetheless, if these tools have not been validated by comparisons to proper flight data, the confidence needed to ensure optimal engineering margins may be lacking. The best approach for improving confidence in aerothermodynamic design tools, both for the computational and for the ground-based experimental design tools, is to validate these tools and design approaches against flight experiments. That being said, the three main approaches to the study of the flow around a reentry vehicle are: ground-based experimental simulations, numerical simulations and flight experiments [27]. Each one of these methods present intrinsic advantages and disadvantages.

Although computational simulations are a powerful tool, they may fail to address the whole physical phenomena and still be computationally expensive. The hypersonic complex physical phenomena and the wide range of spatial and time scales present in flows containing fluid-surface interactions, entropy layers, shock waves, real-gas effects, transition and turbulence processes make the development of accurate and efficient numerical simulation methods extremely difficult. Moreover, the physics of transition and turbulence in hypersonic boundary layers are still poorly understood [28] [29]. It cannot be accurately predicted for most problems of interest and designs must rely on testing and conservatism. This way, the physical models are commonly based on approximations and lack sufficient experimental data, limiting the accuracy of the CFD (Computational Fluid Dynamics) solution.

Ground-based experimental simulations can be performed in ground test facilities. However, the high enthalpy and low density entry flow encountered by entry vehicles is still difficult to fabricate. These facilities have been, for decades, the main means for hypersonic vehicle development due to the difficulty in physically modelling non-equilibrium chemically reacting gas flow. One of the crucial problems arising from hypersonic testing is that the model scaling laws extensively used in subsonic and supersonic flows are not valid for hypersonic gas in which thermochemical reactions dominate (the reaction scale does not change when the test model is reduced in its size for wind-tunnel tests). Shock tubes, air-heated and arc-heated wind tunnels, ballistic ranges and combustion-based propulsion test facilities are some types of hypersonic test facilities developed so far in order to address various aspects of the design problems associated with hypersonic flight, and there is no single one entirely capable of duplicating the hypersonic flight environment.

Nowadays, critical designs of hypersonic vehicles are usually validated with hypersonic flight experiments, which is a more reliable tool than others on the ground. Nevertheless, it remains prohibitively expensive and time-consuming for new vehicle development [30].

Reentry Vehicles Equipped with Control Surfaces

One of the objectives of the ESA flight experiment **EXPERT** was to allow the validation of CFD tools and of methodologies for ground-to-flight data extrapolation [31]. The aerothermodynamic phenomena occurring around the vehicle, and specially around its control surfaces, was studied using experimental and numerical methods. The vehicle has an elongated conical pyramid shape flying with the nose in front and has a very small angle of attack, as shown in Figure 1.9.

It was planned to be injected with a velocity of 5 km/s at the entry gate which is defined at an altitude of 100 km, with a flight path angle of -5.5° [33]. Extensive aerothermodynamics simulations and wind tunnel tests were performed to characterise the aerodynamic behaviour in the different regions of the

Figure 1.9: EXPERT vehicle. Adapted from [32].

atmosphere: free molecular flow, transition regime and continuum regime. This ultimately led to the compilation of an aerothermodynamic database.

One of the aforementioned CFD activities was performed by Clemente et al. [34], by using the CIRA code CH3NS, considering the full 3D geometry, with the aim of analysing the SWBLI around the flap and the thermal loads associated to it. The code solves the full Reynolds-Averaged Navier-Stokes equations for a real gas as air in thermal and chemical non-equilibrium conditions by using a structured multi-block finite volume solver with a centred formulation. Flow fields have been simulated in thermal and chemical non-equilibrium laminar flow conditions with all the geometrical details and the proper thermal and catalytic modelling of the surface. The chemical kinetics model used is from Park and is characterised by reactions involving five species (O, N, NO, O_2 and N_2) in the hypothesis of absence of ionisation. The dynamic viscosity and the thermal conductivity were calculated for each single species and the viscosity and conductivity of the mixture were computed by using the semi-empirical formula of Wilke [35]. The results matched those of previous works. Kharitonov et al. [36] performed wind tunnel tests at M_∞ = 13.8, at the research Institute of Theoretical and Applied Mechanics in Russia, in order to assess what are the values for the lift, drag and pitching moment coefficients at different angles of attack [37].

In 2015, the **Intermediate eXperimental Vehicle** (Figure 1.10) was launched aboard a Vega rocket and returned to Earth subject to the same conditions as any other vehicle returning from LEO [38]. While descending in the atmosphere, its temperature and pressure sensors recorded a vast amount of information. The results are still being analysed in order to better understand the complexities of atmospheric reentry and help to design future reentry vehicles. It attained an altitude of around 412 km, allowing it to reach a speed of 7.5 km/s when reentering the atmosphere at an altitude of 120 km and with a flight path angle of 1.19 degrees below the horizontal [39, 40].

Previously to its launch, the iXV was both ground tested and computationally modelled by Roncioni et al. [39, 41] using again the CIRA code H3NS, with the physical model accounting for Eulerian and viscous laminar/transitional/turbulent flow with air in both thermo-chemical equilibrium and non-equilibrium

Figure 1.10: iXV vehicle. Adapted from [40].

at M_∞ = 15.0 (h = 58.7 km) and M_∞ = 17.7 (h = 64.6 km). Lift, drag and pitching moment coefficients were reported in function of angle of attack and flap deflection angles. Results show that in terms of heat flux distribution, the nose-fuselage zone was affected by the fully turbulence hypothesis, contrary to the flap zone region. There were no significant effects of Mach number and fully turbulent flow on aerodynamic coefficients and the aerodynamic efficiency (C_L/C_D) was reported to slightly decrease with angle of attack and flap deflection. First comparisons between experimental findings and computed results indicate a good agreement in terms of bow shock, shock layer, expansion at the junction on windward side, SWBLI in the flap area and multiple-shock interaction above the flap.

A study designed to assess the aerodynamic feasibility of a single body flap to trim the **Mars Surveyor 2001 Precision Lander** (MSPL) at a desired angle of attack, during hypersonic planetary entry, was conducted by Horvath et al. [42].

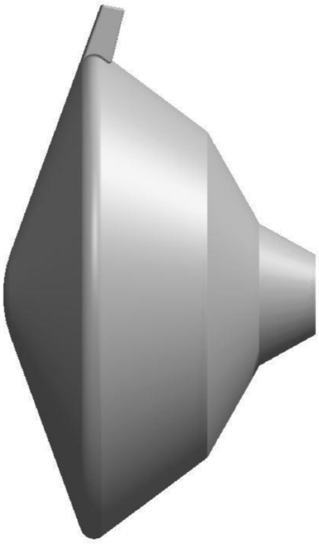

Figure 1.11: 70° sphere-cone model with flap concept [43].

The design was similar to the one presented in Figure 1.11 and both experimental and numerical studies were conducted and compared to each other. For a rapid assessment, an unstructured inviscid flow solver FELISA [44] was used. On a second level, *The Langley Aerothermodynamic Upwind Relaxation Algorithm* (LAURA) [45] was used to simulate viscous laminar Navier-Stokes flow around the body at $M_\infty = 6$. This CFD code is a three-dimensional, finite-volume solver which includes perfect gas, equilibrium and non-equilibrium chemistry models. The viscous study solved the thin-layer Navier-Stokes equations with the CF_4 gas option and the no-slip conditions were applied to the wall. Both simulations were performed without an after-body. The primary effect of the flap was to change the vehicle trim angle of attack.

The inclusion of the flaps on the MSPL was found to have no measurable effect on the aerodynamic performance (L/D), but did achieved measurable increases in axial force. The predicted minimum effect of the after-body was confirmed when numerical and wind-tunnel simulations were compared.

Past and current research has long pointed to trim tabs as an affordable and effective method to increase landed mass for planetary entry for both slender and blunt bodies. Experimental investigations of this type of configuration happened as early as 1961 for Mercury and Apollo-type entry capsules [46–48].

1.6 Thesis Outline

This thesis is structured in five main chapters, organised as follows:

After this introduction to the challenges faced during hypersonic reentry, the case-study definition and a state-of-the-art section, *Chapter 2* presents the theory needed to understand this work. It is meant to further explain the concepts of thermal and chemical non-equilibrium and to shed light on the mathematical formulation used to model high-temperature shock-layer and the models applied to compute thermal, kinetic and transport properties in order to accomplish the objectives of the study.

Chapter 3 sets the scene with respect to the numerical code and simulation parameters, together with a detailed explanation of the mesh study and simulation strategies that were conducted in order to minimise the convergence time of the solution.

Chapter 4 presents the numerical results and necessary interpretations. Comparisons between the different models used are also provided in this chapter.

At last, Chapter 5 concludes this thesis by assessing the work done and providing recommendations for future work.

Chapter 2

Mathematical Formulation

The theoretical formulation of hypersonic reentry comprises the governing equations of hypersonic and high-temperature flow, and therefore, in this chapter, emphasis will be given to the fundamental flow equations and the essential physical behaviour of chemically reacting viscous flow. From Chapter 1, Section 1.2, it became obvious that appropriate modelling is necessary to account for all the complex phenomena occurring within the high-temperature flow surrounding the reentry vehicle. To accurately model planetary entry conditions, it must be assumed that the number of collisions necessary to ensure chemical and thermal equilibrium in the chemically reacting gas has not had enough time to take place and therefore, the flow is said to be in a state of chemical and thermal non-equilibrium. Moreover, a chemically reacting gas implies a mixture of individual species, assumed to be combined into a single phase, which grants the possibility of treating its properties, such as density and viscosity, as bulk properties. The thermodynamics relations used to describe the multi-component gas is presented in Appendix A. Throughout this work, a 9 species chemistry model is used to model weakly ionised air, consisting of the following chemical species:

$$N_2, O_2, N, O, NO, NO^+, N_2{}^+, O_2{}^+, e^-$$

The basis to properly characterise this complex flow environment is the conservation equations applied to the conserved quantities of the flow, under the assumption of continuum flow. These equations take into account the aforementioned non-equilibrium state and depend on chemical-kinetic, multi-temperature and transport models. These request a further explanation, which is presented in Subsections 2.1.1, 2.1.2 and 2.3.

2.1 Non-Equilibrium Chemically Reacting Flow

2.1.1 Chemical Non-Equilibrium

When all chemical reactions are in balance and the gas does not experience any spontaneous change in its chemical composition, no matter how slow, the composition of the system is uniquely described by two thermodynamic variables, such as density and temperature. However, when the fluid passes through the shock front, pressure and temperature are rapidly increased, which changes the chemical equilibrium properties of the fluid itself. The latter will start to seek this new equilibrium state, which requires molecular collisions. Hypersonic flows are characterised by their low characteristic times, which do not allow the necessary collisions to take place and, therefore, there is a region inside the sock layer where chemical equilibrium is not yet reached, even in steady state flow conditions.

Due to chemical non-equilibrium, the gas cannot be modelled only as function of the gas state variables and chemical-kinetic models need to be applied. This requires to find the solution of one mass conservation equation per chemical species considered. In order to obtain the expression for the source term in the mass conservation equation, proper modelling of the reactions taking place must be achieved. The general chemical reaction is given as

$$\sum_i \nu'_i X_i \underset{\mathrm{k}_b}{\overset{\mathrm{k}_f}{\rightleftharpoons}} \sum_i \nu''_i X_i, \tag{2.1}$$

where ν'_i and ν''_i represent the stoichiometric coefficients of the reactants and products (X_i), respectively, k_f represents the rate constant for the forward process of the chemical reaction while k_b represents the rate constant for the backward process. The net rate of formation of species i can be given by

$$\frac{\mathrm{d}\,[X_i]}{\mathrm{d}t} = \sum_r \left(\nu''_{ir} - \nu'_{ir}\right) \left[k_{f_r} \prod [X_i]^{\nu'_{ir}} - k_{b_r} \prod [X_i]^{\nu''_{ir}}\right]. \tag{2.2}$$

$[X_i]$ represents the number of moles of species i per unit of volume of the mixture. Equation 2.2 expresses the net rate for production of the i^{th} species through reaction r.

The rate of creation or consumption of each chemical species is $\dot{\omega}_i$, the source term in the species continuity equation (Equation 2.8), computed as

$$\dot{\omega}_i = M_i \frac{\mathrm{d}\,[X_i]}{\mathrm{d}t} = M_i \sum_r \left(\nu''_{ir} - \nu'_{ir}\right) \left[k_{f_r} \prod [X_i]^{\nu'_{ir}} - k_{b_r} \prod [X_i]^{\nu''_{ir}}\right], \tag{2.3}$$

where M_i represents the molar mass of the i^{th} species.

2.1.2 Thermal Non-Equilibrium

At orbital hypersonic speeds, as the flow crosses the shock wave formed around the reentry body, its great amount of kinetic energy is converted into thermal energy as the internal degrees of freedom of the gas are excited. These degrees of freedom are reservoirs of thermal energy divided into four main thermal energy modes, as represented in Figure 2.1: translational, rotational, vibrational and electronic excitation modes. These four segregated energy modes make up the energy of each particle of the gas, which is assumed to be a collection of atoms, molecules, ions and electrons. Nonetheless, depending on the type of particle, its energy content is distributed in different modes. Molecules possess all four thermal energies, while atomic particles only have translational and electronic forms of energy. The sources of energy of the translational, rotational and vibrational modes are the translational kinetic energy of the center of mass of the particle, the rotation of the molecule about the three orthogonal axes in space and the vibration of the atoms with respect to an equilibrium location within the molecule, respectively. The energy associated to the electronic mode is related to the motion of electrons about the nucleus of atoms and it has two sources: kinetic energy, as a result of the motion of electrons, and potencial energy, due to the electrons' location in an electromagnetic force field. Free electrons only possess translational kinetic energy.

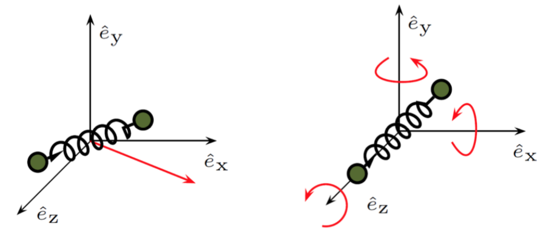

(a) Translational Mode (b) Rotational Mode

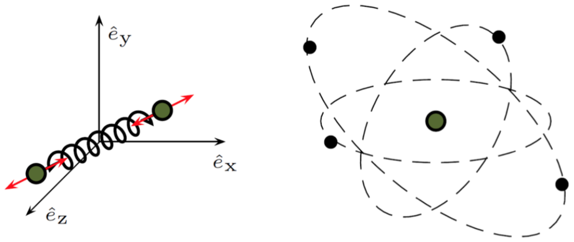

(c) Vibrational Mode (d) Electronic Excitation Mode

Figure 2.1: Different energy modes. Adapted from [49].

Atoms and molecules have three geometric degrees of freedom in translation and, consequently, three thermal degrees of freedom, since the translational velocity can be decomposed into three components. For polyatomic molecules, the number of geometric (and thermal) degrees of freedom in rotation are three, as opposed to what happens in diatomic or linear molecules. The rotational energy of these molecules about the internuclear axis (y axis in Figure 2.1) is negligibly small, and therefore the diatomic and linear molecules are said to have only two geometric as well as two thermal degrees of freedom. Atoms of a molecule vibrate with respect to an equilibrium location within the molecule and, depending on whether the molecule is diatomic or polyatomic, this can add one or more degrees of freedom to the system. Finally, the concepts of geometric and thermal degrees of freedom are usually not applied when describing electronic energy, due to the complexity of electron motion. This way, the total energy of a particle can be given as[1]

$$\varepsilon = \varepsilon_{\text{tra}} + \varepsilon_{\text{rot}} + \varepsilon_{\text{vib}} + \varepsilon_{\text{exc}} + \varepsilon_0, \tag{2.4}$$

where ε_k corresponds to the energy of each energy mode and ε_0 corresponds to the zero-point energy, a fixed quantity for a given species. From a macroscopic point of view, the specific internal energy of each species e_i is given by

$$e_i = e_{\text{tra,i}} + e_{\text{rot,i}} + e_{\text{vib,i}} + e_{\text{exc,i}} + (\Delta h_s)_i^{\circ}\,, \tag{2.5}$$

---

[1] For atoms, $\varepsilon_{\text{rot}} = \varepsilon_{\text{vib}} = 0$.

where e_k corresponds to the specific internal energy of each mode and $(\Delta h_s)_i^{\circ}$ corresponds to the effective zero-point energy. The mathematical formulation for the specific energy of each mode is provided in Appendix A.

At high altitudes, i.e., in low density regimes, the energy exchange is relatively slow when compared to the velocity of the flow. This means that the number of collisions required to achieve thermal equilibrium did not have time to happen (the relaxation times of the energy exchanges are larger than the characteristic time of the flow) and the flow domain is in thermal non-equilibrium.

In the exceptional case of thermal equilibrium, all four energy modes share a single temperature, $T_k = T$. While some regions of the flow may be properly described by this approach, others, such as the region behind a strong shock wave, where large gradients are present, may not. This way, multiple temperatures must be considered to characterise the different species thermal energy modes. When this multi-temperature approach is taken into account, the global internal energy associated to each global temperature T_k, e_k, can be given by the sum of each individual species energy associated to the k^{th} thermal mode $e_{k,i}$ as follows:

$$e_k = \sum_i c_i e_{k,i} \, , \tag{2.6}$$

where c_i represents the mass fraction of the i^{th} species.

Two-Temperature Model

The two-temperature model for non-equilibrium air flow proposed by Park [50] is used in SPARK as a compromise between the complex three temperature model and the over simplistic one temperature model, as presented in Table 2.1. This model, as the name suggests, assumes two different temperatures. The first one is the translational-rotational global temperature $T_{\text{tra-rot}}$, common to the heavy species translational and rotational modes of the molecular species, based on the fact that the energy exchange between the translational and rotational modes is extremely fast. The second temperature, $T_{\text{vib-exc}}$, is used to characterise the molecular vibrational, electron translational, and electronic excitation energies, given that the energy transfer between the translational motion of the free electrons, the vibrational motion of heavy particles and the bounded electrons in the electronic levels of atoms and molecules is very efficient. The difference of energy between electrons and heavy species in the translational mode is due to its discrepancy in mass.

Table 2.1: Multi-temperature models.

	Energy Mode				
Model	Translational		Rotational	Vibrational	Electronic Excitation
	$i = $ e	$i = $ heavy	$i = $ molecule	$i = $ molecule	$i = $ heavy
$1T$	T	T	T	T	T
$2T$	$T_{\text{vib-exc}}$	$T_{\text{tra-rot}}$	$T_{\text{tra-rot}}$	$T_{\text{vib-exc}}$	$T_{\text{vib-exc}}$
$3T$	T_{e}	$T_{\text{tra-rot}}$	$T_{\text{tra-rot}}$	$T_{\text{vib-exc}}$	$T_{\text{vib-exc}}$
$3T$	T_{e}	$T_{\text{tra-rot}}$	$T_{\text{tra-rot}}$	T_{vib}	T_{e}

Although the two-temperature approximation may not be valid in the viscous boundary layer region at the wall, this formulation allows a more tractable formulation in terms of computation of reacting flows in thermal non-equilibrium [51].

More complex models can be defined and used in high-temperature problems. However, the number of models that can be defined are limited to their physical relevance, to the increased computational effort and to the relaxation models available.

The two-temperature model choice was based on the knowledge that it is a legitimate assumption at the atmospheric reentry conditions encountered in this work [52], and on the fact that for the purpose of simulating flow fields over hypersonic reentry bodies, it allows an accurate prediction of the aerodynamic coefficients and both the radiative and convective heating of the surface of the vehicle [51].

2.2 Conservation Equations

The complete system of partial differential equations that governs non-equilibrium viscous chemically reacting flow corresponds to an extension of the traditional Navier-Stokes conservation equations. It is applied to the mass of species (chemical non-equilibrium), momentum, total energy and thermal energy (thermal non-equilibrium) variables in which continuum flow is assumed [51, 53], and intermolecular forces, present at a microscopic level, are neglected. It consists of a system of partial differential equations, formulated in terms of the independent variable ψ in the following way:

$$\underbrace{\frac{\partial}{\partial t}(\rho\psi)}_{\text{Transient term}} + \underbrace{\boldsymbol{\nabla}\cdot(\rho\psi\boldsymbol{U})}_{\text{Convective term}} = \underbrace{\boldsymbol{\nabla}\cdot\boldsymbol{J}_\psi}_{\text{Diffusive term}} + \underbrace{S_\psi}_{\text{Source term}} \tag{2.7}$$

2.2.1 Mass Conservation

Equation 2.8 represents the mass conservation equation applied to each chemical species. It takes into account the aforementioned source term $\dot{\omega}_i$, that is, the production of each chemical species.

$$\frac{\partial(\rho c_i)}{\partial t} + \boldsymbol{\nabla}\cdot(\rho c_i\boldsymbol{U}) = -\boldsymbol{\nabla}\cdot\boldsymbol{J}_i + \dot{\omega}_i\,. \tag{2.8}$$

ρ is the density, c_i is the mass fraction of the i^{th} species and $\boldsymbol{U}$ is the flow velocity vector. Considering a control volume in which a gradient in mass fraction of species i exists, J_i is the mass flux of species i, given approximately by Fick's Law as

$$\boldsymbol{J}_i \equiv \rho_i\boldsymbol{U}_i = -\rho\mathscr{D}_{im}\boldsymbol{\nabla}c_i\,, \tag{2.9}$$

where $\boldsymbol{U}_i$ is the velocity of species i and $\mathscr{D}_{im}$ is the multicomponent diffusion coefficient for species i through the mixture and is related to the binary diffusion coefficient $\mathscr{D}_{ij}$ through an expression based on the transport model being used.

Equation 2.8 equation implies that the total mass of the mixture remains constant, although the total mass of a given species may change, as imposed by the global continuity equation:

$$\frac{\partial \rho}{\partial t} + \boldsymbol{\nabla} \cdot (\rho \boldsymbol{U}) = 0. \tag{2.10}$$

2.2.2 Momentum Conservation

The conservation of momentum, which is a result of Newton's second law applied to the motion of fluids, is ensured with Equation 2.11.

$$\frac{\partial (\rho \boldsymbol{U})}{\partial t} + \boldsymbol{\nabla} \cdot (\rho \boldsymbol{U} \otimes \boldsymbol{U}) = \boldsymbol{\nabla} \cdot [\boldsymbol{\tau}] - \boldsymbol{\nabla} p + \boldsymbol{f}. \tag{2.11}$$

p corresponds to the pressure and the viscous stress tensor $[\boldsymbol{\tau}]$ is given by

$$[\boldsymbol{\tau}] = \mu \left(\boldsymbol{\nabla U} + (\boldsymbol{\nabla U})^{\mathsf{T}}\right) - \frac{2}{3}\mu \left(\boldsymbol{\nabla} \cdot \boldsymbol{U}\right)[\mathbf{I}], \tag{2.12}$$

where a Newtonian stress-strain rate relation for a fluid which obeys Stokes' hypothesis is assumed, μ is the gas viscosity coefficient and $[\mathbf{I}]$ is the identity matrix. $\boldsymbol{f}$ is the source term which represents the force density caused by any external force fields, not considered in the present work.

It is important to state that this formulation assumes that the gas moves with a global velocity $\boldsymbol{U}$, that is, as a whole. This is a practical assumption in terms of computational effort when compared to a more realistic scenario in which one vectorial momentum equation for each species is considered. Moreover, this approximation is valid when the constituent species have similar mass and ionisation is not present.

2.2.3 Total Energy Conservation

Along with the conservation of mass and momentum, the conservation of energy is also a fundamental concept of physics (Equation 2.13).

$$\frac{\partial (\rho E)}{\partial t} + \boldsymbol{\nabla} \cdot (\rho E \boldsymbol{U}) = -\boldsymbol{\nabla} \cdot \boldsymbol{q} - \boldsymbol{\nabla} \cdot (p\boldsymbol{U}) + \boldsymbol{\nabla} \cdot (\boldsymbol{U} \cdot [\boldsymbol{\tau}]) + \dot{Q}, \tag{2.13}$$

where E is the total energy per unit mass ($e + U^2/2$) and the heat flux vector is

$$\begin{aligned} \boldsymbol{q} &= \boldsymbol{q}_C + \boldsymbol{q}_D + \boldsymbol{q}_R \\ &= \sum_k \boldsymbol{q}_{C_k} + \sum_i \boldsymbol{J}_i h_i + \boldsymbol{q}_R, \end{aligned} \tag{2.14}$$

h_i is the i^{th} species enthalpy and the total energy flux,

$$\boldsymbol{q}_E = -\sum_k \boldsymbol{q}_{C_k} - \sum_i \boldsymbol{J}_i h_i - \boldsymbol{q}_R - p\boldsymbol{U} + \boldsymbol{U} \cdot [\boldsymbol{\tau}], \tag{2.15}$$

accounts for thermal conduction, transport of energy by diffusion, radiative energy emitted or absorbed by a fluid element element and rate of work done by pressure forces, shear stresses and normal stresses.

The Fourier's Law of heat conduction is used to compute the conduction heat flux $\boldsymbol{q}_{C_k}$ for each thermal energy mode as

$$\boldsymbol{q}_{C_k} = -\kappa_k \boldsymbol{\nabla} T_k \,, \tag{2.16}$$

where κ_k and T_k are the thermal conductivity coefficient and temperature associated with the k^{th} energy mode. $\boldsymbol{q}_R$ is the radiative heat flux vector, considered equal to zero in this work and $\dot{Q}$ represents the source term.

2.2.4 Non-Equilibrium Thermal Energy Conservation

To accurately model flow in thermal non-equilibrium, an additional conservation equation per non-equilibrium temperature needs to be considered (Equation 2.17). For the two-temperature model, there is only one non-equilibrium thermal energy conservation equation and it is commonly referred to as the vibrational-electronic energy conservation equation, whilst for the three temperature model in which the electronic excitation mode is in equilibrium with the free electrons' translation, this equation is split into two: the vibrational energy conservation equation and the electron-electronic energy conservation equation.

$$\frac{\partial\left(\rho e_k\right)}{\partial t} + \boldsymbol{\nabla} \cdot \left(\rho \boldsymbol{U} h_k\right) = \boldsymbol{\nabla} \cdot \left(\kappa_k \boldsymbol{\nabla} T_k - \sum_i \boldsymbol{J}_i h_{i,k}\right) + \dot{\Omega}_k, \tag{2.17}$$

e_k is the specific internal energy of the k^{th} thermal energy mode and $\dot{\Omega}_k$ is the energy-exchange source term associated with the k^{th} energy mode.

The transport coefficients $\mathscr{D}_i$, μ and κ_k will be discussed in more detail in Section 2.3.

2.3 Transport Properties

Diffusion, viscosity and thermal conduction are the physical properties of transport phenomena which become particularly important in high temperature viscous chemically reacting flows. They define the dissipative fluxes in Equations 2.9, 2.12 and 2.16, which govern the flow. These fluxes are fundamental in the modelling of transport of mass, momentum and energy through the gas, respectively [13]. Table 2.2 summarises the aforementioned dissipative fluxes and their corresponding transport coefficients, gradients and models.

Table 2.2: List of dissipative fluxes and related coefficients, gradients and models in SI units. Transport coefficients: $\mathscr{D}_i$ - diffusion coefficient of species i, μ - dynamic viscosity and κ_k - thermal conductivity associated with thermal mode k.

	Dissipative Flux		Transport Coefficient		Gradient		Model
Mass Diffusion	$\boldsymbol{J}_i$	$\mathrm{kg\,m^{-2}\,s^{-1}}$	$\mathscr{D}_i$	$\mathrm{m^2\,s^{-1}}$	$\boldsymbol{\nabla}(c_i)$	$\mathrm{m^{-1}}$	Fick's Law
Viscosity	$[\boldsymbol{\tau}]$	$\mathrm{N\,m^{-2}}$	μ	$\mathrm{kg\,m^{-1}\,s^{-1}}$	$\boldsymbol{\nabla U}$	$\mathrm{s^{-1}}$	Newtonian Fluid
Thermal Conduction	$\boldsymbol{q}_{C_k}$	$\mathrm{J\,m^{-2}\,s^{-1}}$	κ_k	$\mathrm{J\,m^{-1}\,s^{-1}\,K^{-1}}$	$\boldsymbol{\nabla}(T_k)$	$\mathrm{K\,m^{-1}}$	Fourier's Law

Determining the flow transport coefficients is required to know the behaviour of the gas towards concentration, velocity and temperature gradients. Besides the continuously changing chemistry, temperature and pressure in high temperature flow, which requires the knowledge of the altering transport properties, the possibility of ionisation introduces ambipolar diffusion, which also changes the gas mixture transport properties. This will be explained in Section 2.3.1. SPARK is able to compute these properties in real-time during a CFD simulation, using two different models based on mixing rules: the Wilke/Blottner/Eucken and the Gupta-Yos/CCS models. These simplified models substitute the classical and computationally expensive Chapman-Enskog solution of the Boltzmann equation [54].

2.3.1 Transport Models

Wilke/Blottner/Eucken Model

This model was developed in 1950 with the application of kinetic theory to the full first-order Chapman-Enskog relation [35], along with curve fits determined by Blottner et al. [55] for the species viscosities and Eucken's relation [56] for the species thermal conductivities. Wilke assumed that all binary interactions have the same (hard-sphere) cross-section. This model gives a general equation for viscosity and thermal conductivity as a function of the mole fractions, viscosities and thermal conductivities of the pure components of the mixture [57]. This way, the mixture viscosity and thermal conductivity for each global temperature are given, respectively, by the following semi-empirical relations [55]:

$$\mu = \sum_i \frac{x_i \mu_i}{\phi_{ij}} \qquad \text{and} \qquad \kappa_k = \sum_i \frac{x_i \kappa_{k,i}}{\phi_{ij}} \, , \tag{2.18}$$

where x_i is the mole fraction of the i^{th} species and ϕ_{ij} is the scale factor expressed as

$$\phi_{ij} = \sum_j \frac{x_j \left[1 + \sqrt{\frac{\mu_i}{\mu_j}} \left(\frac{M_j}{M_i}\right)^{\frac{1}{4}}\right]^2}{\sqrt{8\left(1 + \frac{M_i}{M_j}\right)}} \, . \tag{2.19}$$

M_* representes each species' (i's or j's) molar mass.

Blottner's curve fitting model [55] is then used to compute each species viscosity and is given by

$$\mu_i(T_{\text{tra},i}) = 0.1 \exp(C_i) \; {T_{\text{tra},i}}^{(A_i \ln T_{\text{tra},i} + B_i)} \, , \tag{2.20}$$

where A_i, B_i and C_i are curve fitted coefficients for each species and $T_{\text{tra},i}$ is the translational temperature of species i.

Eucken's relation [56] can be used to determine the thermal conductivity of each species for each global thermal energy as

$$\begin{cases} \kappa_{k,i} = \frac{5}{2}\mu_i c_{v_{k,i}}, & \text{if } k = \text{tra} \\ \kappa_{k,i} = \mu_i c_{v_{k,i}}, & \text{if } k \neq \text{tra} \end{cases} \tag{2.21}$$

$c_{v_{k,i}}$ represents the specific heat at constant volume of the i^{th} species for the k^{th} energy mode and is given by Equation A.19. Depending on the multi-temperature model used, in thermal non-equilibrium, the contributions of each species should be accounted for differently in the mixing rule.

Finally, the diffusion coefficient is assumed equal to all species and is given by

$$\mathscr{D}_i = \mathscr{D} = \frac{\text{Le}\ \kappa}{\rho c_p}, \tag{2.22}$$

where c_p is the gas mixture total specific heat at a constant pressure, given by Equation A.16, and the Lewis number Le, which corresponds to the ratio of thermal diffusivity to mass diffusivity, is assumed to be a constant.

Gupta-Yos/Collision Cross Section Model

The Gupta-Yos/CCS model is an approximate mixing rule which provides the transport properties required in flow field calculations, being also a simplification of the Chapman-Enskog solution [58]. This model takes into account the cross-section of each collision in the multi-component mixture and thus accounts for the true nature of the interactions between species. This way, it is assumed to be more physically accurate than the Wilke/Blottner/Eucken model [59].

The strength of the interaction between each pair of species is given by the collision terms $\Delta_{ij}^{(1)}$ and $\Delta_{ij}^{(2)}$. These terms are extensively used in this transport model formulation and are defined as

$$\Delta_{ij}^{(1)}(T_c) = \frac{8}{3}\left[\frac{2M_iM_j}{\pi R_u T_c(M_i+M_j)}\right]^{1/2} \pi\overline{\Omega}_{ij}^{(1,1)}, \tag{2.23}$$

$$\Delta_{ij}^{(2)}(T_c) = \frac{16}{5}\left[\frac{2M_iM_j}{\pi R_u T_c(M_i+M_j)}\right]^{1/2} \pi\overline{\Omega}_{ij}^{(2,2)}, \tag{2.24}$$

where R_u represents the universal gas constant. Equations 2.23 and 2.24 define the collision strength between each pair of species (i, j), as function of the controlling temperature T_c, which depends on the type of particles colliding. If the collision involves an electron, the controlling temperature used is the electron's temperature, otherwise, the heavy-species translational temperature is applied. $\pi\overline{\Omega}_{ij}$ represents the average collision cross-section in m^2 computed using Gupta's curve fits [58].

The gas mixture viscosity μ is given by

$$\mu = \sum_i \frac{x_i m_i}{\sum\limits_j x_j \Delta_{ij}^{(2)}}, \tag{2.25}$$

where m_i is the particle mass of the i^{th} species, obtained as

$$m_i = \frac{M_i}{N_A}\,, \tag{2.26}$$

and N_A is the Avogadro constant.

The translational mode κ_{tra} and electrons' κ_{e} thermal conductivities are obtained as

$$\kappa_{\text{tra}} = \frac{15}{4}k_B \sum_{s\neq e} \frac{x_i}{\sum\limits_j \zeta_{ij} x_j \Delta_{ij}^{(2)}} \qquad \text{and} \qquad \kappa_{\text{e}} = \frac{15}{4}k_B \frac{x_{\text{e}}}{\sum\limits_j \zeta_{\text{e}j} x_j \Delta_{ij}^{(2)}}\,, \tag{2.27}$$

where,

$$\zeta_{ij} = 1 + \frac{\left(1-\frac{M_i}{M_j}\right)\left[0.45 - 2.54\frac{M_i}{M_j}\right]}{\left(1+\frac{M_i}{M_j}\right)^2}\,. \tag{2.28}$$

The thermal conductivities for the other modes of energy are computed as

$$\kappa_{\text{rot}} = \sum_{i=\text{mol.}} \frac{x_i m_i c_{v_{\text{rot},i}}}{\sum\limits_j x_j \Delta_{ij}^{(1)}}\,, \tag{2.29}$$

$$\kappa_{\text{vib}} = \sum_{i=\text{mol.}} \frac{x_i m_i c_{v_{\text{vib},i}}}{\sum\limits_j x_j \Delta_{ij}^{(1)}} \tag{2.30}$$

and

$$\kappa_{\text{exc}} = \sum_{i\neq \text{e}} \frac{x_i m_i c_{v_{\text{exc},i}}}{\sum\limits_j x_j \Delta_{ij}^{(1)}}\,. \tag{2.31}$$

The global thermal conductivity of the mixture κ can be computed for thermal equilibrium and non-equilibrium conditions. For the first case, κ is simply the linear sum of Equations 2.27 through 2.31:

$$\kappa = \kappa_{\text{tra}} + \kappa_{\text{e}} + \kappa_{\text{rot}} + \kappa_{\text{vib}} + \kappa_{\text{exc}}\,. \tag{2.32}$$

In the case of thermal non-equilibrium, the thermal conductivity associated with each global temperature mode k is obtained by taking the individual contributions of each species in the aforementioned equations, in agreement with the multi-temperature model used.

The binary diffusion coefficient involving two particles is given by

$$\mathscr{D}_{ij} = \frac{k_B T_c}{p\Delta_{ij}^{(1)}}\,. \tag{2.33}$$

An averaged diffusion coefficient can be used by assuming that the multi-component mixture is a binary mixture consisting of species i and all the remaining species in the mixture as one species j:

$$\mathscr{D}_i = \frac{1 - x_i}{\sum\limits_{j \neq i} \frac{x_j}{D_{ij}}} \,. \tag{2.34}$$

For a single species, the viscosity coefficient μ is determined as

$$\mu_i = \frac{5}{16} \frac{\sqrt{\pi m_i k_B T_c}}{\pi \overline{\Omega}_{ii}^{(2,2)}} \,, \tag{2.35}$$

and the thermal conductivities are obtained as follows:

$$\kappa_{\text{tra},i} = \frac{75}{64} k_b \frac{\sqrt{\pi k_B T_c / m_i}}{\pi \overline{\Omega}_{ii}^{(2,2)}} \,, \tag{2.36}$$

$$\kappa_{\text{rot},i=\text{mol.}} = \frac{8}{3} k_b c_{v_{\text{rot},i}} \frac{\sqrt{\pi k_B T_c m_i}}{\pi \overline{\Omega}_{ii}^{(1,1)}} \,, \tag{2.37}$$

$$\kappa_{\text{vib},i=\text{mol.}} = \frac{8}{3} k_b c_{v_{\text{vib},i}} \frac{\sqrt{\pi k_B T_c m_i}}{\pi \overline{\Omega}_{ii}^{(1,1)}} \,, \tag{2.38}$$

and

$$\kappa_{\text{exc},i \neq \text{e}} = \frac{8}{3} k_b c_{v_{\text{exc},i}} \frac{\sqrt{\pi k_B T_c m_i}}{\pi \overline{\Omega}_{ii}^{(1,1)}} \,. \tag{2.39}$$

Both Wilke/Blottner/Eucken and Gupta-Yos/CCS models are valid for weakly ionised flows. However, the latter is proved to be more numerically stable and faster in terms of convergence. Moreover, the use of Wilke's model is not recommended at super-orbital entry velocities [12, 35].

Ambipolar Diffusion

In a plasma, forced diffusion to the electric field created by the charged particles is an essential contribution to the diffusional mass fluxes of the individual species relative to the mass-averaged velocity of the plasma [60]. This will enhance the diffusion of ions, which are being *pulled* by the more mobile electrons. The latter will also be slowed down by the ions and finally, they will end up diffusing at the same velocity, mainly established by the heavier species. Given the fact that the electric-static forces are not being accounted for in the conservation equations, ambipolar corrections should be taken into account when computing the charged particles diffusion fluxes.

Chen [61] shows that, for ions, the ambipolar diffusion coefficient (superscript a) is determined as

$$\mathscr{D}_{\text{ion}}^a = \left(1 + \frac{T_\text{e}}{T_\text{ion}}\right) \mathscr{D}_{\text{ion}} \,, \tag{2.40}$$

where $\mathscr{D}_{\text{ion}}$ is the ion free diffusion coefficient, and T_e and T_ion are the translational temperatures of the electrons and ions, respectively. In thermal equilibrium conditions ($T_\text{e} = T_\text{ion}$), Equation 2.40 becomes $\mathscr{D}_{\text{ion}}^a = 2\mathscr{D}_{\text{ion}}$.

For electrons, when a single ionic species is considered, $\mathscr{D}_\text{e}^a$ is equal to $\mathscr{D}_{\text{ion}}^a$. Otherwise, the effective diffusion coefficient of electrons can be obtained by letting the average diffusion velocity of ions be equal to the diffusion velocity of electrons [62]. This way,

$$\mathscr{D}_{\text{e}}^{a} = M_{\text{e}} \frac{\sum\limits_{i=\text{ion}} \mathscr{D}_i^a x_i}{\sum\limits_{i=\text{ion}} M_i x_i} \, . \tag{2.41}$$

2.4 Aerodynamic Forces and Moments

2.4.1 Coordinate Systems

The forces and moments and hence, the equations of motion, are defined in specific coordinate systems. In general, two coordinate systems are used: the body-fixed system and aerodynamic (air-path) system, as depicted in Figure 2.2.

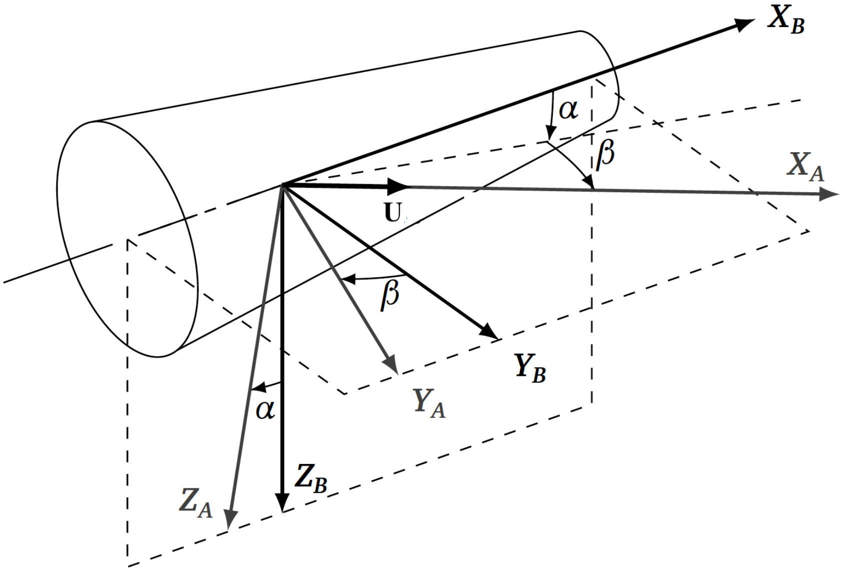

Figure 2.2: Body-fixed coordinate system (index B) and aerodynamic coordinate system (index A), [63].

The transformation from the body-fixed coordinate system to the aerodynamic coordinate system is related to the angles of attack α and of sideslip β. The angle of attack is assumed positive for a nose-up attitude and the angle of sideslip is defined positive for a nose-left attitude, as it is depicted in Figure 2.2. Matrix 2.42 performs the coordinate transformation of a vector in the body-fixed reference frame (X_B, Y_B, Z_B) into a vector in the aerodynamic coordinate system (X_A, Y_A, Z_A).

$$\begin{aligned} \mathbf{Q}^{A/B} &= \begin{bmatrix} \cos\beta & \sin\beta & 0 \\ -\sin\beta & \cos\beta & 0 \\ 0 & 0 & 1 \end{bmatrix} \begin{bmatrix} \cos\alpha & 0 & \sin\alpha \\ 0 & 1 & 0 \\ -\sin\alpha & 0 & \cos\alpha \end{bmatrix} \\ &= \begin{bmatrix} \cos\beta\cos\alpha & \sin\beta & \cos\beta\sin\alpha \\ -\sin\beta\cos\alpha & \cos\beta & -\sin\beta\sin\alpha \\ -\sin\alpha & 0 & \cos\alpha \end{bmatrix} \end{aligned} \tag{2.42}$$

The transformation matrix from frame A to frame B is simply given by

$$\mathbf{Q}^{B/A} = \left[\mathbf{Q}^{A/B}\right]^T . \tag{2.43}$$

2.4.2 Forces and Moments

Aerodynamic forces and moments on a body are obtained by integrating the normal (superscript N) and tangential stresses (superscript S) acting on the body. When the fluid around a closed surface is not static, the pressure varies around it. The sum of the pressure (static), which acts locally normal to the body surface, times the area around the body produces a net force. In a viscous computation, shear stresses come into play and are caused by friction between the body and the molecular layer of air just adjacent to the body surface and, as opposed to the pressure forces, they act locally tangential to the surface. Therefore, pressure and shear stress are distributed loads acting on the body and when integrated over the complete surface area of the vehicle give rise to the resultant aerodynamic force vector. These are the two fundamental (and only) sources of aerodynamic force.

Forces in the body-fixed coordinate system are defined as

$$\boldsymbol{F} = \boldsymbol{F}^N + \boldsymbol{F}^S, \tag{2.44}$$

where, for a closed surface,

$$\boldsymbol{F}^N = -\int\int_S (p - p_\infty)\,\hat{\boldsymbol{n}} dS \qquad \text{and} \qquad \boldsymbol{F}^S = \int\int_S \boldsymbol{\tau} dS, \tag{2.45}$$

and p_∞ corresponds to the upstream pressure, $\hat{\boldsymbol{n}}$ corresponds to the unit normal vector and $\boldsymbol{\tau}$ is the shear stress vector. Force coefficients are defined as

$$\boldsymbol{C}_F = \boldsymbol{C}_F^N + \boldsymbol{C}_F^S, \tag{2.46}$$

where

$$\boldsymbol{C}_F^N = -\frac{1}{A_{ref}}\int\int_S C_p \hat{\boldsymbol{n}} dS \qquad \text{and} \qquad \boldsymbol{C}_F^S = \frac{1}{\frac{1}{2}\rho_\infty U_\infty^2 A_{ref}}\int\int_S \boldsymbol{\tau} dS. \tag{2.47}$$

C_p is the pressure coefficient, defined as

$$C_p = \frac{p - p_\infty}{\frac{1}{2}\rho_\infty U_\infty^2}, \tag{2.48}$$

where A_{ref} denotes the reference area used to compute the force and moment coefficients, ρ_∞ corresponds to the upstream density and U_∞ is the upstream velocity.

Moments about a point with position vector $\boldsymbol{r}$ are given as

$$\boldsymbol{M} = \boldsymbol{M}^N + \boldsymbol{M}^S, \tag{2.49}$$

where

$$\boldsymbol{M}^N = -\int\int_S p(\boldsymbol{r} \times \hat{\boldsymbol{n}})dS \qquad \text{and} \qquad \boldsymbol{M}^S = \int\int_S \boldsymbol{r} \times \boldsymbol{\tau} dS. \tag{2.50}$$

Moment coefficients are defined as follows,

$$\boldsymbol{C}_M = \boldsymbol{C}_M^N + \boldsymbol{C}_M^S \tag{2.51}$$

where,

$$\boldsymbol{C}_M^N = -\frac{1}{A_{ref}c_{ref}} \int\int_S C_p(\boldsymbol{r} \times \hat{\boldsymbol{n}})dS \qquad \text{and} \qquad \boldsymbol{C}_M^S = \frac{1}{\frac{1}{2}\rho_\infty U_\infty^2 A_{ref}c_{ref}} \int\int_S \boldsymbol{r} \times \boldsymbol{\tau} dS. \tag{2.52}$$

c_{ref} denotes the reference chord used in defining the moment coefficients.

The coefficients of lift C_L, drag C_D, and side-force C_Y are obtained in the aerodynamic reference frame through the use of the transformation matrix given by Equation 2.42 [64].

$$\begin{bmatrix} -C_L \\ -C_D \\ C_Y \end{bmatrix} = \begin{bmatrix} -\sin\alpha & 0 & \cos\alpha \\ \cos\beta\cos\alpha & \sin\beta & \cos\beta\sin\alpha \\ -\sin\beta\cos\alpha & \cos\beta & -\sin\beta\sin\alpha \end{bmatrix} \begin{bmatrix} C_{FX_B} \\ C_{FY_B} \\ C_{FZ_B} \end{bmatrix} \tag{2.53}$$

The equations for aerodynamic coefficients are for steady state only.

Another critical aspect of hypersonic flight is that the pressure distribution over the vehicle or control surfaces is significantly affected by the variation in the ratio of specific heats γ [65]. This is due to the fact that γ, which is also the isentropic exponent, influences the rate of compression or expansion of the flow. On the other hand, this rate influences the setting of the control surfaces, namely the angle of attack needed to trim the vehicle, which is usually larger than the one computed for perfect gas. The problem described above was observed during the first Space Shuttle reentry. Pressure distribution calculations had been done along the windward side of the Shuttle both for a non-reacting perfect gas boundary layer (γ = 1.4) and for a chemically reacting flow. Although the results were found to be very similar, when integrated over the vehicle surface, a net moment that provided additional pitch-up to the vehicle nose was produced. Other explanations have been presented for this additional pitch-up, which illustrates how interacting physical phenomena are different to isolate.

Chapter 3

Numerical Setup

A detailed description of the CFD solver used is first introduced in this chapter, followed by the justified selection of the trajectory point being simulated. A subsequent mesh and convergence study is provided in which the best mesh configuration is selected. Numerical and convergence issues are also discussed in this chapter.

3.1 CFD Solver

SPARK, the *Software Package for Aerothermodynamics, Radiation and Kinetics* [66], is the CFD code used to simulate multi-dimensional hypersonic flow, maintained at the University of Illinois at Urbana-Champaign and Instituto de Plasmas e Fusão Nuclear (IPFN, Institute for Plasmas and Nuclear Fusion) and it is the sole Aerothermodynamic tool available in Portugal [67]. Unlike most numerical tools, SPARK implements various levels of independent physical models and numerical techniques in a unified framework that shares the same data structure, offering more flexibility and extendability. Given the exceptionally multi-physics nature of high-temperature and high-velocity flows, the aforementioned design characteristics become important. The code is capable of performing Euler or Navier-Stokes compressible flow simulations in 0D (temporal relaxation), 1D (post-shock relaxation) or 2D (cylindrical or axisymmetric). It is coded in Fortran 03/08, taking advantage of object-oriented programming techniques and high computational efficiency. Treating each physical quantity and physical model as an object enables the separation of physical models, numerical methods and mesh-related operations. Mesh grids can be generated using any external CFD software available to the user.

The SPARK code is capable of using both a multi-temperature and a state-to-state approach, which allows to simulate the typical non-equilibrium conditions experienced at high altitudes during reentry. Frozen or perfect gas conditions can be chosen as the gas model, as well as a more detailed chemically reacting mixture, which employs chemical kinetic models. Catalytic effects can also be selected to simulate atom recombination at the wall. Furthermore, it provides mesh refinement tools for shock and/or boundary layer capturing. It is a structured, second-order finite volume code and the method used to solve the conservation equations can either use an explicit or implicit time discretisation scheme. In order to run simulations, a key-word based input file must be filled in with the relevant simulation parameters.

No turbulence model is currently implemented in SPARK and, therefore, the flow is assumed to be laminar over the whole reentry body. This assumption is mostly valid in the stagnation region where the favourable pressure gradients experienced by the flow over the vehicle geometry and the low Reynolds numbers due to the strong viscous effects delays the transition to turbulent flow [68].

3.2 Trajectory Point

When selecting the free-stream conditions for the CFD simulation, special attention needs to be given to the limits of the physical models employed in the numerical code. The Knudsen number is a relevant dimensionless quantity which gives a numerical account of whether or not the continuum hypothesis can be applied [69]. It is also of particular interest when assessing the *no-slip boundary condition*, in which the flow directly in contact to the wall is assumed not to move. That is, the conventional viscous flow no-slip conditions begin to fail at a certain altitude, depending on the body geometry. The value that is commonly taken as the threshold so that continuum flow and the no-slip condition can be considered is 10^{-3} [70, 71]. As these slip effects start taking place, the governing equations of the flow are still assumed to be the usual continuum-flow equations, apart from the proper velocity and temperature-slip conditions employed as boundary conditions. Nonetheless, as the altitude continues to increase, a point is eventually reached where the continuum-flow equations themselves are no longer valid and, in order to predict the aerodynamic behaviour, methods from kinetic theory must be used. For Knudsen numbers much greater than 10^{-1}, most of the gas flow must be characterised using statistical methods since there is no continuum [72]. Figure 3.1 allows to visualize the different flow regimes and the Knudsen numbers associated to them.

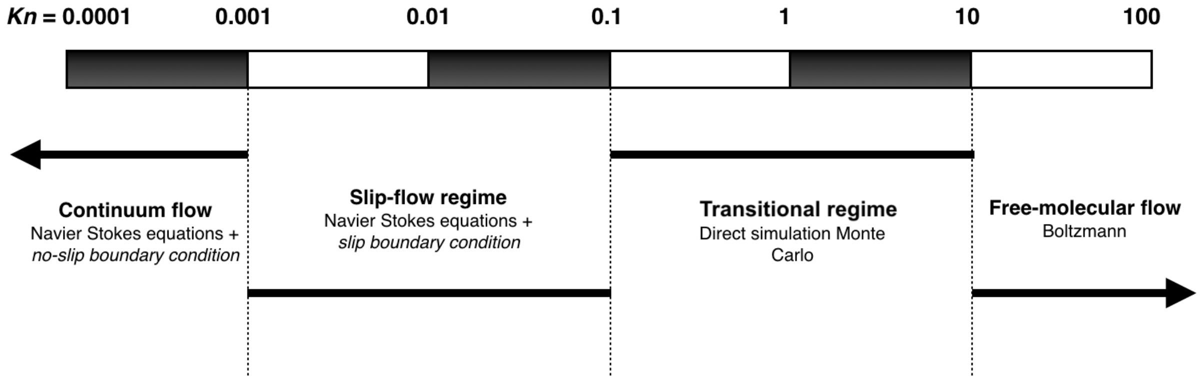

Figure 3.1: Different flow regimes.

This dimensionless number is computed using the following equation:

$$K_n = \frac{k_B T_\infty}{p_\infty \sqrt{2}\sigma l}, \tag{3.1}$$

where k_B is the Boltzmann constant, p_∞ is the free-stream pressure, σ is the collision effective cross-section, taken as 0.4 $\times 10^{-18}$ m^2 for the Earth's atmosphere, and l is the characteristic dimension of the reentry body, here taken as the volume of the body divided by its surface area.

While in the vacuum of space, the upper stage rocket can orient itself using its movable nozzle adapted to vacuum conditions. When it reaches the upper layers of the atmosphere, its nozzle can no longer perform its job and the rocket stage needs to rely on its control surfaces to land on a dedicated area. The conditions at 60 km were chosen to be simulated since it is the maximum altitude that can be chosen which takes advantage of the continuum flow with no-slip boundary condition assumption, while having a free-stream pressure more than 20 times higher than, for example, at an altitude of 80 km. Moreover, heat loads are expected to be higher at 60 km than at any other point earlier in the trajectory. Also taking advantage of the ballistic geometry of the vehicle, the velocity attained while delivering its intended payload is very likely to be preserved at this altitude of the trajectory.

Table 3.1: Point simulation parameters.

h [km]	U_∞ [km s^{-1}]	a_f [m/s]	p [Pa]	T [K]	ρ [kg m^{-3}]	K_n	M$_\infty$	x_{N_2}	x_{O_2}	T_{wall} [K]
60	7.60	315.06	21.96	247.00	3.096×10^{-4}	0.001	24	0.79	0.21	1200

The values in Table 3.1 were obtained from the US Standard Atmosphere, 1976 [73]. The Knudsen number is found to be within the threshold for continuum flow with no-slip condition and therefore, the non-equilibrium partial differential Navier-Stokes equations can be used.

3.3 Mesh and Convergence Study

3.3.1 Numerical Issues

A preliminary simulation in chemical non-equilibrium was performed in order to assess the location and shape of the shock wave, which allowed to reduce the area outside the shock layer. Mesh refinement at the wall is extremely important to accurately predict the aerodynamic characteristics of the reentry body and therefore, that was the main aspect taken into account when constructing the mesh, while also trying to keep the skewness equiangle value below 0.55. Nonetheless, high-speed flows present a wide range of numerical challenges. These are primarily associated with capturing high gradients and discontinuities, characteristic of strong shock waves and shear layers. When trying to assess the quality of the adapted mesh (shorter and with refinement) by changing the number of grid cells that could accurately capture these phenomena, some unacceptable results were obtained, which can be attributed to the *carbuncle* phenomenon. This anomaly makes the structure of numerically captured shock waves to become widely distorted and it is most noticeable in CFD simulations within the blunt nose region on axisymmetric grids [74]. Although this problem represents a numerical instability closely related to the Euler part of the fluid equations which govern compressible flows (convective terms), relying on the diffusive terms present in the Navier-Stokes equations to damp the instability is not sufficient. As a result, different approaches in the mesh construction phase had to be considered to circumvent the problem presented in Figure 3.2 (a). Pandolfi and D'Ambrosio [75] suggest to pay special attention to the aspect ratio of the grid cells directly in contact with the normal part of the shock wave. If the side of the grid cell tangential to the shock front is highly elongated, the time step used to solve the conservation equations for that specific cell will be smaller than the one which should be necessary. Thus, additional numerical diffusion is introduced into the fluxes across these kind of surfaces, lessening the carbuncle effect. This way, the solution found to overcome this problem consisted of reducing the tangential refinement in the nose region, which, for the elliptical nose geometry, resulted in the solution depicted in Figure 3.2 (b).

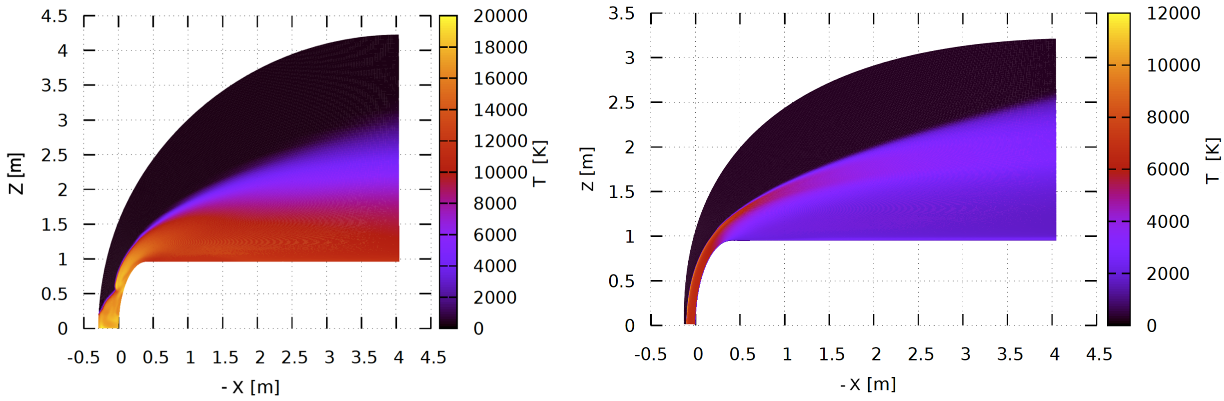

(a) Carbuncle instability. No fix applied.

(b) Carbuncle instability solved.

Figure 3.2: One example of *carbuncle* encountered in this work.

3.3.2 Boundary Conditions

Wall Catalycity

Heating to hypersonic vehicles during flight is not only governed by the state of the flow around the vehicle, but also by the chemical or species boundary conditions. The surface may chemically react with the flow surrounding the vehicle, that is, the surface may be consumed or transformed (i. g. ablation). However, it is out of the scope of this work to consider a surface that undergoes chemical changes. Alternately, a surface (wall) which is *catalyst* regarding reactions of the ambient species in the non-equilibrium flow adjacent to the reentry body is considered.

When atoms hit the surface of a material, they may react to form molecules while releasing some or all of their heat of dissociation. *Catalytic* is a chemical term used to commonly describe materials capable of enhancing the rate of reactions or changing the equilibrium constant [76]. This comes as a disadvantage during reentry or hypersonic flight, since by giving up their latent heat of dissociation, molecules increase the heating of the surface.

In SPARK, the wall boundary condition can be set to non-catalytic, in which case it is assumed that there is no atom recombination at the surface and therefore, the wall is not affected by the flow surrounding the vehicle, or to catalytic, where it is assumed that atoms recombine to some extent at the wall. A fully catalytic boundary condition can be chosen to model the assumption that all atoms colliding with the surface will recombine to form molecules and thus, it imposes at the wall the chemical composition of the free-stream. The latter represents the worst case scenario in terms of heating to the surface. The three possible scenarios are represented in Figure 3.3.

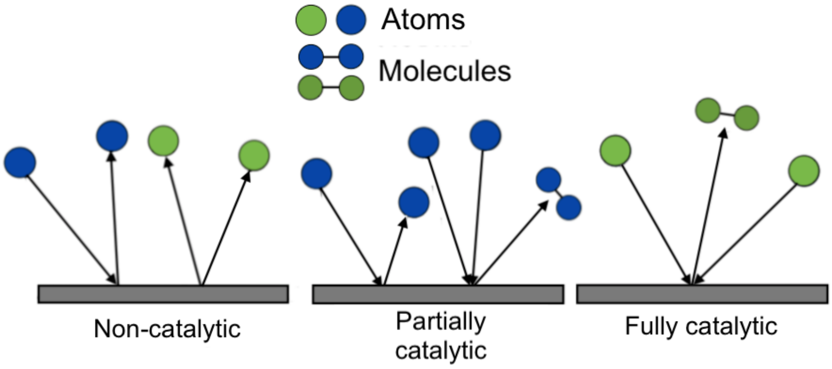

Figure 3.3: The effect of surface catalycity on atom recombination at the wall.

The boundary conditions considered for the CFD domain are thus the ones represented in Figure 3.4, which include a fully catalytic and isothermal wall with its temperature set to T_w = 1200 K [77].

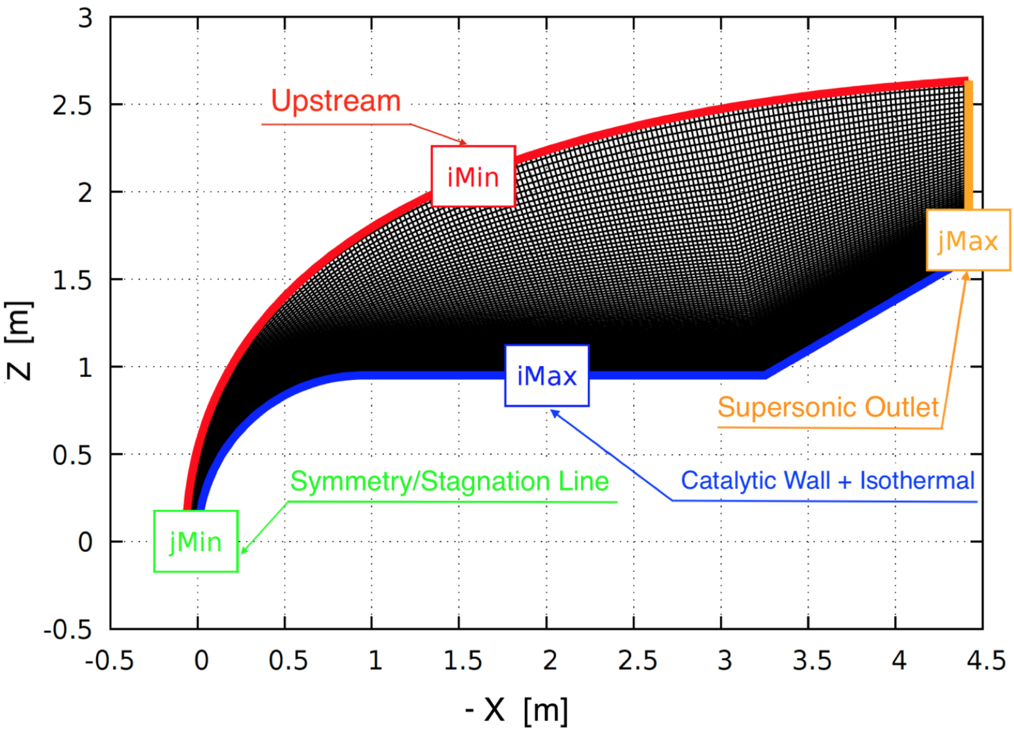

Figure 3.4: CFD boundary conditions for a 150x200 mesh configuration.

These parameters were defined in the input file needed to start the simulation in SPARK. The structure of this file is presented later on in Section 3.4.

3.3.3 Mesh Fine-tuning

The next step consists of varying the number of cells in the normal direction to the wall (Ni) in order to assess which is the best configuration that allows to accurately capture the strong gradients experienced by the flow. Four different mesh resolutions were tested for the spherical nose geometry (60×200, 90×200, 105×200 and 150×200) with the same refinement near the wall and the results obtained for the temperature and pressure profile along the stagnation line are represented in Figure 3.5. These results considered thermal equilibrium and the Gupta-Yos transport model.

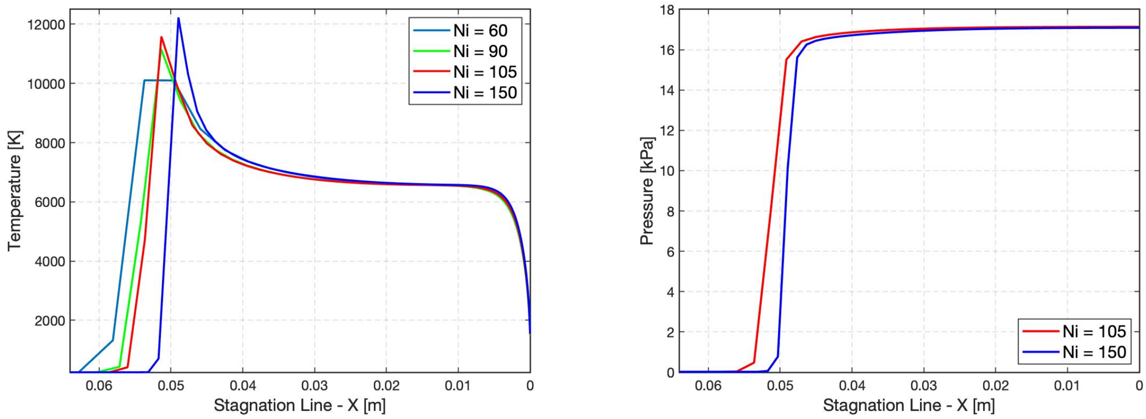

(a) Stagnation line temperature

(b) Stagnation line pressure

Figure 3.5: Temperature and pressure profiles along the stagnation line for different number of cells normal to the wall.

Figure 3.5 (a) clearly shows that the mesh with 60 cells along the stagnation line is too rough to be considered in further simulations. Although predicting the conditions at the shock front is not as important as accurately predicting the boundary-layer conditions, this mesh configuration does not show a temperature peak associated to the shock region. Moreover, the lowest temperature achieved behind the shock front is 12% higher when compared to the 150×200 mesh configuration. The mesh configurations with 90 and 105 cells along the stagnation line, also when compared to the 150×200 mesh, seem to underestimate the same temperature in 3.1% and 2.0%, respectively, the shock position up to 2.4×10^{-3} m, and the temperature peak up to 8.4%. Taken into account the pressure profile in Figure 3.5 (b) a difference of 0.3% in pressure peak is found between the two most computationally expensive configurations.

Higher refinements were considered, however, they were too computationally expensive and the time needed until convergence was considerably higher, which deemed these solutions unpractical.

The number of cells along the body was not increased since doing so would be prohibitively computationally expensive as it would increase the convergence time to several months.

Among the options provided and taken all these factors into account, the mesh that is accepted to accurately predict the pressure, temperature profiles and, consequently, the heat flux and forces at the surface of the vehicle is the one with Ni = 150 cells.

The same study was performed for the highly elliptical nose geometry using four different mesh configurations (100×175, 120×175, 160×175 and 195×175), yielding Ni = 195 cells. The shock front moved 0.0513 m along the stagnation line when compared to the spherical geometry, which translates to a thicker shock layer, resulting in the need for a greater number of cells.

3.4 SPARK Input File

In order to launch SPARK and run the simulations, a key word-based input file must be provided with the initialisation parameters. The file structure is presented in this section:

```
Start(Spark)

 Start(Gas)
    Gas_Model = Frozen_Gas/Perfect_Gas/Nonequ_Gas
    Flow_Type = Euler/Navier_Stokes
    Species   =  N2, O2, NO, N, O, N2+, O2+, NO+, e-
    Kinetic   =  Air11-Park2001
    TransportModel = Wilke/Gupta_Yos
    Start(Gas_State)
      Start(Upstream)
        Pressure          =   21.96
        Temperature       =   247.00
        Velocity          =   7600.00
        Mole_fractions    =   N2:0.79  , O2:0.21
      End(Upstream)
    End(Gas_State)
    Start(Multitemperature)
        Nonequ_Model = T_Tev
        Electronic_Nonequ_Model = Translation_Excitation_Vibration
    End(Multitemperature)
  End(Gas)

  Start(Simulation)
    Simulation_Type       =   2D_PLAN/2D_AXI
  End(Simulation)

  Start(Solver)
    Time_Discretization = Explicit/Implicit
    StopCondition( Iter = __ )
    cfl( __ )
```

```
  End(Solver)

  Start(BoundaryConditions)
    Upstream( iMin  )
    Wall( iMax  , Tw = 1200.00)
    Symmetry( jMin  )
    SupersonicOutlet( jMax  )
  End(BoundaryConditions)

End(Spark)
```

To summarize,

- The **gas model** determines the flow type and it can be set to frozen or perfect in equilibrium conditions. It can also be set to non-equilibrium conditions.
- The **flow type** defines the set of equations to be solved by the code.
- The **transport model** object determines the model being used to compute the transport properties.
- The **species** defines, as the name suggests, the species involved in the chemical reactions occurring within the flow.
- The **kinetic scheme** specifies the kinetic parameters.
- The **gas state** defines the gas upstream and initial conditions, depending on the trajectory points being considered.
- The **non-equilibrium model** assigns the multi-temperature model to be used in the simulation. The thermal relaxation models used are:

  - Vibration-Chemistry: Candler 1989 [78].

  - Vibration-Translation: Millikan-White-Park [79], [80]

  - Electron-Translation: Appleton et al. [81], [82].

3.5 Simulation Strategy

The root-mean-square value of the residual of the system of equations allows to evaluate the convergence of the solution. In this work, the solution was considered converged when the residual dropped below 10^{-4} or 10^{-5}, for the mesh study or for further simulations, respectively. Given the unusual large size of the reentry body being simulated in SPARK and therefore, the great number of mesh cells required to achieve meaningful results, the large time interval between each iteration results in converge times up to several months if no simulation strategy is implemented. The most effective method to reduce convergence time is to consider an implicit time discretisation, which often made the simulation crash. Hence, using an explicit time discretisation to begin with, all the simulations started with chemical non-equilibrium Euler flow and were then changed to viscous (Navier-Stokes) flow after the shock wave position had stabilised. The rationale of replacing the Navier-Stokes equations with Euler equations, in a first stage, is the fact that, in a domain far from the wall, the transport properties such as the molecular viscosity, thermal conductivity and diffusion are less significant in comparison with the inertia of the fluid motion [83]. Although the Gupta-Yos model implementation has only been used with the Wilke model as the baseline, no clear or significant advantage was taken from this specific action.

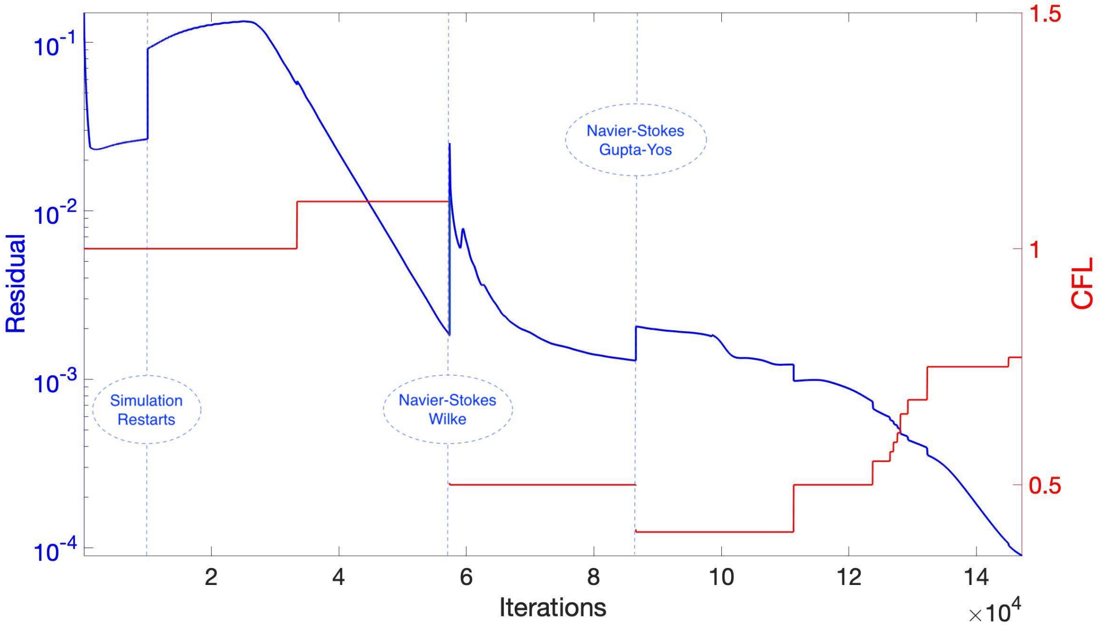

Figure 3.6: Residual and CFL profiles of an explicit simulation.

Figure 3.6 presents the strategy implemented in a simulation in thermal equilibrium and for an explicit time discretisation. As expected, the residual increases when the flow type is changed from reactive Euler to Navier-Stokes with the Wilke transport model due to the addition of viscosity to the equations being solved by the code. Later on, the change to the Gupta-Yos transport model only increases the residual slightly, which stabilises for a few iterations before continuing its decrease. The CFL was changed several times during the simulation which, besides changing the residual dramatically, also changed the slope of the residual's curve.

For some simulations it was possible to change to an implicit time discretisation when the residuals were lower than $5{\times}10^{-3}$ and the flow type was set to Navier-Stokes. This allowed to continually vary the CFL from 1 to values as high as 50, which reduced the convergence time to just a few thousand iterations (e.g. 2000 in one case).

Chapter 4

Results

The impact of the transport and multi-temperature models and the nose geometry is first analysed in this chapter. Secondly, the force and moment aerodynamic coefficients for the reentry vehicle predicted by the simulations are presented.

4.1 Thermal Equilibrium

4.1.1 Impact of Transport Model

Figures 4.1 (a) and (b) illustrate the stagnation line temperature profile and wall heat flux for the two mixing rules discussed in Chapter 2, for the spherical geometry. All reported heating results are convective only, which consists of a conduction and a diffusive component, determined by the temperature and mass fraction gradients, respectively. The contribution from radiation was not expected to be dominant, as in the case of objects travelling at super-orbital speeds (in which radiative heating mostly depends on the excited species), and therefore it was excluded from the analysis.

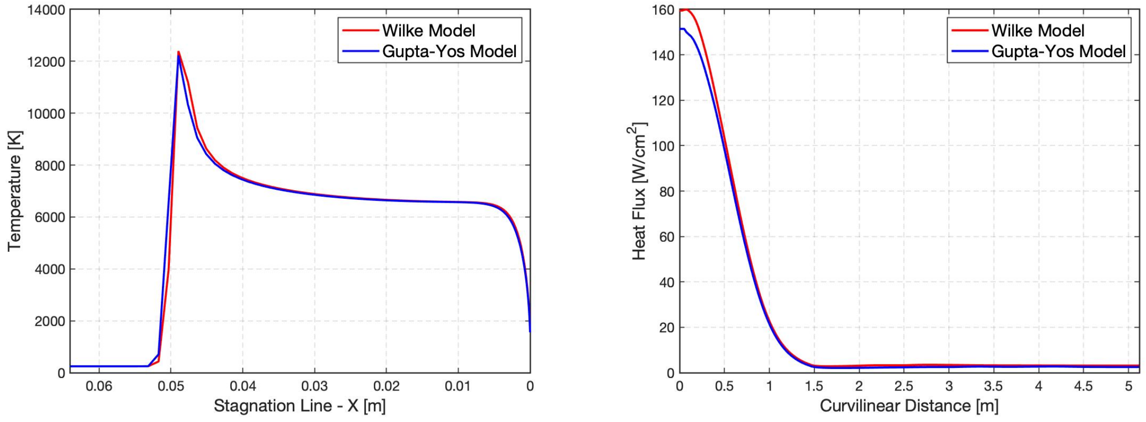

(a) Stagnation line temperature

(b) Wall heat flux

Figure 4.1: Temperature along the stagnation line and wall heat flux for the Wilke and Gupta-Yos transport models.

A thorough analysis of the results shows how the two models agree well at the velocity considered in this work. The greatest discrepancy is found at the bow shock region, which is already expected due to the roughness of this area. The Wilke model estimates the peak temperature to be 1.4% higher when compared to the Gupta-Yos model. Moreover, the lowest temperature achieved behind the shock is 1.5% higher in the Wilke case. Consequently, the heat flux in the nose region is 5.1% lower for the Gupta-Yos model with respect to the Wilke case, resulting in an almost perfect agreement after this region. The slight disturbances found in the nose area also suggest that the carbuncle problem was not completely eradicated, even though the different measures discussed in Section 3.3 were applied. Furthermore, the heat flux at the stagnation point for both models yields higher results than the semi-empirical Sutton-Graves relation[1] [84], which predicts a stagnation heat flux of 138 $\mathrm{W\,cm^{-2}}$. This is expected since this relation assumes chemical equilibrium.

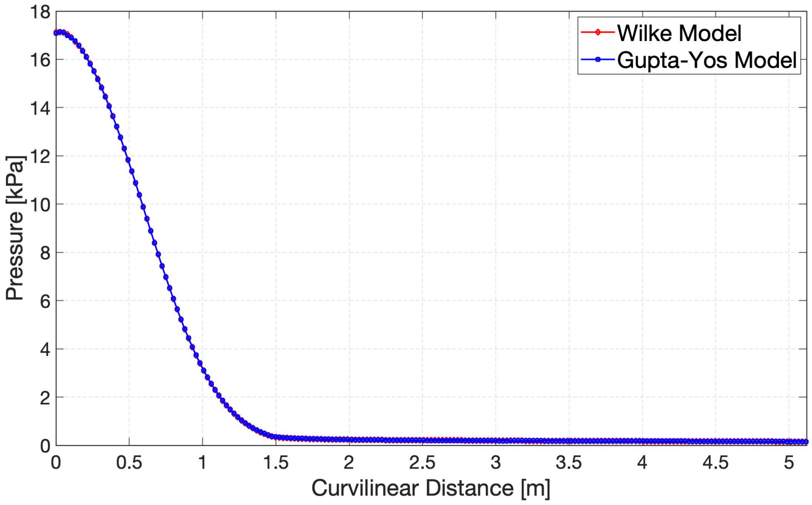

Figure 4.2: Wall pressure distribution, η = 0°.

Figure 4.2 shows that the pressure at the stagnation point for the Wilke model is slightly higher (0.23%) when compared to the Gupta mixing rule.

Figure 4.3 presents the results obtained for the electron mole and mass fractions along the stagnation line. The greatest discrepancies are found at the wall, whereas in the shock layer the two models seem to agree almost entirely. This was expected since the gas is weakly ionised (assumption shared by the two mixing rules) for the conditions being simulated in this work.

The Gupta-Yos/CCS model is assumed to be more physically accurate given that this mixing rule takes into account the cross-section of each collision in the multi-component mixture and thus accounts for the true nature of the viscosity collision integrals. Hereupon the results are based on the Gupta-Yos/CCS model and a fully catalytic boundary condition at the wall is considered.

---

[1] $q = K\sqrt{\frac{\rho}{R_n}}U^3$, where K is the heat transfer coefficient, taken as $1.7415{\times}10^{-4}$ for an Earth entry and R_n is the hemispherical nose radius.

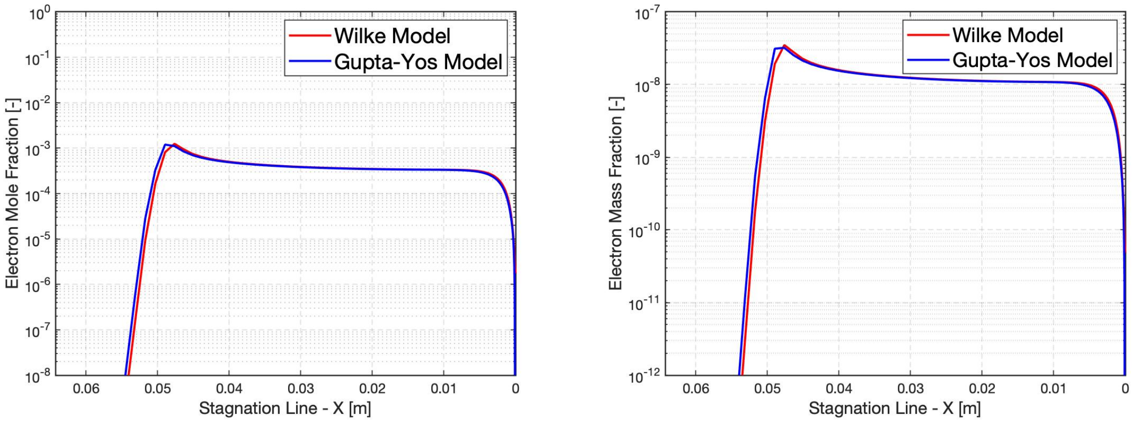

(a) Electron mole fraction

(b) Electron mass fraction

Figure 4.3: Electron mole and mass fractions along the stagnation line for the Wilke and Gupta-Yos transport models.

4.1.2 Stagnation Line Analysis

Figure 4.4 presents the results for the species mole fractions along the stagnation line, thus showing how x_i varies behind the shock front.

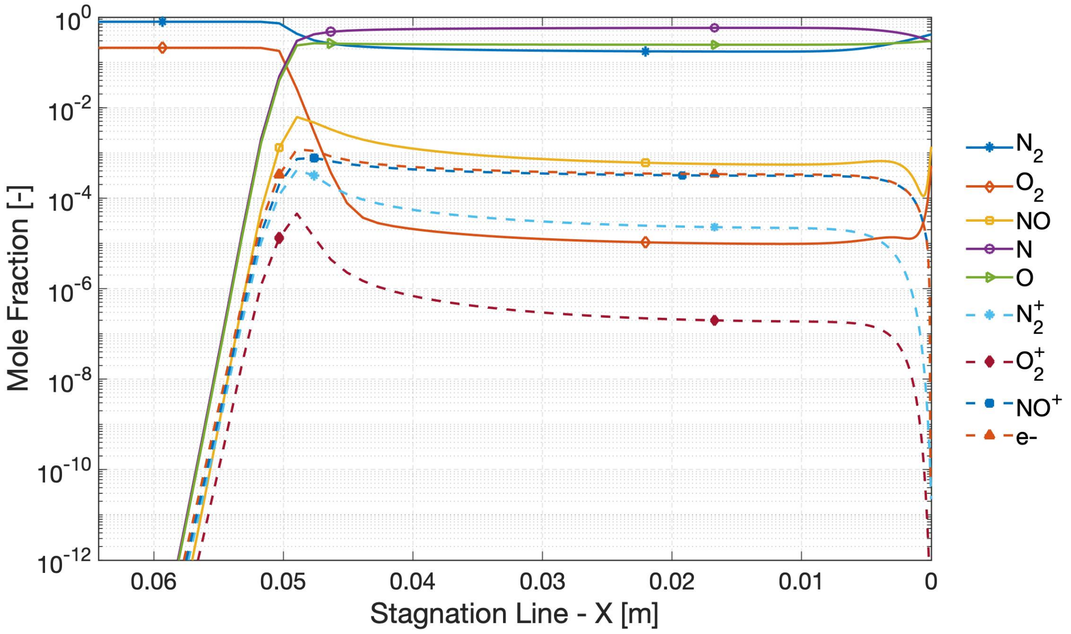

Figure 4.4: Species mole fractions along the stagnation line in thermal equilibrium.

As expected, the N_2 and O_2 mole fractions remain constant ($x_{\mathrm{N_2}}$ = 0.79 and $x_{\mathrm{O_2}}$ = 0.21), until the bow shock is reached. From this point on (X = 0.053 m), given the temperatures in excess of 9000K attained in the shock region, dissociation and ionisation of the molecules take place. N_2 and O_2 species mole fractions decrease and the rest of the species (atomic, ionic and electrons) mole fractions increase. The number of electrons increases rapidly downstream from the shock-wave and its mole fraction reaches a maximum value of 0.0012 and then diminishes quickly toward the vehicle surface. The chemical composition of the gas slightly stabilises before the boundary layer is reached, where, once again, temperature gradients promote chemical reactions of the species that constitute the gas. $x_{\mathrm{N_2}}$, $x_{\mathrm{O_2}}$ and x_{NO} rapidly increase at the surface, while $x_{\mathrm{N_2^+}}$, $x_{\mathrm{O_2^+}}$ and $x_{\mathrm{NO^+}}$ decrease, suggesting that the latter are recombining with e$^-$ to form the former species. The atomic nitrogen has the highest and nearly uniform mole fraction within the shock layer. Nonetheless, the nitrogen atoms recombine at the catalytic surface and yields a high mole fraction of 0.4135 for the molecular nitrogen.

4.1.3 Impact of Nose Geometry

Figure 4.5 shows the temperature and pressure profiles along the stagnation line, as well as the wall heat flux and pressure profiles for both geometries considered in this work.

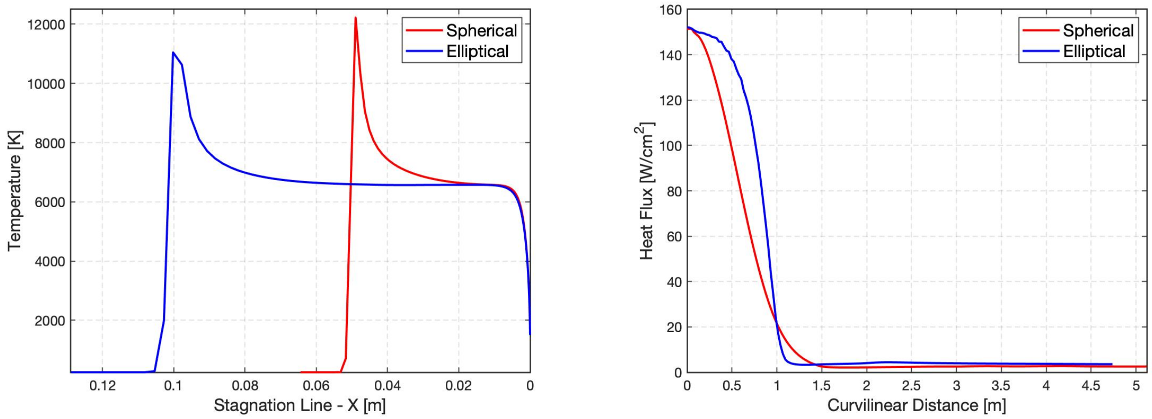

(a) Stagnation line temperature (b) Wall heat flux

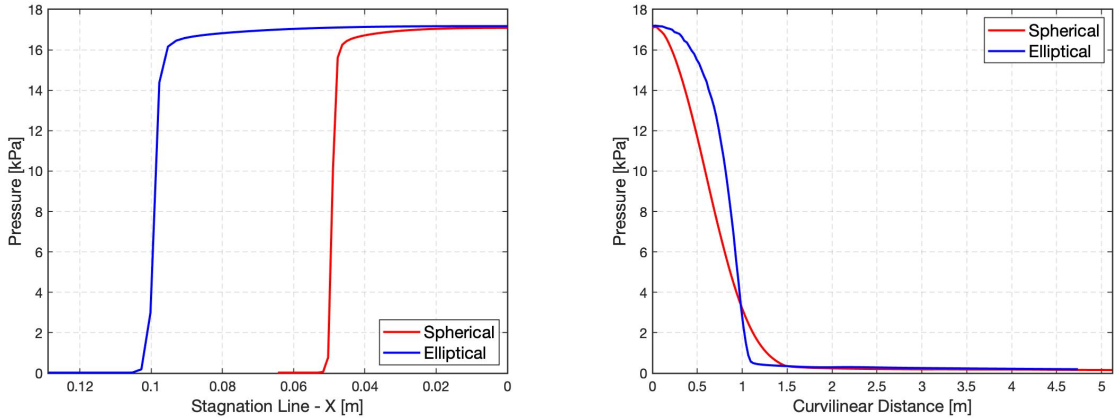

(c) Stagnation line pressure (d) Wall pressure distribution

Figure 4.5: Temperature, heat flux and pressure profiles for the two different nose geometries.

Figures 4.5 (a) and (c) illustrate that the shock layer is thicker for the elliptical nose geometry, with a wider shock front being 0.0513 m further away from the vehicle surface when compared to the spherical case. Although the latter shows a higher temperature peak, no significant conclusions can be withdrawn regarding the shock front due to the roughness of the area. The heat flux at the stagnation point differs less than 0.5% and the wall heat flux profile differs in shape with a plateau value of 2.6 and 3.6 W cm^{-2}

for the spherical and elliptical cases, respectively.

The two wall pressure curves also have different tendencies (Figure 4.5 (d)), as expected due to the different nose geometries. With respect to the pressure peak (at the stagnation point), this value is 0.3% higher in the elliptical case when compared to the spherical one.

4.2 Thermal Non-Equilibrium

Figure 4.6 presents the impact of considering Park's two-temperature model to account for thermal non-equilibrium on the temperature and pressure profiles along the stagnation line for the spherical nose geometry. For comparison purposes, the equilibrium results are reported in dashed lines.

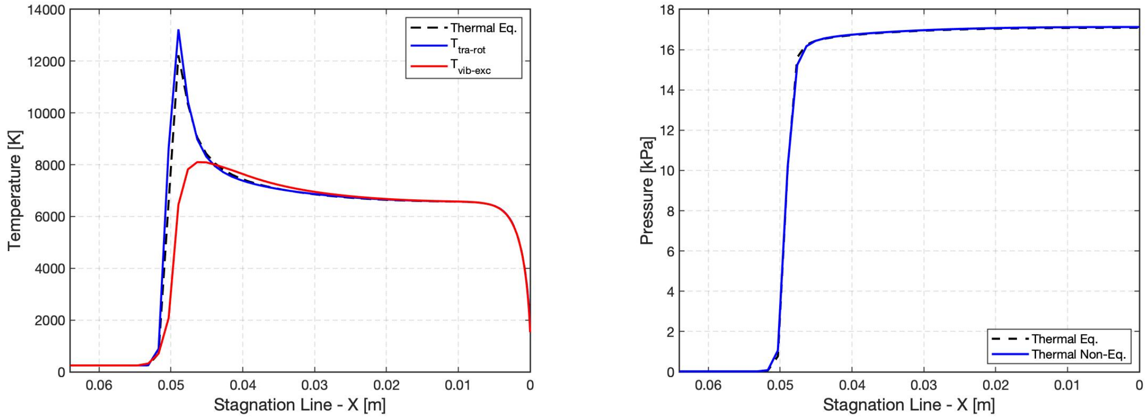

(a) Stagnation line temperature

(b) Stagnation line pressure

Figure 4.6: Temperature and pressure profiles along the stagnation line for both thermal equilibrium and non-equilibrium.

As can be seen in Figure 4.6 (a), the peak in translational-rotational temperature (blue line) is 8.2% higher for the non-equilibrium case when compared to the equilibrium case results, with the same overall trend as the equilibrium case. Moreover, the non-equilibrium case reveals a wider shock front and an increase in the shock standoff distance. The electron-vibrational-electronic temperature peak (red line) is 38.8% lower than that of the translational-rotational temperature and follows a very distinct profile up until X = 0.013 m. This leads to the conclusion that the flow is in a state of very strong non-equilibrium in the shock layer, reaching thermal equilibrium in the boundary layer region.

The pressure in thermal non-equilibrium is assumed to be the sum of the heavy species pressure and the free electrons' pressure, which are functions of the translational and the free electrons' temperature, respectively. Expectedly, since the pressure is not affected by the internal degrees of freedom of the particles, the pressure profile for both equilibrium and non-equilibrium conditions is the same within the shock layer, as illustrated in Figure 4.6 (b).

Figure 4.7 reveals that, apart from the wider shock front, the stagnation line flow composition does not change significantly with respect to the thermal equilibrium case.

Moreover, the heat flux results at the stagnation point showed a difference smaller than 10% between the two cases.

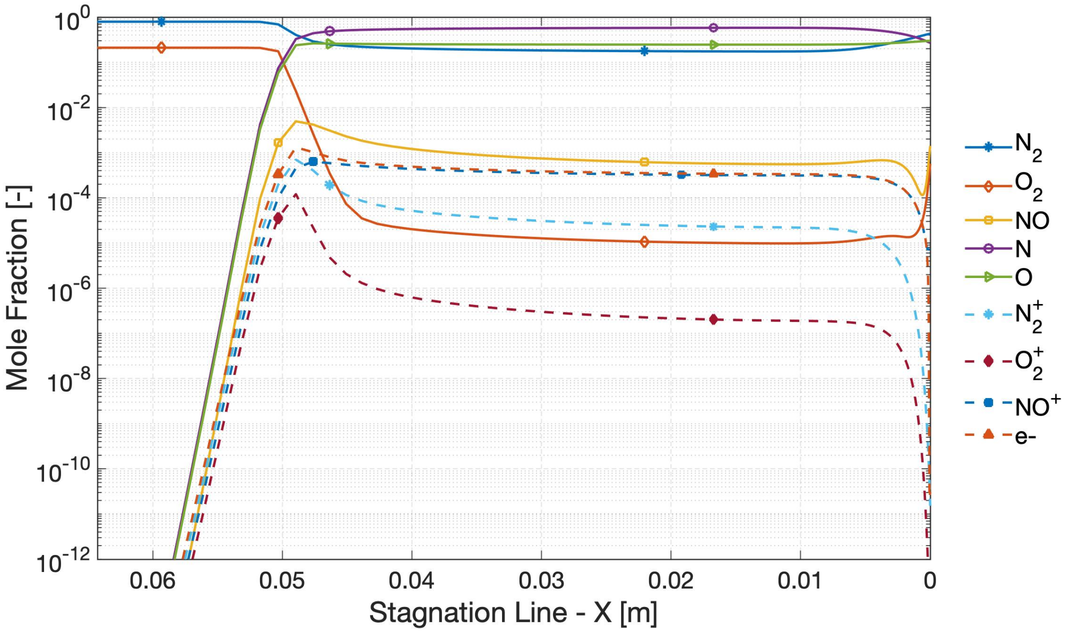

Figure 4.7: Species mole fractions along the stagnation line in thermal non-equilibrium.

The small differences encountered in this analysis allows to assume thermal equilibrium combined with chemical non-equilibrium in further simulations. This simplified method is proved to be more efficient, reducing, this way, the convergence time of the solution for the simulations with a flap angle different than zero.

4.3 Impact of Flap Deflection Angle

The test matrix used in order to evaluate the influence of the control surface is shown in Table 4.1.

Table 4.1: Test matrix used to evaluate the impact of flap deflection angle η at zero angle of attack.

Nose Geometry	Transport Model	ρ [kg m^{-3}]	U_∞ [km s^{-1}]	Flap Angle η [°]	A_{ref} [m^2]	c_{ref} [m]
Spherical	Gupta-Yos/CCS	3.096×10^{-4}	7.6	0 10 20 30	2.84	4.6
Elliptical	Gupta-Yos/CCS	3.096×10^{-4}	7.6	0 10 20 30	2.84	4.06

Spherical Geometry

Figure 4.8 shows how the temperature changes along the stagnation line and the wall heat flux for the different flap deflection angles considering the spherical nose geometry. As expected, the stagnation line profile only changes slightly, with stagnation point temperatures not varying when compared to the zero deflection angle case (black dashed line). Since the flow reaching the flap is supersonic behind the shock front, the deflection of a control surface does not affect the heat flux in the nose region.

Regarding the wall heat flux (Figure 4.8 (b)), for the η = 10° and η = 20° cases, the heat flux at the stagnation point is found to be slightly higher with respect to the baseline case ($\eta = 0°$). However, there is no reason to believe that the flap deflection angle has a direct or significant influence on the stagnation point heat flux, since the same trend is not observed in the η = 30° case. Naturally, the flap deflection introduces a new shock-wave within the flow at a curvilinear distance around 3.75 m, which increases the temperature behind it. Consequently, this leads to an increase in the heat flux and its magnitude increases as the flap deflection angle increases. The peak in heat flux for this region and for the η = 30° case is 558% higher than for the baseline case, while for the η = 10°, this scenario corresponds to a 62.7% increase in heat flux.

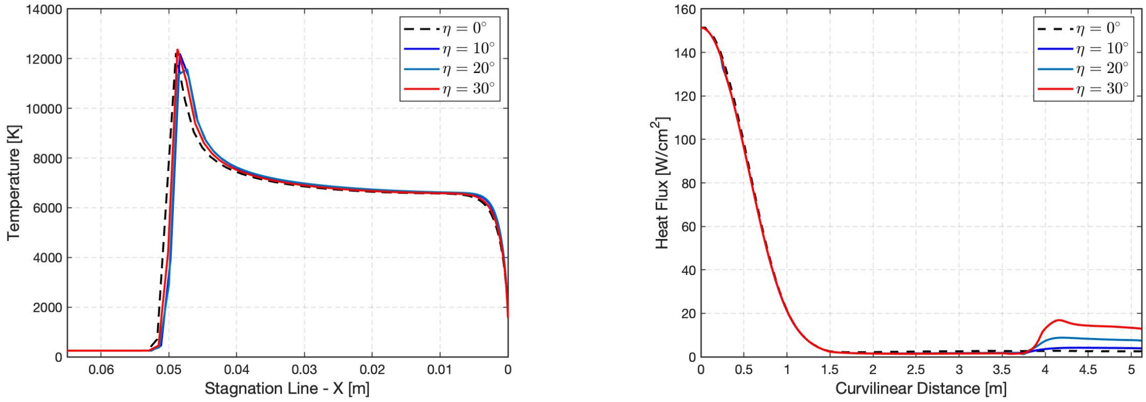

(a) Stagnation line temperature

(b) Wall heat flux

Figure 4.8: Temperature profile along the stagnation line and wall heat flux for different flap deflection angles.

The pressure distribution on the wall for the different deflection angles is also plotted in Figure 4.9.

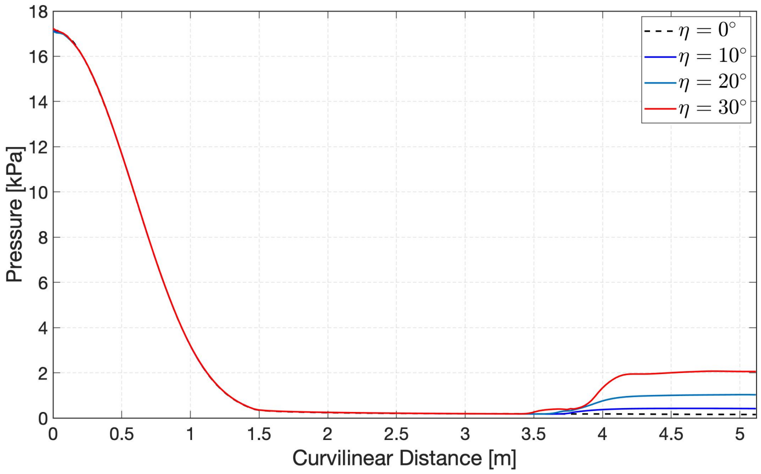

Figure 4.9: Wall pressure distribution for different flap deflection angles.

From the stagnation point on up until the flap region, the pressure profile remains the same for all the cases. As the flap is reached by the flow, a shock-wave is, once again, responsible for increasing the pressure behind it. These effects change the forces and moments acting on the vehicle. A slight disturbance of the pressure is observed around a curvilinear distance of 3.5 m for the η = 20° and η = 30° cases, with the latter having the most visible effect. As discussed in Chapter 1, these disturbances are caused by the subsonic portion of the boundary layer on the vehicle's surface approaching the flap which provides a path for the disturbances such as the increased pressure produced by the shock wave to influence the upstream flow. This adverse pressure gradient ultimately leads to flow separation. Figure 4.10 illustrates the velocity profile in the X direction for the three flap deflection cases, where negative values for the velocity can be clearly observed in the region near the control surface, supporting the premise of flow separation.

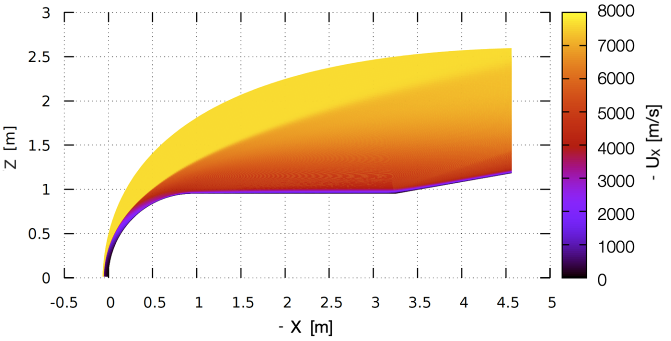

(a) Velocity profile, $\eta = 10°$

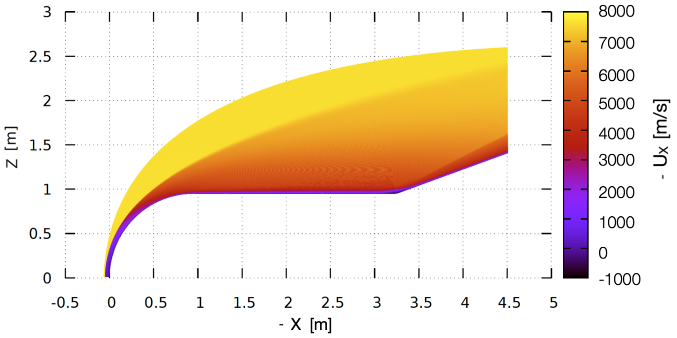

(b) Velocity profile, $\eta = 20°$

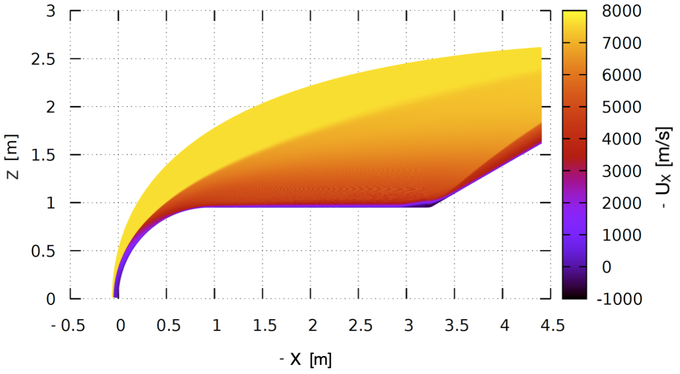

(c) Velocity profile, $\eta = 30°$

Figure 4.10: Velocity profile in the X direction for different flap deflection angles.

Figure 4.11 reports the molecular and atomic oxygen mass fraction in the flow field for the spherical geometry and $\eta = 30°$. O_2 concentration decreases within the shock layer (behind both shock waves), where dissociation takes place. In the region downstream of the stagnation point, where the temperature is lower, the decrease in O_2 mass fraction is smoother.

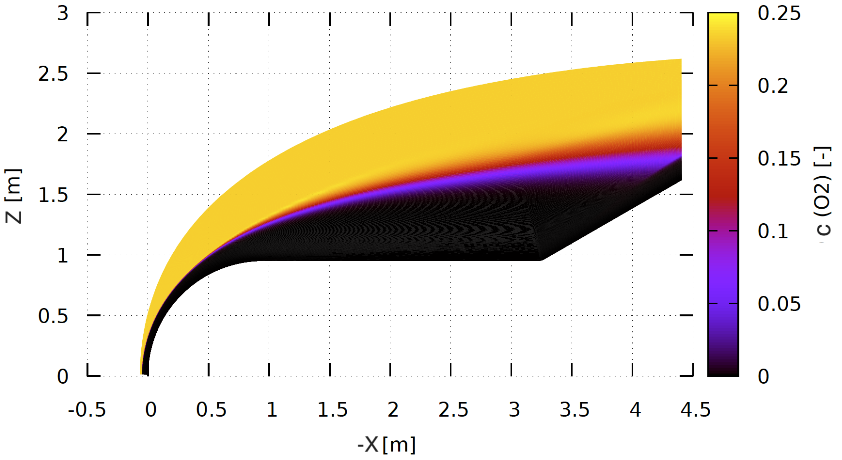

(a) O_2 mass fraction, $\eta = 30°$

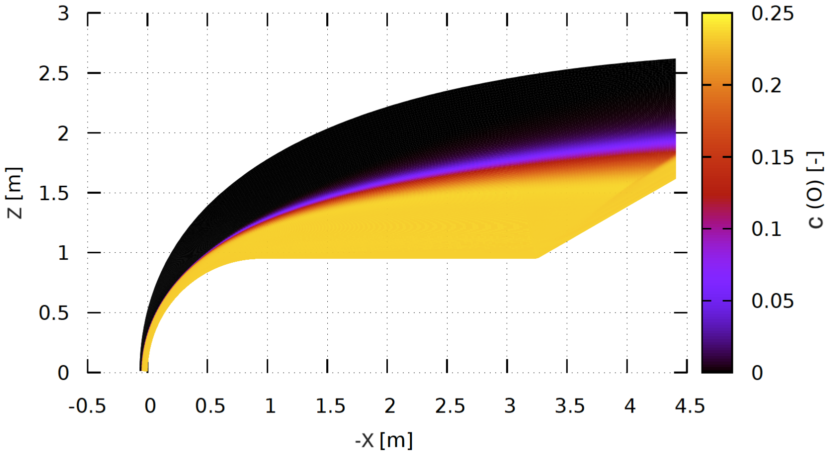

(b) O mass fraction, $\eta = 30°$

Figure 4.11: Molecular and atomic oxygen mass fractions for $\eta = 30°$.

Figure 4.12 depicts the molecular and atomic nitrogen mass fractions along the flow. N_2 concentration decreases within the shock layer and the dissociation reactions lead to an increase in c_{N}, only to decrease again near the vehicle surface where the catalytic wall promotes atom recombination.

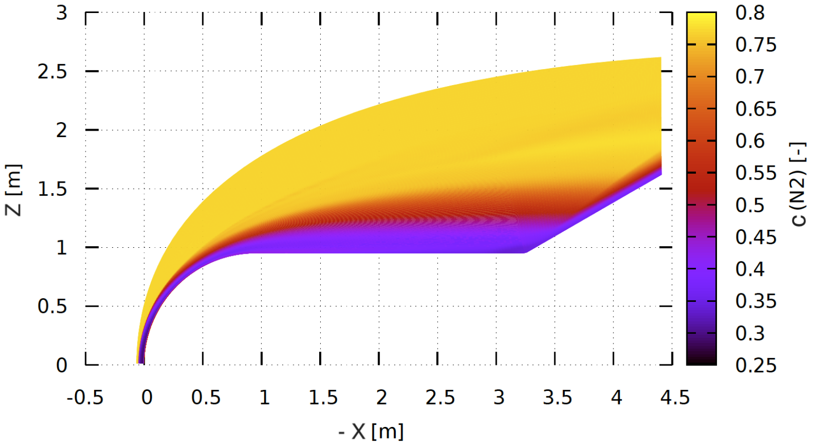

(a) N_2 mass fraction, $\eta = 30°$

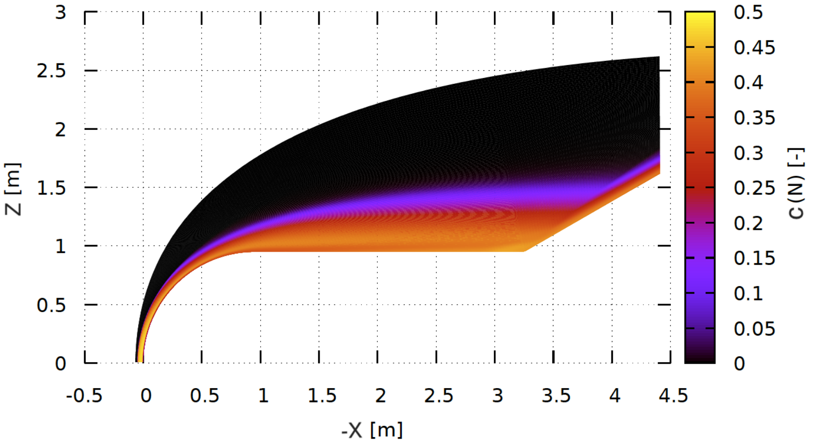

(b) N mass fraction, $\eta = 30°$

Figure 4.12: Molecular and atomic nitrogen mass fractions for $\eta = 30°$.

Elliptical Geometry

Figure 4.13 reveals the temperature profile along the stagnation line and the wall heat flux for the different flap deflection angles considering the elliptical nose geometry. Once again, the stagnation line profile does not show significant changes, with stagnation point temperatures not varying more than 8% when compared to the zero deflection angle case (black dashed line). However, slight differences are observed between the profiles of the $0 - 10^{\circ}$ and $20 - 30^{\circ}$ pairs. The reason for this may lay in the fact that the meshes used for the positive deflections cases were slightly stretched in the normal direction in order to accommodate some changes that the flaps could introduce in the flow. Nonetheless, the stagnation line profile and shock region remained within the limits of the baseline case. Given the high convergence time of the solution (between one and two months), the cases that could be tested were limited and no better solution was found.

The wall heat flux shown in Figure 4.13 (b) is similar for all the cases with a flap deflection angle different than zero. This reinforces the idea that there is no need to restart the simulations with higher quality meshes, even though the temperature profile is not as similar as it should. The heat flux peak in the flap region for the η = 30° case is 409.2% higher than for the baseline case, while for the η = 10°,

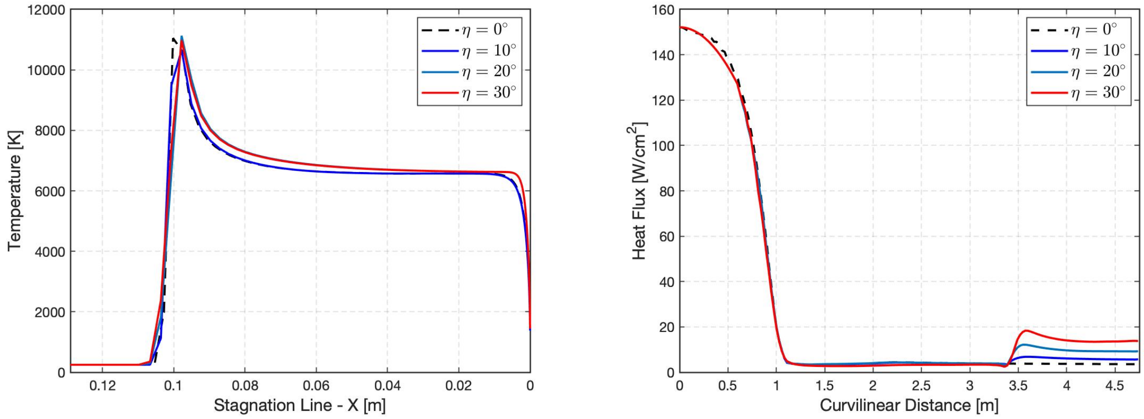

(a) Stagnation line temperature

(b) Wall heat flux

Figure 4.13: Temperature profile along the stagnation line and wall heat flux for different flap deflection angles.

this scenario corresponds to a 19.2% increase in heat flux.

The pressure profile is represented in Figure 4.14 and it shows the same overall trend up until the flap region for all the cases (the same behaviour had already been encountered in the spherical geometry case). In the flap region, the shock wave formed by the flap increases the pressure behind it, with the higher pressure achieved, naturally, by the highest deflection angle (η = 30°). Moreover, the slight disturbance of the pressure is again clearly observed around a curvilinear distance of 3.25 m for the η = 30° case, which is caused by the subsonic portion of the boundary layer on the vehicle's surface approaching the compression flap.

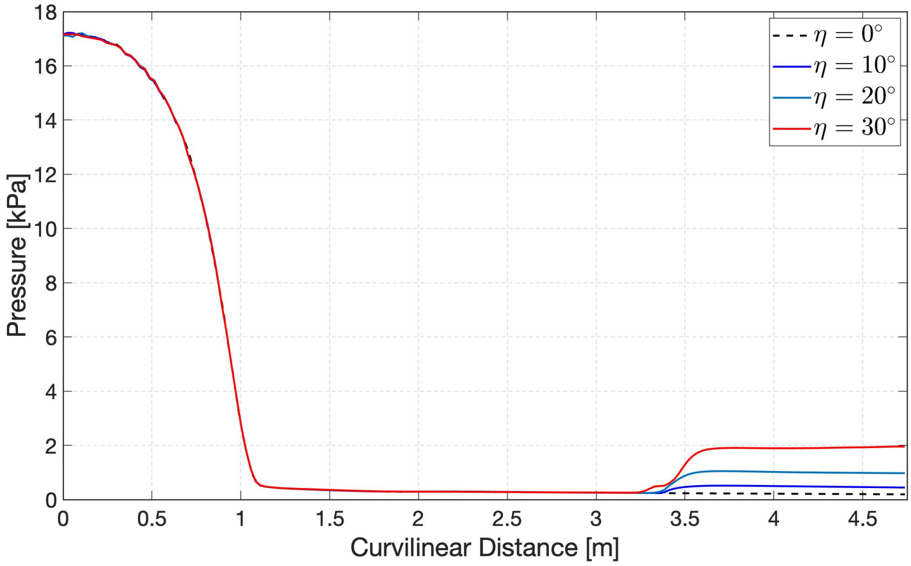

Figure 4.14: Wall pressure distribution for different flap deflection angles.

4.3.1 Aerodynamic Coefficients

Once the CFD solution has converged, post processing is required in order to achieve the objectives of this study. Two algorithms were generated in order to compute the forces and moments acting on the reentry vehicle. The first one considers the normal (pressure) forces and it was validated considering some cases to which the results were already known (e.g. with a uniform pressure distribution, the sum of these forces must be zero). In flows at speeds greater than the speed of sound, a perturbation is only felt in the Mach cone (Mach angle given as $\arcsin\left(\mathrm{M}^{-1}\right)$) downstream from the source of disturbance and therefore, certain parts of the flap behave as though they were in the two-dimensional flow. Taken this into account, a correction factor was introduced in the pressure distribution along the flap in order to include the three-dimensional flow effects on the control surface [85, 86]. This correction factor is represented in Figure 4.15 (not to scale) and it is only used as a first approach to the problem since it does not take into account the effects of high temperature gas dynamics.

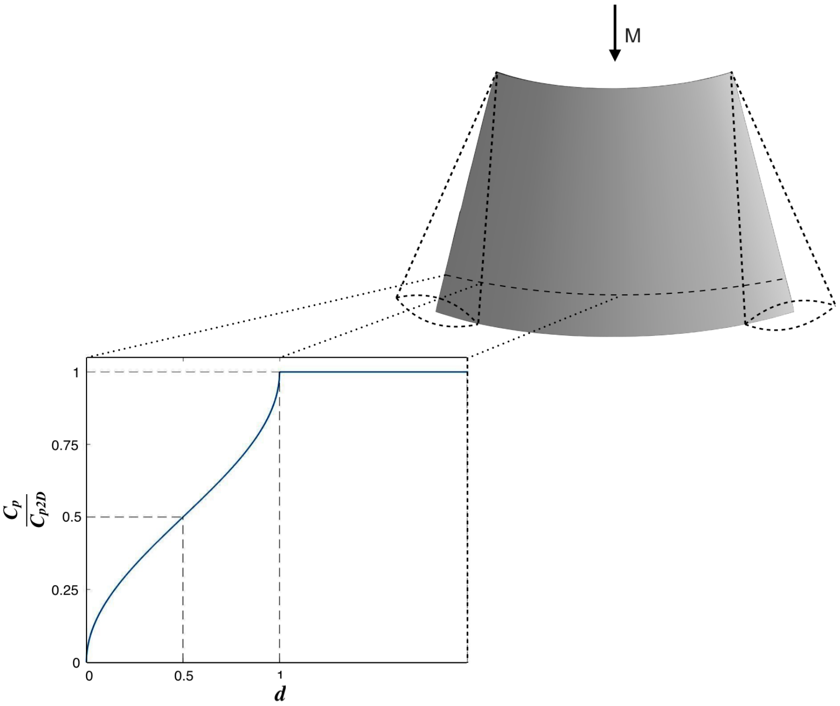

Figure 4.15: Pressure profile along the flap taken into account 3D effects (not to scale).

The pressure correction in the mach cone region is given by

$$\Delta p = \Delta p_{2D} \frac{2}{\pi} \arcsin \sqrt{d}. \tag{4.1}$$

The pressure profile remains the same as in the results from the simulations up until the disturbed region, which is under the influence of the side edges, is reached. d is a dimensionless number that quantifies the distance along the perturbed region of the trailing edge of the flap. Although not explicitly represented in Figure 4.15, the pressure profile is symmetric (as well as t).

The second algorithm takes into account the tangential (shear) forces.

The forces and aerodynamic coefficients were calculated as described in Chapter 2. Several different areas can be chosen when developing the reference area used in the drag and lift equations. If drag is perceived as being caused by friction between the air and the body, a logical choice would be the total surface area of the body. If drag is thought to be a resistance to the flow, a more logical choice would be the frontal area of the body which is perpendicular to the flow direction. Each of the areas are proportional to the other areas. Since the drag and lift coefficients are determined experimentally or computationally, by measuring the drag and lift and performing the necessary math to produce the coefficient, this choice is free. Different surface areas produce different force coefficients, but the drag and lift are the same, and the coefficients are related by the ratio of the areas. Therefore, the reference area chosen was the frontal/projected area, which is the same for both geometries.

In order to evaluate the aerodynamic characteristics of the stage, four different flap configurations were studied and the test matrix of Table 4.1 was applied to each one of them. For all the configurations, the origin of the frame of reference is set at the nose tip of the vehicle and the axes are defined as in the air-path/aerodynamic coordinate system.

180° Flap Configuration Centred at Y$_A$ = 0 m and Z$_A$ = 0.95 m

Figure 4.16 shows the 180° flap concept centred at Y$_A$ = 0 m and Z$_A$ = 0.95 m.

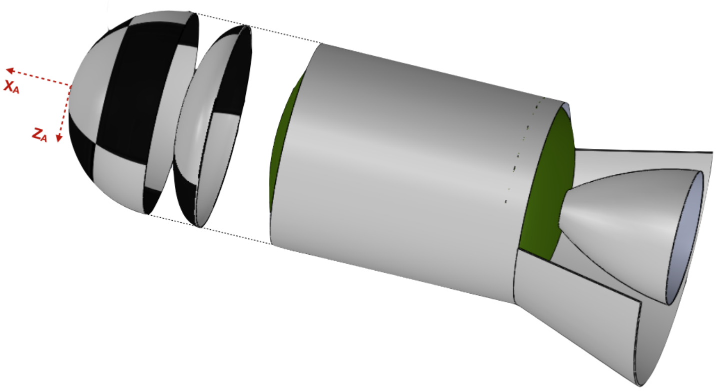

Figure 4.16: Rocket's stage equipped with a 180° flap centred at Y$_A$ = 0 m and Z$_A$ = 0.95 m.

The results obtained for the drag, lift and moment coefficients are represented in Figures 4.17 and 4.18. Apart from the drag coefficient, the resulting forces and moments for both nose geometries and both equilibrium and non-equilibrium (2T in dashed line) are very similar. The maximum discrepancy is found with a flap deflection angle of $\eta = 30°$ in the moment coefficient about mid-chord and corresponds to a 3.14% negative increase in C_{MY_A} for the spherical geometry when compared to the elliptical one.

Geometrical reasons dictate that under the same conditions, the elliptical geometry presents a higher drag coefficient, as depicted in Figure 4.17 (a). With respect to the spherical geometry, the highly elliptical nose shows a drag coefficient up to 52% higher ($\eta = 0°$ case). Between the equilibrium and non-equilibrium case for the spherical geometry, the differences are not higher than 3% for any deflection angle.

The maximum aerodynamic efficiency (L/D) is 0.19 obtained when the flap is deflected with an angle of $30°$ for the spherical geometry.

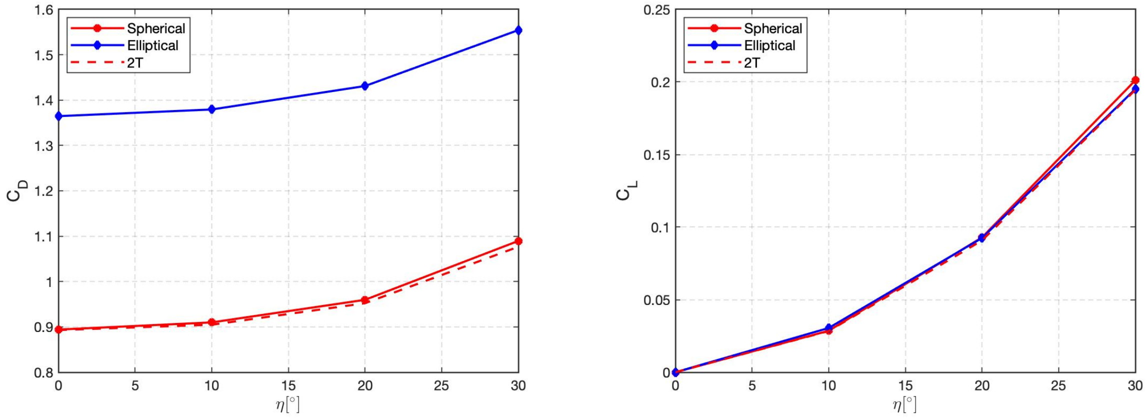

(a) Drag coefficient

(b) Lift coefficient

Figure 4.17: Drag and lift coefficients as function of the flap deflection angle for the vehicle with a 180° flap centred at Y$_A$ = 0 m and Z$_A$ = 0.95 m.

Naturally, since the flap is symmetric with respect to the plane defined by Y$_A$ = 0 and centred at Z = 0.95 m, the only moment about $\{$X$_A$, Y$_A$, Z$_A\}$ = $\{$0, 0, 0$\}$ and $\{$X$_A$, Y$_A$, Z$_A\}$ = $\{$-0.5c_{ref}, 0, 0$\}$ is the moment with respect to the Y$_A$ axis.

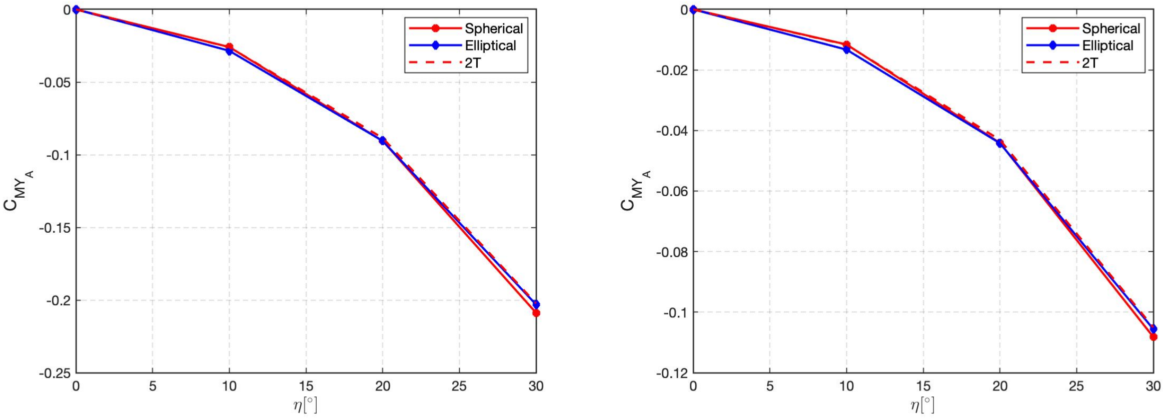

(a) Pitching moment coefficient about $\{$X$_A$, Y$_A$, Z$_A\}$ = $\{$0, 0, 0$\}$ m

(b) Pitching moment coefficient about $\{$X$_A$, Y$_A$, Z$_A\}$ = $\{$-0.5c_{ref}, 0, 0$\}$ m

Figure 4.18: Pitching moment coefficients as function of the flap deflection angle for the vehicle with a 180° flap centred at Y$_A$ = 0 m and Z$_A$ = 0.95 m.

90° Flap Configuration Centred at Y$_A$ = 0 m and Z$_A$ = 0.95 m

Figure 4.19 shows the 90° flap concept centred at Y$_A$ = 0 m and Z$_A$ = 0.95 m. This new symmetric flap configuration presents different results for all the coefficients, except for the $\eta = 0°$ case. The maximum drag and lift coefficients in equilibrium conditions represented in Figure 4.20 are 6.5% and 34.5% lower, respectively, when compared to the $180°$ flap configuration. The maximum aerodynamic efficiency is 0.13, 31% lower than for the first case that was analysed.

Once again, the moment coefficients with respect to the Y$_A$ axis increase in absolute value as the flap

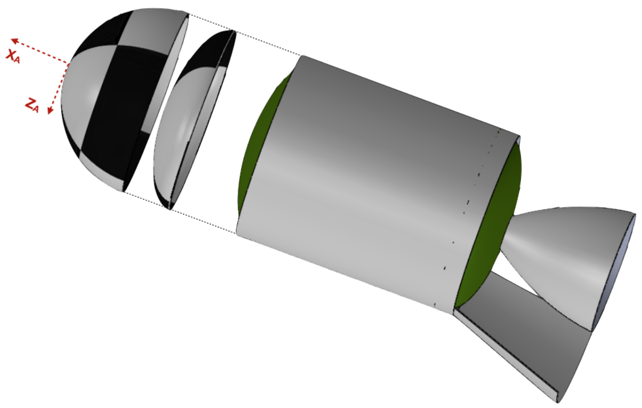

Figure 4.19: Rocket's stage equipped with a 90° flap centred at $Y_A = 0$ m and $Z_A = 0.95$ m.

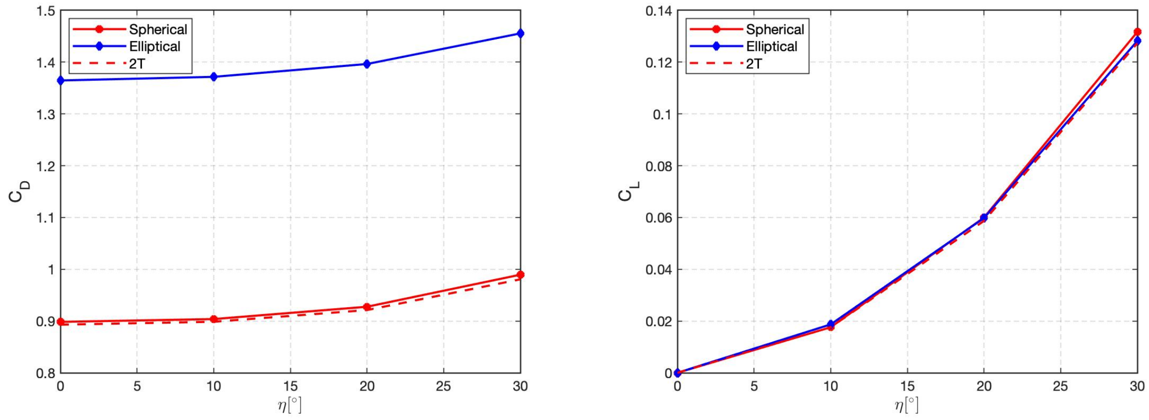

(a) Drag coefficient

(b) Lift coefficient

Figure 4.20: Drag and lift coefficients as function of the flap deflection angle for the vehicle with a 90° flap centred at $Y_A = 0$ m and $Z_A = 0.95$ m.

deflection angle increases (Figure 4.21), reaching a maximum of around 0.13 and 0.07 for the reference point at the origin and mid-chord, respectively.

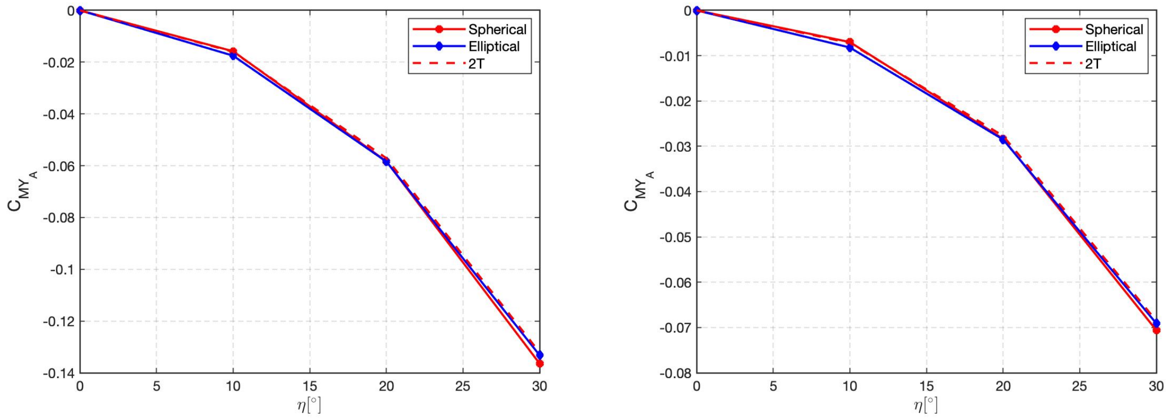

(a) Pitching moment coefficient about $\{X_A, Y_A, Z_A\} = \{0, 0, 0\}$ m

(b) Pitching moment coefficient about $\{X_A, Y_A, Z_A\} = \{-0.5c_{ref}, 0, 0\}$ m

Figure 4.21: Pitching moment coefficients as function of the flap deflection angle for the vehicle with a 90° flap centred at $Y_A = 0$ m and $Z_A = 0.95$ m.

90° Flap Configuration Centred at Y_A = 0.67 m and Z_A = 0.67 m

Figure 4.23 shows the 90° flap concept centred at Y_A = 0.67 m and Z_A = 0.67 m. This flap is not symmetric with respect to the plane defined by Y_A = 0 and thus additional moments are created by the aerodynamic forces (Figures 4.24 and 4.25).

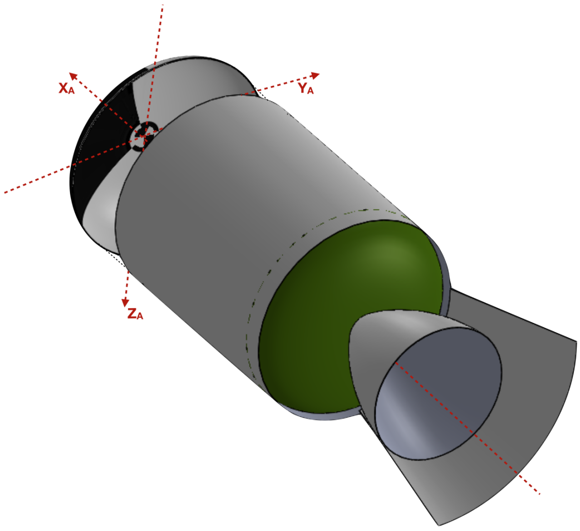

Figure 4.22: Rocket's stage equipped with a 90° flap centred at Y_A = 0.67 m and Z_A = 0.67 m.

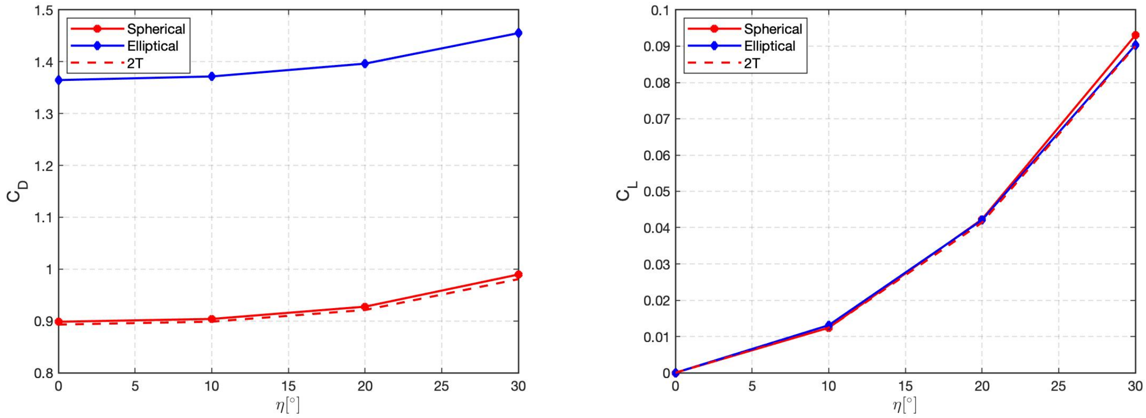

(a) Drag coefficient

(b) Lift coefficient

Figure 4.23: Drag and lift coefficients as function of the flap deflection angle for the vehicle with a 90° flap centred at Y_A = 0.67 m and Z_A = 0.67 m.

According to the results of Figure 4.23, the aerodynamic efficiency is not higher than 0.094 for the deflection angles considered. However, the additional moment coefficient with respect to the Z_A axis has a value of 0.1 (about $\{X_A, Y_A, Z_A\} = \{0, 0, 0\}$ m) for the maximum flap deflection angle considered and the absolute values of the moments with respect to the Y_A and Z_A axes are the same due to the flap geometry.

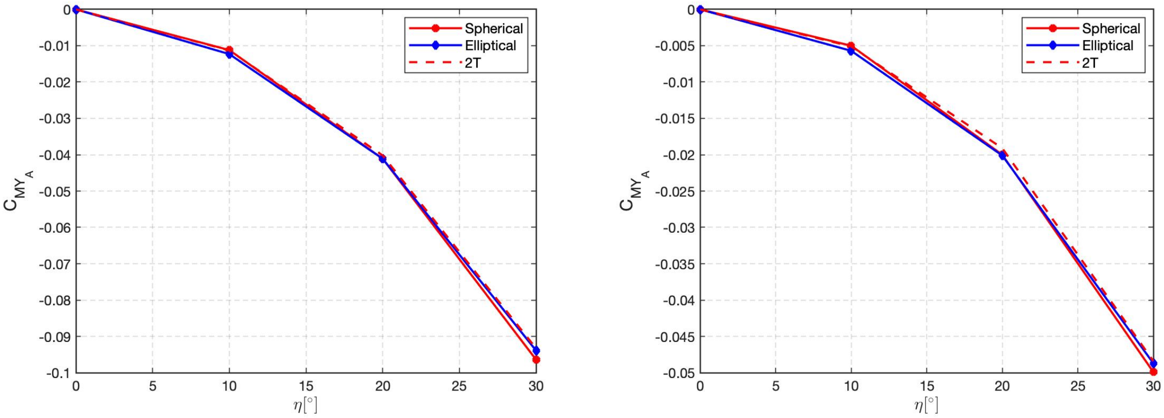

(a) Pitching moment coefficient about {X$_A$, Y$_A$, Z$_A$} = {0, 0, 0} m

(b) Pitching moment coefficient about {X$_A$, Y$_A$, Z$_A$} = {-0.5c_{ref}, 0, 0} m

Figure 4.24: Pitching moment coefficients as function of the flap deflection angle for the vehicle with a 90° flap centred at Y$_A$ = 0.67 m and Z$_A$ = 0.67 m.

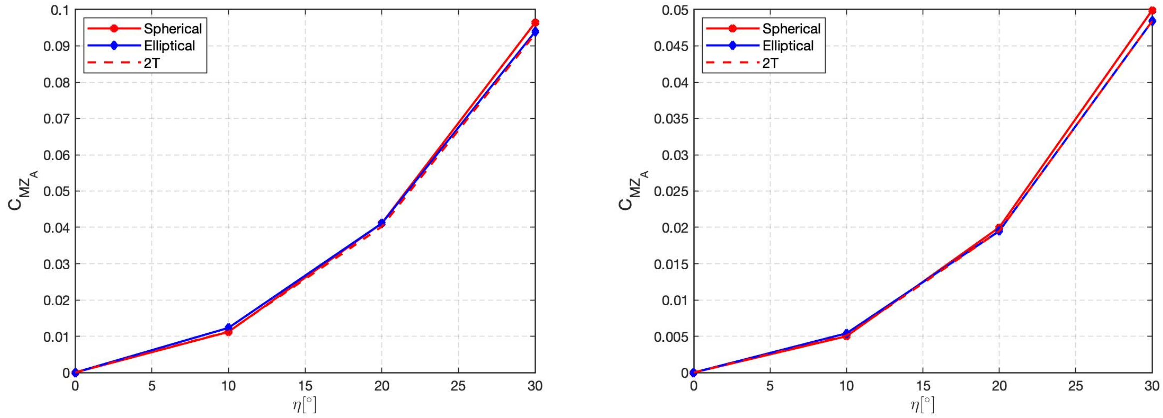

(a) Yawing moment coefficient about {X$_A$, Y$_A$, Z$_A$} = {0, 0, 0} m

(b) Yawing moment coefficient about {X$_A$, Y$_A$, Z$_A$} = {-0.5c_{ref}, 0, 0} m

Figure 4.25: Yawing moment coefficients as function of the flap deflection angle for the vehicle with a 90° flap centred at Y$_A$ = 0.67 m and Z$_A$ = 0.67 m.

45° Flap Configuration Centred at Y$_A$ = 0.36 m and Z$_A$ = 0.88 m

Figure 4.26 shows the 45° flap concept centred at Y$_A$ = 0.36 m and Z$_A$ = 0.88 m. This flap is also not symmetric with respect to the plane defined by Y$_A$ = 0 and the moment coefficients created by the aerodynamic forces are represented in Figures 4.28 and 4.29.

This configuration leads to the lowest aerodynamic efficiency of all the flap configurations studied when the maximum deflection angle is considered, with a value of 0.062, for the spherical case. Figure 4.27 also shows that C_D does not increase beyond 0.94 and 1.41 for the spherical and elliptical geometries, respectively, as opposed to the other cases.

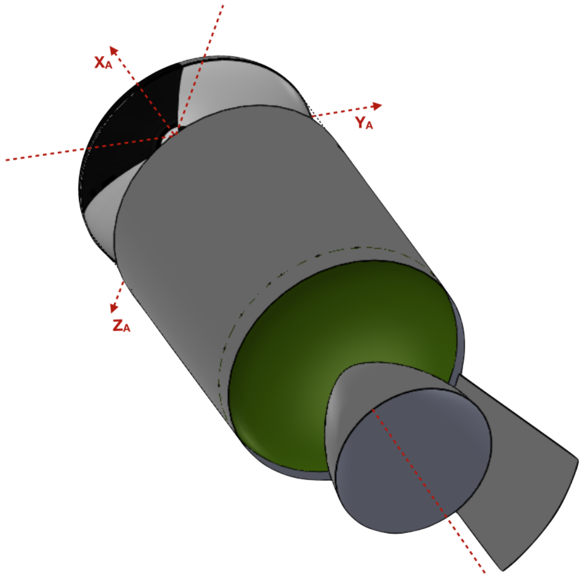

Figure 4.26: Rocket's stage equipped with a 45° flap centred at Y_A = 0.36 m and Z_A = 0.88 m

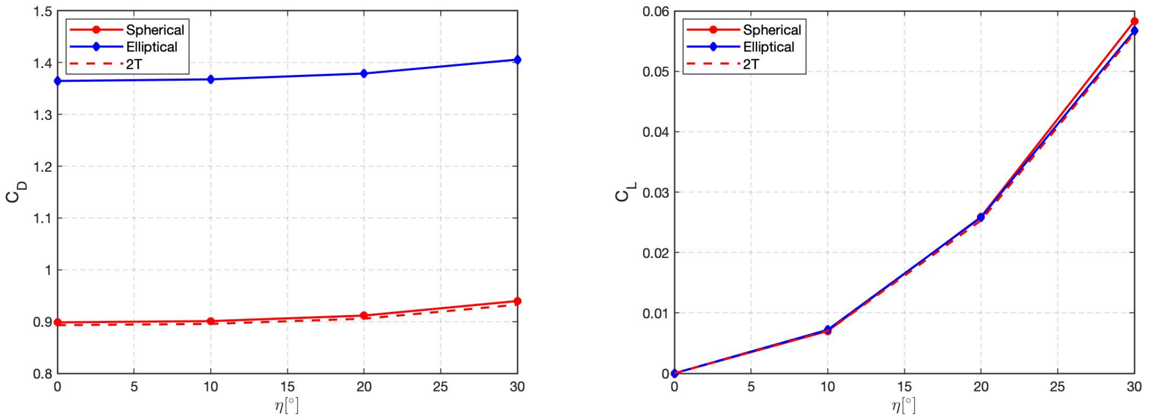

(a) Drag coefficient

(b) Lift coefficient

Figure 4.27: Drag and lift coefficients as function of the flap deflection angle for the vehicle with a 45° flap centred at Y_A = 0.36 m and Z_A = 0.88 m.

The results support, once again, the hypothesis of thermal equilibrium with discrepancies not higher than 0.7% for the drag coefficient and 3.5% for the lift and moment coefficients between the 1T and 2T conditions.

Although this configuration represents only half the mass of the previous one, it also represents a decrease in efficiency in terms of moments and forces.

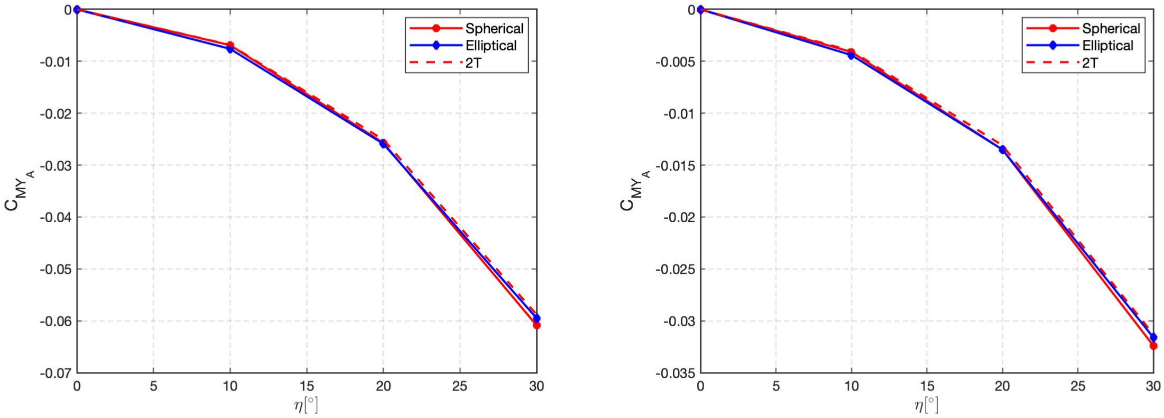

(a) Pitching moment coefficient about {X$_A$, Y$_A$, Z$_A$} = {0, 0, 0} m (b) Pitching moment coefficient about {X$_A$, Y$_A$, Z$_A$} = {-0.5c_{ref}, 0, 0} m

Figure 4.28: Pitching moment coefficients as function of the flap deflection angle for the vehicle with a 45° flap centred at Y$_A$ = 0.36 m and Z$_A$ = 0.88 m.

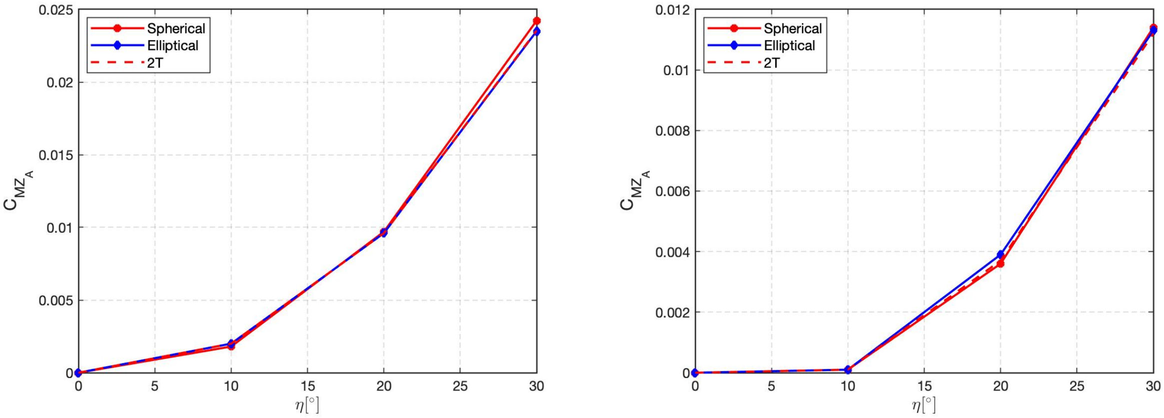

(a) Yawing moment coefficient about {X$_A$, Y$_A$, Z$_A$} = {0, 0, 0} m (b) Yawing moment coefficient about {X$_A$, Y$_A$, Z$_A$} = {-0.5c_{ref}, 0, 0} m

Figure 4.29: Yawing moment coefficients as function of the flap deflection angle for the vehicle with a 45° flap centred at Y$_A$ = 0.36 m and Z$_A$ = 0.88 m.

These results are only valid when the cylindrical protection system for the nozzle depicted in Figure 1.7 is deployed. Naturally, if this part is removed from the reentry vehicle, the moments and the lift coefficients increase. This increase is, in percentage, always higher for the $\eta = 10^\circ$ case, which is expected, since it is the case in which the pressure profile is more similar to the one with $\eta = 0^\circ$. Furthermore, in this scenario, the maximum aerodynamic efficiency obtained for the deflection angles that were tested is 0.2. The aerodynamic coefficients obtained for the case without a cylindrical protection system attached to the rear part of the vehicle are shown in Appendix B.

Although only four different flap configurations have been presented, the options are endless. Moreover, since the results for three different configuration angles are known, if these are kept equal (45°, 90° or 180°) and the flap location is shifted, the new forces and moments acting on the vehicle can be simply obtained by multiplying the presented results by the corresponding rotation matrix.

Chapter 5

Conclusions

This chapter concludes this thesis by presenting its major achievements and recommended steps for future work.

5.1 Achievements

The influence of the transport model, nose geometry, multi-temperature model and flap angle and configuration was successfully assessed for the reentry of a rocket's upper stage equipped with control surfaces. This was mainly achieved by performing CFD simulations with the hypersonic code SPARK, developed and maintained at IPFN. The practical nature of the work did not spare the development of a post-processing algorithm capable of computing the aerodynamic forces and moments acting on the reentry vehicle, with the wall pressure distribution and stress tensor profiles as inputs for the code.

The analysis of the transport model concluded that the Wilke model estimates the peak temperature to be 1.4% higher when compared to the Gupta-Yos model and the lowest temperature achieved behind the shock was 1.5% higher in the Wilke case. Consequently, the heat flux in the nose region is 5.1% lower for the Gupta-Yos model with respect to the Wilke case. In terms of the pressure profile, no significant differences were found. For these reasons and on the account that the Gupta-Yos/CCS model considers the true nature of the particle collisions, all the simulations with a positive flap angle used this transport model.

The main differences found between the two nose geometries were the thickness of the shock layer (the elliptical case increased the shock stand-off distance in 0.0513 m) and the heat flux and pressure profiles of the nose exclusively.

The comparison between the two temperature models (equilibrium and Park's two temperature model) revealed a strong non-equilibrium in the shock-wave region, a wider shock front and a slight increase in the shock standoff distance. The electron-vibrational temperature peak is 38.8% lower than that of the translational-rotational temperature. Nonetheless, thermal equilibrium was reached in the region of interest (boundary layer), which allowed to use the more time-efficient 1T temperature in further simulations. Within the shock layer, the pressure profiles for both equilibrium and non-equilibrium conditions were found to be the same, as expected, since the pressure is not affected by the internal degrees of freedom of the particles.

The pressure and heat flux profiles were successfully obtained for the different flap deflection angles, which, respectively, allowed to generate the necessary inputs for the algorithm afore mentioned and, in the future, will allow to better predict the type of protection system needed. Furthermore, the subsonic portion of the boundary layer on the vehicle's surface approaching the flap was found to provide a path for the increased pressure produced by the shock wave to influence the upstream flow in the $\eta = 20°$ and $30°$, which led to flow separation in this region.

At last, the aerodynamic coefficients were obtained for four different flap configurations and three positive deflection angles. The maximum aerodynamic efficiency was found for the circular geometry (L/D = 0.19). Additional 2T temperature simulations were performed with the control surfaces deflected in order to prove that this assumption does not significantly alter the results.

5.2 Future Work

The future steps recommended for this work are:

- CFD simulations in further points of the trajectory of the rocket's stage with the estimated aerodynamic coefficients as inputs for the trajectory code.
- True multidimensional analysis, including gaps and other interfaces.
- Turbulence analysis in the region away from the stagnation point.
- CFD simulations in the wake region to assess how this area influences the forces acting on the reentry vehicle.
- Assessment of the radiative heat fluxes, dependent on the population of the excited states and convection of the fundamental states which, together with the convective heating computed in this work can estimate the **total** heat flux experienced by the selected body geometry.
- Thermal protection system design, including the selection of the effective and lightweight materials able to withstand the heating loads generated during the trajectory.
- Assessment of the recovery system's potential impact on the launcher's lifting capability, an important factor that might complicate landing and reusing rocket upper stages.

Bibliography

[1] R. D. Launius. *The Smithsonian History of Space Exploration: From the Ancient World to the Extraterrestrial Future*. Smithsonian Books, 2018.

[2] NASA Jet Propulsion Laboratory. Mission to Wild-2, stardust. Retrieved April 1, 2019, from `https://www.jpl.nasa.gov/missions/stardust/`.

[3] Japan Aerospace Exploration Agency. Hayabusa's Scientific and Engineering Achievements during Proximity Operations around Itokawa. Retrieved April 1, 2019, from `http://www.isas.jaxa.jp/e/snews/2005/1102.shtml`.

[4] European Space Agency. Rosetta Overview. Retrieved April 1, 2019, from `http://www.esa.int/Our_Activities/Space_Science/Rosetta_overview`, .

[5] G. Bignami and A. Sommariva. *The Future of Human Space Exploration*. Palgrave Macmillan UK, 1st edition, 2016. ISBN 978-1-137-52657-1,978-1-137-52658-8.

[6] F. J. Regan and S. M. Anandakrishnan. *Dynamics of Atmospheric Re-Entry*. AIAA, 1993.

[7] A. Korzun, K. J. Murphy, and K. Edquist. Supersonic aerodynamic characteristics of blunt body trim tab configurations. In *31st AIAA Applied Aerodynamics Conference*. AIAA 2013-2809, June 2013. doi: 10.2514/6.2013-2809.

[8] C. C. Coleman and F. Faruqi. On stability and control of hypersonic vehicles. Defence Science and Technology Organisation, Australia, Weapons System Division, November 2009.

[9] European Space Agency. Reentry Technologies. Retrieved May 20, 2019, from `https://www.esa.int/Our_Activities/Space_Transportation/IXV/Reentry_technologies`, .

[10] J. J. Bertin. *Hypersonic Aerothermodynamics*. AIAA, 1994.

[11] D. F. Potter. *Modelling of Radiating Shock Layers for Atmospheric Entry at Earth and Mars.* PhD thesis, The University of Queensland, Australia, 2011.

[12] D. D. Loureiro. High-temperature modeling of transport properties in hypersonic flows. Master's thesis, Instituto Superior Técnico, Lisboa, 2015.

[13] J. D. Anderson. *Hypersonic and High Temperature Gas Dynamics.* AIAA, 1989.

[14] F. Grasso, G. Ranuzzi, S. Cuttica, M. M. Marini, and B. Chanetz. Shock-wave/turbulent boundary-layer interactions in nonequilibrium flows. *AIAA Journal*, 39:2131–2140, January 2001. doi: 10.2514/3.14977.

[15] J. Kelleher. The tiny Electron rocket is getting ready to fly again (Personal blog post). Retrieved July 1, 2019, from `https://www.medium.com/@JackKelleher/the-tiny-electron-rocket-is-getting-ready-to-fly-again-fb81846a765e`.

[16] SpaceX. Reusability. Retrieved August 19, 2019, from `https://www.spacex.com/reusability-key-making-human-life-multi-planetary`.

[17] Blue Origin. New Shepard. Retrieved August 19, 2019, from `https://www.blueorigin.com/new-shepard/`.

[18] Rocket Lab. Rocket Lab Announces Reusability Plans for Electron Rocket. Retrieved August 19, 2019, from `https://www.rocketlabusa.com/news/updates/rocket-lab-announces-reusability-plans-for-electron-rocket/`.

[19] Global Small Launch Vehicle Market - Analysis and Forecast 2018-2028 - Focus on Payload Ranges and End Users. Technical report, Research and Markets, November 2018.

[20] *Vega User's Manual*. Arianespace Service & Solutions, April 2014. Issue 4, Revision 0.

[21] NASA Official: W. Graham. Vega launches Italy's PRISMA Earth observation satellite. Retrieved July 1, 2019, from `https://www.nasaspaceflight.com/2019/03/vega-italys-prisma-earth-observation-satellite/`.

[22] S. Bianchi. The Launchers and the Vega Programme and the Launcher Subsystems. Directorate of Launchers, ESA, February 2005.

[23] D. Akin. Applications of ultra-low ballistic coefficient entry vehicles to existing and future space missions. In *SpaceOps 2010 Conference*. AIAA 2010-1928, April 2010.

[24] S. Dutta, B. Smith, D. Prabhu, and E. Venkatapathy. Mission sizing and trade studies for low ballistic coefficient Entry systems to venus. In *IEEE Aerospace Conference Proceedings*, March 2012. doi: 10.1109/AERO.2012.6187002.

[25] H. K. Magazu, D. L. Akin, and M. J. Lewis. Aerothermodynamics of a parashield re-entry vehicle. *Journal of Spacecraft and Rockets*, 35:434–441, July 1998. doi: 10.2514/2.3373.

[26] R. Savino and V. Carandente. Aerothermodynamic and feasibility study of a deployable aerobraking re-entry capsule. *Fluid Dynamics & Material Processing*, 8:453–477, December 2012. doi: 10.3970/fdmp.2012.008.453.

[27] J. Muylaert, L. Walpot, H. Ottens, and F. Cipollini. Aerothermodynamic reentry flight experiments - EXPERT. In *Flight Experiments for Hypersonic Vehicle Development*, pages 1–34, 2007. Paper 13.

[28] S. Yoon, P. Gnoffo, J. White, and J. Thomas. Computational challenges in hypersonic flow simulations. In *39th AIAA Thermophysics Conference*, June 2007. ISBN 978-1-62410-010-9. doi: 10.2514/6.2007-4265.

[29] K. Sinha. Computational fluid dynamics in hypersonic aerothermodynamics. *Defence Science Journal*, 60:663–671, November 2010. doi: 10.14429/dsj.60.604.

[30] Z. Jiang and H. Yu. Theories and technologies for duplicating hypersonic flight conditions for ground testing. *National Science Review*, 4(3):290–296, 02 2017. ISSN 2095-5138. doi: 10.1093/nsr/nwx007.

[31] ESA. Expert. Retrieved May 8, 2019, from `http://www.esa.int/Our_Activities/Human_and_Robotic_Exploration/EXPERT/Expert_European_eXPErimental_Reentry_Testbed`.

[32] N. A. Kharchenko and I. A. Kryukov. Aerothermodynamics calculation of the EXPERT reentry flight vehicle. *Journal of Physics: Conference Series*, 1009, April 2018.

[33] F. Ratti, J. Gavira, G. Passarelli, and F. Massobrio. Expert - The ESA Experimental Re-entry Test-bed: System overview. In *16th AIAA/DLR/DGLR International Space Planes and Hypersonic Systems and Technologies Conference*. AIAA 2009-7224, October 2009. ISBN 978-1-60086-968-6. doi: 10.2514/6.2009-7224.

[34] M. D. Clemente, M. Marini, S. D. Benedetto, A. Schettino, and G. Ranuzzi. Numerical prediction of aerothermodynamic effects on a reentry vehicle body flap configuration. *Acta Astronautica*, 65: 221–239, July-August 2009.

[35] G. E. Palmer and M. J. Wright. A comparison of methods to compute high-temperature gas viscosity. *Journal of Thermophysics and Heat Transfer*, 17, April 2003.

[36] A. M. Kharitonov, N. P. Adamov, I. I. Mazhul, L. G. Vasenyov, V. I. Zvegintsev, and J. Muylaert. Aerodynamics of the Expert re-entry ballistic vehicle. January 2009.

[37] C. Weiland. *Aerodynamic Data of Space Vehicles*. Springer, 2014.

[38] P. Baiocco, S. Guedron, S. Plotard, and J. Moulin. The pre-X atmospheric re-entry experimental lifting body: Program status and system synthesis. In *57th International Astronautical Congress*. Valencia, Spain, Paper 06-D2.P.2.02, 2006.

[39] P. Roncioni, G. Ranuzzi, M. Marini, and E. Cosson. Hypersonic CFD characterization of iXV vehicle. In *West-East Hight Speed Flow Field Conference*, November 2007.

[40] European Space Agency. iXV: Intermediate eXperimental Vehicle Fact Sheet. Technical report, 2017.

[41] P. Roncioni, G. Ranuzzi, M. Marini, and S. Paris. Experimental and numerical investigation of aerothermal characteristics of the iXV hypersonic vehicle. *Journal of Spacecraft and Rockets*, April 2011. doi: 10.2514/1.48331.

[42] T. J. Horvath, T. F. O'Connell, F. Cheatwood, R. K. Prabhu, and S. Alter. Experimental hypersonic aerodynamic characteristics of the 2001 Mars surveyor precision lander with flap. *Journal of Spacecraft and Rockets*, 43, February 2002. doi: 10.2514/1.19651.

[43] J. Sepulveda. Aerodynamic modeling and assessment of flaps for hypersonic trajectory control of blunt bodies. Master's thesis, University of Illinois at Urbana-Champaign, Urbana, Illinois, 2017.

[44] M. J. Djomehri and L. Erickson. An assessment of the adaptive unstructured tetrahedral grid, Euler Flow Solver Code FELISA. Technical Report NASA-TP-3526, December 1994.

[45] P. Gnoffo and F. M. Cheatwood. User's Manual for the Langley Aerothermodynamic Upwind Relaxation Algorithm (LAURA). Technical Report NASA-TM-4674, April 1996.

[46] K. J. Murphy, A. Korzun, A. Watkins, and K. Edquist. Testing of the trim tab parametric model in NASA Langley's unitary plan wind tunnel. In *31st AIAA Applied Aerodynamics Conference*, June 2013. doi: 10.2514/6.2013-2808.

[47] R. I. Sammonds and R. R. Dickey. Effectiveness of several control arrangements on a mercury-type capsule. Technical Report NASA-TM-X-579, 1961.

[48] T. Tendeland and B. D. Pearson. Effectiveness of two flap controls on a Mercury-type capsule at a mach number of 15 in the Ames hypersonic helium tunnel. Technical Report NASA TM X-660, October 1962.

[49] B. Lopez. *Simulation des Ecoulements de Plasma Hypersonique Hors Equilibre Thermochimique.* PhD thesis, Université D'Orléans, France, 2010.

[50] C. Park. Assessment of two-temperature kinetic model for ionizing air. *Journal of Thermophysics and Heat Transfer*, 3(3):233–244, July 1989.

[51] P. A. Gnoffo, R. N. Gupta, R. A. T. J. L. Shinn, and K.-P. Lee. Conservation equations and physical models for hypersonic air flows in thermal and chemical nonequilibrium. Technical Report NASA-TP-2867, February 1989.

[52] C. Park. The limits of two-temperature kinetic model in air. In *48th AIAA Aerospace Sciences Meeting Including the New Horizons Forum and Aerospace Exposition*, January 2010. ISBN 978-1-60086-959-4.

[53] E. H. Hirschel. *Basics of Aerothermodynamics.* Progress in astronautics and aeronautics 204 [sic]. Springer, 1st edition, 2005. ISBN 9783540221326,3-540-22132-8.

[54] S. Chapman and T. G. Cowling. *The Mathematical Theory of Non-uniform Gases.* Cambridge Mathematical Library, 3rd edition, 1970.

[55] F. G. Blottner, M. Johnson, and M. Ellis. Chemically reacting viscous flow program for multicomponent gas mixtures. Technical Report SC-RR-70-754, January 1971.

[56] G. Palmer and M. Wright. A comparison of methods to compute high-temperature gas thermal conductivity. In *36th AIAA Thermophysics Conference*, 2003. doi: 10.2514/6.2003-3913.

[57] C. R. Wilke. A viscosity equation for gas mixtures. *The Journal of Chemical Physics*, 18, 1950.

[58] R. N. Gupta, J. M. Yos, R. A. Thompson, and K.-P. Lee. A review of reaction rates and thermodynamic and transport properties for an 11-species air model for chemical and thermal nonequilibrium calculations to 30000 K. Technical Report NASA-RP-1232, June 2002.

[59] H. Alkandry, I. D. Boyd, and A. Martin. Comparison of models for mixture transport properties for numerical simulations of ablative heat-shields. In *51st AIAA Aerospace Sciences Meeting including the New Horizons Forum and Aerospace Exposition*, January 2013. doi: 10.2514/6.2013-303.

[60] J. D. Ramshaw and C. H. Chang. Ambilolar diffusion in two-temperature multicomponent plasmas. *Plasma Chemistry and Plasma Processing*, 13:489–498, September 1993. ISSN: 0272-4324.

[61] F. F. Chen. *Introduction to Plasma Physics and Controlled Fusion*, volume 1. Springer, 2nd edition, 1984. ISBN 0306413329,9780306413322.

[62] J. H. Lee. *Thermal Design of Aeroassisted Orbital Transfer Vehicles - Basic Governing Equations for the Flight Regimes of Aeroassisted Orbital Transfer Vehicles*, volume 10.2514/4.865718. 1985. ISBN 978-0-915928-94-1,978-1-60086-571-8. doi: 10.2514/5.9781600865718.0003.0053.

[63] J. R. Hess. Aerogravity assists: Hypersonic maneuvering to improve planetary gravity assists. Master's thesis, Deltf University of Technology, Delft, February 2016.

[64] M. D. Maughmer, L. N. Long, and P. J. Pagano. Prediction of forces and moments for hypersonic flight vehicle control effectors. Technical Report NASA-CR-193033, May 1993.

[65] D. G. Fletcher. Fundamentals of hypersonic flow - Aerothermodynamics. In *RTO AVT Lecture Series on "Critical Technologies for Hypersonic Development"*. von Karman Institute, Belgium, 2005.

[66] B. Lopez and M. L. da Silva. SPARK: A software package for aerodynamics, radiation and kinetics. In *46th AIAA Thermophysics Conference*, June 2016. doi: 10.2514/6.2016-4025.

[67] Instituto de Plasmas e Fusão Nuclear (2016). Hypersonic Plasmas Laboratory, SPARK. Retrieved April 30, 2019, from `https://www.ipfn.tecnico.ulisboa.pt/nprime/hpl/codes.html`.

[68] D. A. Andrienko. *Non-equilibrium Models for High Temperature Gas Flows.* PhD thesis, Wright State University, United States of America, 2014.

[69] B. Sundén and J. Fu. *Heat Transfer in Aerospace Applications*. Academic Press, 1st edition, 2016. ISBN 9780128097618,9780128097601.

[70] R. K. Agarwal, K.-Y. Yun, and R. Balakrishnan. Beyond Navier-Stokes: Burnett equations for flows in the continuum-transition regime. *Physics of Fluids*, 13, 2001. doi: 10.1063/1.1397256.

[71] T. Schlegat. Experimental investigation of rarefaction effects on aerodynamic coefficients on slender and blunt re-entry vehicles. *DLR Deutsches Zentrum fur Luft- und Raumfahrt e.V. - Forschungsberichte*, 2016(23):1–134, January 2016.

[72] B. E. Rapp. *Microfluidics: Modeling, Mechanics and Mathematics. A volume in Micro and Nano Technologies*. Elsevier, 1st edition, 2016. ISBN 9781455731510,9781455731411.

[73] National Aeronautics and Space Administration (NASA). The Standard Atmosphere, 1976. Technical Report NASA-TM-X-74335, October 1976.

[74] R. W. MacCormack. Carbuncle computational fluid dynamics problem for blunt-body flows. *Journal of Aerospace Information Systems*, 10, May 2013. doi: 10.2514/1.53684.

[75] M. Pandolfi and D. D'Ambrosio. Numerical instabilities in upwind methods: Analysis and cures for the carbuncle phenomenon. *Journal of Computational Physics*, 166, 2001. doi: 10.1006/jcph.2000.6652.

[76] J. B. J. J. Bertin, J. Periaux. *Advances in Hypersonics —— Wall Recombination and Boundary Conditions in Nonequilibrium Hypersonic Flows - with Applications*, volume 10.1007/978-1-4612-0371-1. 1992. ISBN 978-1-4612-6730-0,978-1-4612-0371-1. doi: 10.1007/978-1-4612-0371-1_6.

[77] E. Farbar, A. Martin, I. Boyd, and M. Kim. Investigation of the effects of electronic-electron translational nonequilibrium on numerical prediction of hypersonic flow fields. In *42nd AIAA Thermophysics Conference*, June 2011. doi: 10.2514/6.2011-3136.

[78] G. Candler. Translation-vibration-dissociation coupling in nonequilibrium hypersonic flows. In *24th Thermophysics Conference*, 1989. doi: 10.2514/6.1989-1739.

[79] R. C. Millikan and D. R. White. Systematics of vibrational relaxation. *The Journal of Chemical Physics*, 39, 1963. doi: 10.1063/1.1734182.

[80] C. Park. Review of chemical-kinetic problems of future NASA missions. I - Earth entries. *Journal of Thermophysics and Heat Transfer*, 7, 1993. doi: 10.2514/3.431.

[81] J. P. Appleton, M. Steinberg, and D. J. Liquornik. No Title. *Journal of Chemical Physics*, 48:599–608, December 1968.

[82] K. N. C. Bray. MIT Fluid Mechanics Lab. Rept. No. 67-3, December, 1967.

[83] J. Shang and S. Surzhikov. *Plasma Dynamics for Aerospace Engineering*. Cambridge Aerospace Series. June 2018. ISBN 9781108418973. doi: 10.1017/9781108292566.

[84] K. Sutton and R. A. Graves. A general stagnation-point convective heating equation for arbitrary gas mixtures. Technical Report NASA-TR-R-376, November 1971.

[85] J. C. F. Pereira. *Aerodinâmica Compressível*. AEIST, 2018. Sebenta de Aerodinâmica II.

[86] H. Ashley. *Aerodynamics of Wings and Bodies*. Dover Books on Engineering. Dover Publications, 1985. ISBN 0486648990.

Appendix A

Physical Chemistry

A.1 Thermodynamic Relations

A.1.1 Gas Mixture Composition

Several different ways can be used to describe the composition of a chemical reacting gas, with the purpose of identifying the quantity of species i present in the gas mixture. Some of the quantities that uniquely define the mixture chemical composition are, for example, the mole fraction x_i, defined as

$$x_i = \frac{n_i}{n} = \frac{N_i}{N}\,, \tag{A.1}$$

where n_i and N_i represent the number of moles and particles of species i present in the mixture and n and N represent the total moles and particles present in the gas mixture, respectively. Or even the mass fraction

$$c_i = \frac{\rho_i}{\rho}\,, \tag{A.2}$$

where ρ_i represents the mass density of each species.

Based on the definitions of x_i, c_i and ρ_i, the following relations are true:

$$\sum_i x_i = 1, \qquad \sum_i c_i = 1 \qquad \text{and} \qquad \rho = \sum_i \rho_i\,. \tag{A.3}$$

The conversion between the different composition variables can be obtained through the following relations:

$$c_i = x_i \frac{M_i}{M} \qquad \text{and} \qquad c_i = \frac{n_i M_i}{\rho V}\,, \tag{A.4}$$

where V is the volume of the global gas mixture and M is the molar mass of the global gas mixture, which can be computed as

$$M = \sum_i x_i M_i = \frac{1}{\left(\sum\limits_i \frac{c_i}{M_i}\right)} \,. \tag{A.5}$$

A.1.2 Equation of State

In this work, the individual chemical species that constitute the gas mixture are assumed to behave as an ideal gas and therefore, the intermolecular forces between particles is negligible. Under these conditions, Dalton's Law of Partial Pressures hold as

$$p = \sum_i p_i \,, \tag{A.6}$$

and the partial pressure p_i also obeys various equations of state, such as

$$p_i = \rho_i R_i T_{\text{tra},i}, \qquad p_i = \frac{n_i}{V} R_u T_{\text{tra},i} \qquad \text{or} \qquad p_i = \frac{N_i}{V} k_B T_{\text{tra},i} \,, \tag{A.7}$$

where V is the volume of the global mixture. The specific gas constant R_i can be related to the universal gas constant R_u, to the Boltzmann constant k_B, to the i^{th} species particle mass m_i and other variables as

$$R_i = \frac{R_u}{M_i} = \frac{N_A k_B}{M_i} = \frac{k_B}{m_i} = \frac{R_u / N_A}{m_i} \,. \tag{A.8}$$

A.1.3 Thermodynamic Properties

Internal Energy

The internal energy per unit mass of the mixture of perfect gases is given by

$$e = \sum_i c_i e_i \,, \tag{A.9}$$

and represents the total energy stored in the internal degrees of freedom of the species of the gas. The specific energy associated to each species is defined as

$$\begin{aligned} e_i &= e_{\text{tra},i} + e_{\text{rot},i} + e_{\text{vib},i} + e_{\text{exc},i} + (\Delta h_s)^\circ_i \\ &= \underbrace{\frac{3}{2} R_i T_{\text{tra}}}_{\text{Translation}} + \underbrace{R_i T_{\text{rot}}}_{\text{Rotation}} + \underbrace{\frac{\theta_{\text{vib},i}}{e^{\theta_{\text{vib}}/T_{\text{vib},i}} - 1} R_i}_{\text{Vibration}} + \underbrace{\frac{\sum\limits_l \theta_{\text{exc},l,i} g_{l,i} \exp\left\{\left(-\frac{\theta_{\text{exc},l,i}}{T_{\text{exc},i}}\right)\right\}}{\sum\limits_l g_{l,i} \exp\left\{\left(-\frac{\theta_{\text{exc},l,i}}{T_{\text{exc},i}}\right)\right\}} R_i}_{\text{Electronic Excitation}} + \underbrace{(\Delta h_s)^\circ_i}_{\text{Effective zero point energy}} \,. \end{aligned} \tag{A.10}$$

where $\theta_{\text{vib},i}$ is the i^{th} species characteristic vibrational temperature and $\theta_{\text{exc},l,i}$ is the characteristic electronic temperature, $g_{l,i}$ is the degeneracy of the l^{th} energy level of the i^{th} species and $(\Delta h_s)_i^\circ$ is also known as the standard formation enthalpy or the chemical enthalpy.

The global internal energy associated to each global temperature T_k is given by Equation 2.6, repeated here for convinence:

$$e_k = \sum_i c_i e_{k,i}\ , \tag{A.11}$$

Enthalpy

In a similar way, the global enthalpy associated to each temperature is computed as

$$h_k = \sum_i c_i h_{k,i}\ , \tag{A.12}$$

and the total enthalpy of the mixture can be obtained as

$$h = \sum_k h_k + (\Delta h_s)_i^\circ\ . \tag{A.13}$$

The specific enthalpy associated to each species is defined as

$$\begin{aligned} h_i &= h_{\text{tra},i} + h_{\text{rot},i} + h_{\text{vib},i} + h_{\text{exc},i} + (\Delta h_s)_i^\circ \\ &= e_{\text{tra},i} + R_i T_{\text{tra},i} + e_{\text{rot},i} + e_{\text{vib},i} + e_{\text{exc},i} + (\Delta h_s)_i^\circ\ . \end{aligned} \tag{A.14}$$

Specific Heats

The rate of change of the internal energy and enthalpy as a function of the temperature is defined as the gas specific heat at constant volume c_v, and the specific heat at constant pressure c_p. That is,

$$c_v \equiv \left(\frac{\partial e}{\partial T}\right)_V \qquad \text{and} \qquad c_p \equiv \left(\frac{\partial h}{\partial T}\right)_p\ . \tag{A.15}$$

Taking into account the four energy modes described in this work, the previous definitions become

$$\begin{cases} c_v = \sum_k c_{v_k} = \sum_k \frac{\partial e_k}{\partial T_k} \\ c_p = \sum_k c_{p_k} = \sum_k \frac{\partial h_k}{\partial T_k} \end{cases} \tag{A.16}$$

From the definitions encountered in Equations A.11 and A.12, the following relations are obtained:

$$\begin{cases} c_{v_k} = \sum_i \left(c_i \frac{\partial e_{k,i}}{\partial T_{k,i}} + e_{k,i} \frac{\partial c_i}{\partial T_{k,i}}\right) \\ c_{p_k} = \sum_i \left(c_i \frac{\partial h_{k,i}}{\partial T_{k,i}} + h_{k,i} \frac{\partial c_i}{\partial T_{k,i}}\right) \end{cases} \tag{A.17}$$

In Equation A.17, a frozen (constant chemical composition of the gas) component and a reactive component can be identified. Using only the frozen component of both specific heats, c_v and c_p become

$$\begin{cases} c_{v_k} = \sum_i c_i \frac{\partial e_{k,i}}{\partial T_{k,i}} \\ c_{p_k} = \sum_i c_i \frac{\partial h_{k,i}}{\partial T_{k,i}} \end{cases} \tag{A.18}$$

with,

$$\begin{cases} c_{v_{\text{tra},i}} = \frac{3}{2} R_i \; ; \; c_{p_{\text{tra},i}} = \frac{5}{2} R_i \\ c_{v_{\text{rot},i}} = c_{p_{\text{rot},i}} = R_i \\ c_{v_{\text{vib},i}} = c_{p_{\text{vib},i}} = \frac{\partial e_{\text{vib},i}}{\partial T_{vib} i} \\ c_{v_{\text{exc},i}} = c_{p_{\text{exc},i}} = \frac{\partial e_{\text{exc},i}}{\partial T_{exc} i} \end{cases} \tag{A.19}$$

The following relations between the specific heats, R_u, R_i and γ hold:

$$R_u = c_p - c_v, \qquad R_i = c_{p_{\text{tra},i}} - c_{v_{\text{tra},i}} \qquad \text{and} \qquad \gamma = \frac{c_p}{c_v}\,. \tag{A.20}$$

Appendix B

Aerodynamic Coefficients

The results for the aerodynamic coefficients of the reentry vehicle without the nozzle thermal protection system are shown in the following figures for the four different flap configurations considered in the present work.

180° Flap Configuration Centred at Y$_A$ = 0 m and Z$_A$ = 0.95 m

Figures B.1 and B.2 show the drag, lift and pitching moment coefficients for a 180° flap configuration when the nozzle protection system is not included in the geometry. In this case, the maximum aerodynamic efficiency is 0.2 instead of 0.19 for $\eta = 30°$.

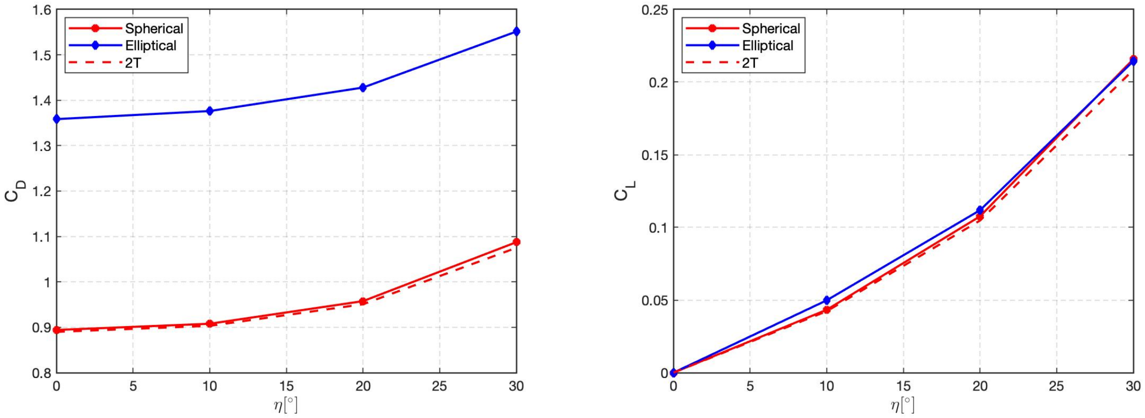

(a) Drag coefficient

(b) Lift coefficient

Figure B.1: Drag and lift coefficients as function of the flap deflection angle for the vehicle with a 180° flap centred at Y$_A$ = 0 m and Z$_A$ = 0.95 m.

The moments for $\eta = 10°$ show differences as high as 58% between the two cases.

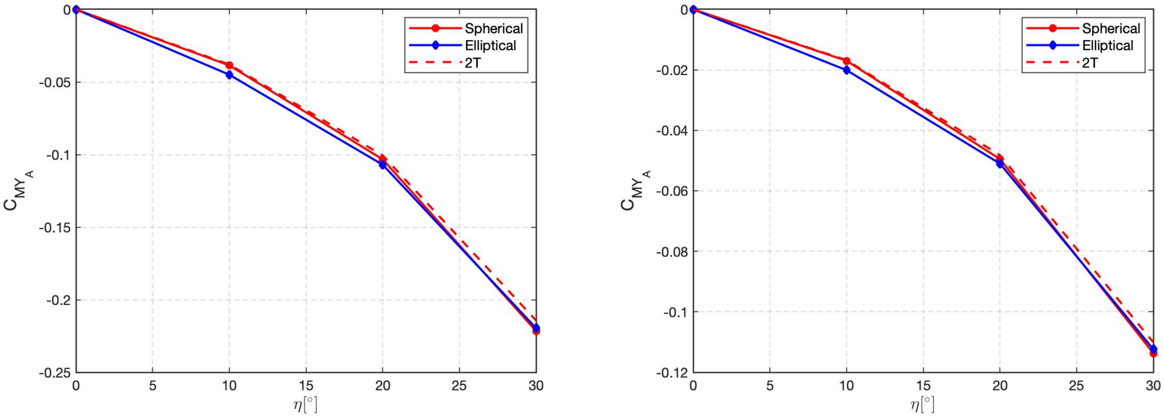

(a) Pitching moment coefficient about $\{\mathrm{X}_A, \mathrm{Y}_A, \mathrm{Z}_A\}$ = $\{0, 0, 0\}$ m

(b) Pitching moment coefficient about $\{\mathrm{X}_A, \mathrm{Y}_A, \mathrm{Z}_A\}$ = $\{-0.5c_{ref}, 0, 0\}$ m

Figure B.2: Pitching moment coefficients as function of the flap deflection angle for the vehicle with a 180° flap centred at Y_A = 0 m and Z_A = 0.95 m.

90° Flap Configuration Centred at Y_A = 0 m and Z_A = 0.95 m

Figures B.3 and B.4 show the drag, lift and pitching moment coefficients for a 90° symmetric flap configuration. This configuration leads to a maximum aerodynamic efficiency of 0.14 for the deflection angles considered.

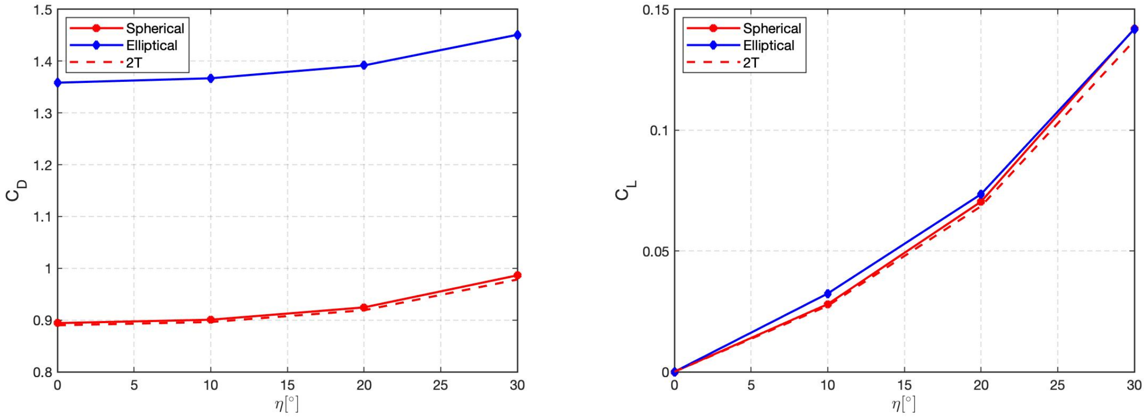

(a) Drag coefficient

(b) Lift coefficient

Figure B.3: Drag and lift coefficients as function of the flap deflection angle for the vehicle with a 90° flap centred at Y_A = 0 m and Z_A = 0.95 m.

The moment coefficients with respect to the Y_A axis increase in absolute value as the flap deflection angle increases (Figure B.4), reaching a maximum of around 0.145 and 0.07 for the reference point at the origin and mid-chord, respectively.

The moments for $\eta = 10^\circ$ show differences as high as 59% between the two cases.

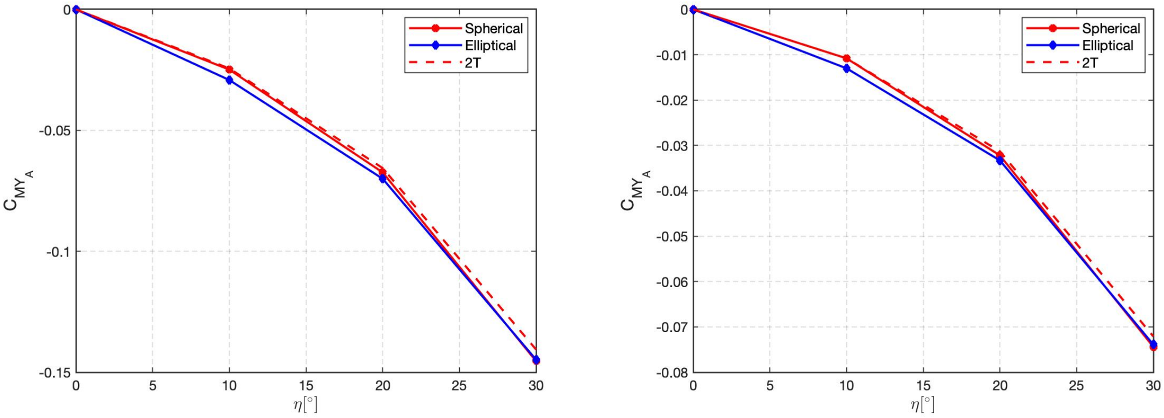

(a) Pitching moment coefficient about {X$_A$, Y$_A$, Z$_A$} = {0, 0, 0} m

(b) Pitching moment coefficient about {X$_A$, Y$_A$, Z$_A$} = {-0.5c_{ref}, 0, 0} m

Figure B.4: Pitching moment coefficients as function of the flap deflection angle for the vehicle with a 90° flap centred at Y$_A$ = 0 m and Z$_A$ = 0.95 m.

90° Flap Configuration Centred at Y$_A$ = 0.67 m and Z$_A$ = 0.67 m

Figure B.5 shows the drag and lift coefficients for a 90° centred at Y$_A$ = 0.67 m and Z$_A$ = 0.67 m. This flap is not symmetric with respect to the plane defined by Y$_A$ = 0 and therefore, additional moments are created by the aerodynamic forces (Figures B.6 and B.7).

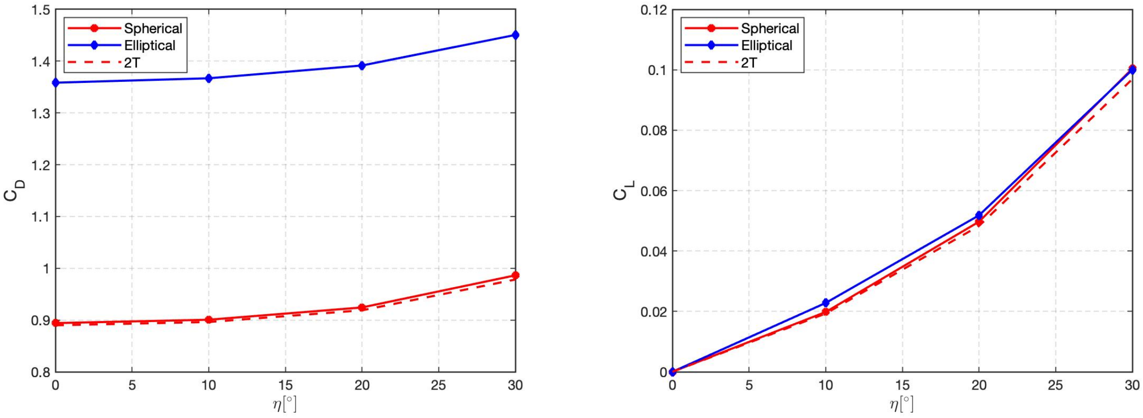

(a) Drag coefficient

(b) Lift coefficient

Figure B.5: Drag and lift coefficients as function of the flap deflection angle for a vehicle with a 90° flap centred at Y$_A$ = 0.67 m and Z$_A$ = 0.67 m.

The aerodynamic efficiency is not higher than 0.1 for the deflection angles considered.

The moments for $\eta = 10°$ show differences as high as 68% between the two cases.

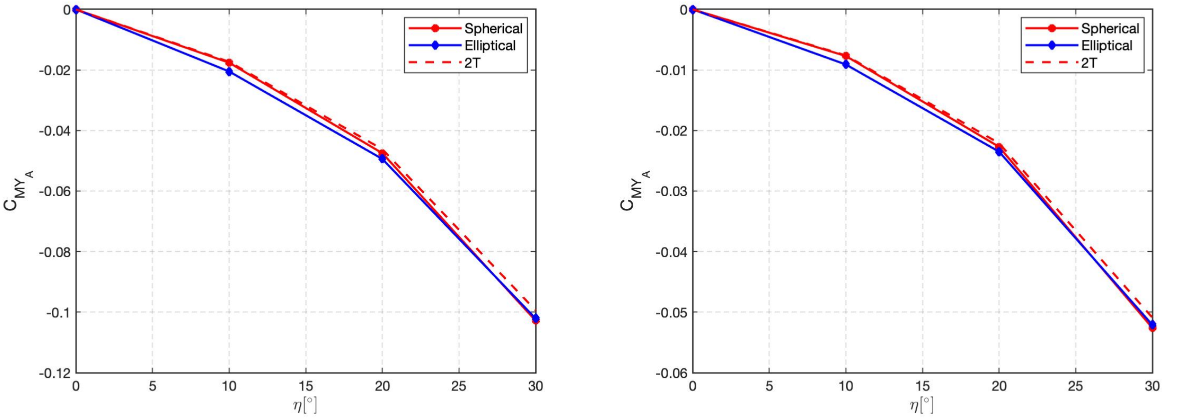

(a) Pitching moment coefficient about $\{X_A, Y_A, Z_A\} = \{0, 0, 0\}$ m

(b) Pitching moment coefficient about $\{X_A, Y_A, Z_A\} = \{-0.5c_{ref}, 0, 0\}$ m

Figure B.6: Pitching moment coefficients as function of the flap deflection angle for a vehicle with a 90° flap centred at Y_A = 0.67 m and Z_A = 0.67 m.

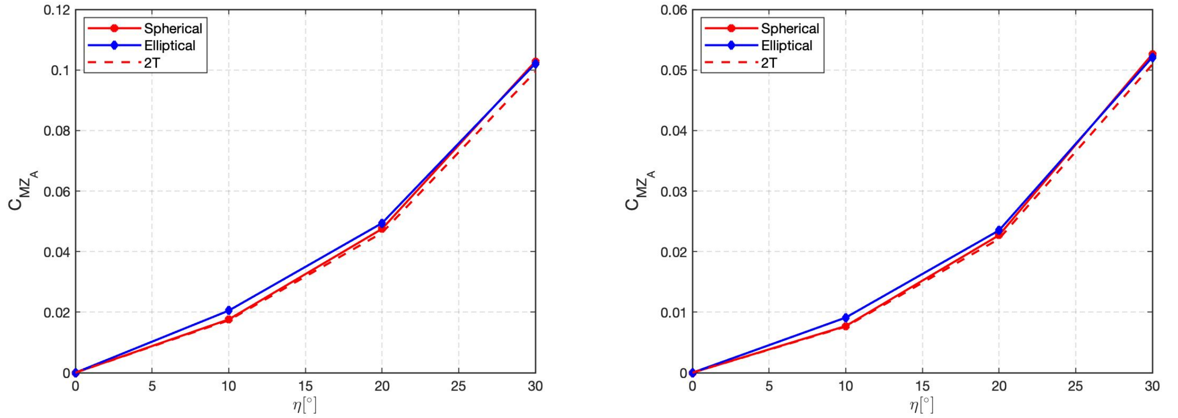

(a) Yawing moment coefficient about $\{X_A, Y_A, Z_A\} = \{0, 0, 0\}$ m

(b) Yawing moment coefficient about $\{X_A, Y_A, Z_A\} = \{-0.5c_{ref}, 0, 0\}$ m

Figure B.7: Yawing moment coefficients as function of the flap deflection angle for a vehicle with a 90° flap centred at Y_A = 0.67 m and Z_A = 0.67 m.

45° Flap Configuration Centred at Y_A = 0.36 m and Z_A = 0.88 m

Figure B.8 shows the drag and lift coefficients for a 90° centred at Y_A = 0.36 m and Z_A = 0.88 m.

This configuration leads to the lowest aerodynamic efficiency of all the flap configurations studied considering the maximum deflection angle, with a value of 0.067, for the circular case.

In Figure B.10 (b), an increase of 1200% in the moment coefficient with respect to the case where the nozzle protection system is deployed for the $\eta = 10^\circ$ case is observed.

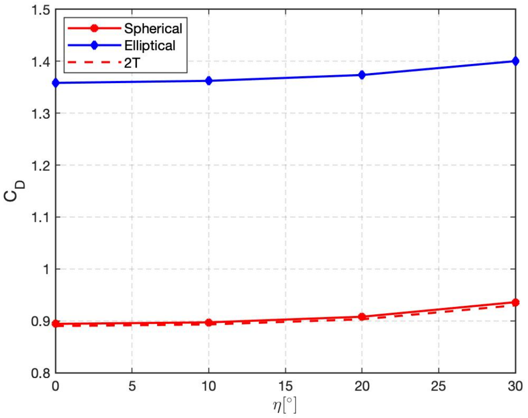

(a) Drag coefficient (b) Lift coefficient

Figure B.8: Drag and lift coefficients as function of the flap deflection angle for a vehicle with 45° flap centred at Y_A = 0.36 m and Z_A = 0.88 m.

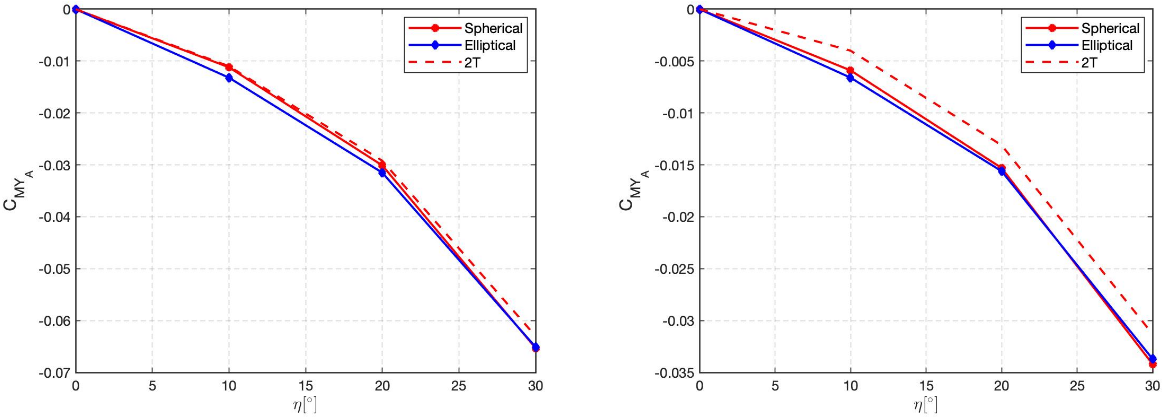

(a) Pitching moment coefficient about $\{X_A, Y_A, Z_A\}$ = $\{0, 0, 0\}$ m (b) Pitching moment coefficient about $\{X_A, Y_A, Z_A\}$ = $\{-0.5c_{ref}, 0, 0\}$ m

Figure B.9: Pitching moment coefficients as function of the flap deflection angle for a vehicle with 45° flap centred at Y_A = 0.36 m and Z_A = 0.88 m.

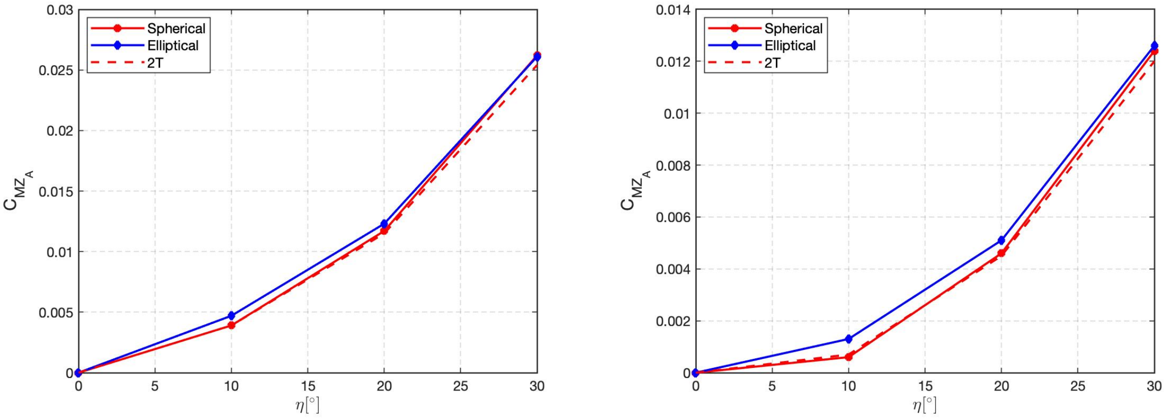

(a) Yawing moment coefficient about $\{X_A, Y_A, Z_A\}$ = $\{0, 0, 0\}$ m (b) Yawing moment coefficient about $\{X_A, Y_A, Z_A\}$ = $\{-0.5c_{ref}, 0, 0\}$ m

Figure B.10: Yawing moment coefficients as function of the flap deflection angle for a vehicle with 45° flap centred at Y_A = 0.36 m and Z_A = 0.88 m.